FABRICATION AND CHARACTERIZATION OF WAVEGUIDE LASERS OPERATING IN THE INFRARED SPECTRAL RANGE

Esrom Aschenaki Kifle

UNIVERSITAT ROVIRA i VIRGILI

Fabrication and characterization of waveguide lasers operating in the infrared spectral range

Esrom Aschenaki Kifle

DOCTORAL THESIS
2019

UNIVERSITAT ROVIRA I VIRGILI
FABRICATION AND CHARACTERIZATION OF WAVEGUIDE LASERS OPERATING IN THE INFRARED SPECTRAL RANGE
Esrom Aschenaki Kifle

Fabrication and characterization of waveguide lasers operating in the infrared spectral range

Esrom Aschenaki Kifle

Doctoral Thesis

Supervised by:

Dr. Xavier Mateos Ferré
Prof. Dr. Magdalena Aguiló Díaz

Departament de Química Física i Inorgànica
Física i Cristal·lografia de Materials i Nanomaterials (FiCMA - FiCNA)

UNIVERSITAT ROVIRA i VIRGILI

Tarragona
2019

UNIVERSITAT ROVIRA I VIRGILI
FABRICATION AND CHARACTERIZATION OF WAVEGUIDE LASERS OPERATING IN THE INFRARED SPECTRAL RANGE
Esrom Aschenaki Kifle

Fabrication and characterization of waveguide lasers operating in the infrared spectral range

Esrom Aschenaki Kifle

Física i Cristal·lografia de Materials i Nanomaterials (FiCMA - FiCNA)
Departament de Química Física i Inorgànica
Universitat Rovira i Virgili
C/ Marcel·lí Domingo, 1
E-43007, Tarragona, Spain

UNIVERSITAT ROVIRA I VIRGILI
FABRICATION AND CHARACTERIZATION OF WAVEGUIDE LASERS OPERATING IN THE INFRARED SPECTRAL RANGE
Esrom Aschenaki Kifle

UNIVERSITAT ROVIRA I VIRGILI

DEPARTAMENT DE QUÍMICA FÍSICA I INORGÀNICA

Campus Sescelades
Marcel·lí Domingo, s/n
43007 Tarragona
Tel. +34 977 55 81 37
Fax +34 977 55 95 63
www.quimica.urv.es

We STATE that the present study, entitled "**Fabrication and characterization of waveguide lasers operating in the infrared spectral range**", presented by Esrom Aschenaki Kifle for the award of the degree of Doctor, has been carried out under our supervisión at the Department of Physical and Inorganic Chemistry of this University, and that it fulfills all the requirements to be eligible for the International Doctorate Mention.

Tarragona, June 6, 2019

Doctoral Thesis Supervisors

Dr. Xavier Mateos Ferré

Prof. Magdalena Aguiló Díaz

UNIVERSITAT ROVIRA I VIRGILI
FABRICATION AND CHARACTERIZATION OF WAVEGUIDE LASERS OPERATING IN THE INFRARED SPECTRAL RANGE
Esrom Aschenaki Kifle

Abstract

Fabrication and characterization of waveguide lasers operating in the infrared spectral range

This thesis deals with the development of compact and efficient waveguide lasers operating in the continuous wave and passively *Q*-switched operation regimes in the near-infrared spectral range. To this aim, erbium (Er^{3+}), thulium (Tm^{3+}) and holmium (Ho^{3+}) doped monoclinic double tungstate crystalline materials were employed. These gain media were chosen due to their ability to generate polarized laser emission, their large interatomic distance favouring high doping levels with minimum luminescence quenching, and their high absorption and emission cross-sections which makes them suitable for achieving compact devices.

Waveguides offer unique advantages such as a lower laser threshold, a small device-footprint, a better heat dissipation, and a good laser beam quality. The combinations of the top-seeded solution growth (TSSG), liquid phase epitaxy (LPE), diamond saw dicing and femtosecond direct laser writing (fs-DLW) methods were employed for fabricating and structuring the waveguides. Furthermore, different characterization techniques such as confocal microscopy, μ-Raman, and μ-luminescence mapping were implemented to assess the quality and suitability of the fabricated waveguides for lasing application.

The saturable absorbers employed in the passive *Q*-switching operations included transition-metal-doped chalcogenide crystals (Cr^{2+}:ZnSe or ZnS), few-layer transition metal dichalcogenide (MoS_2) and carbon nanostructures such as graphene and single-walled carbon nanotubes deposited on a transparent substrate or directly onto the surface of the sample containing the waveguides.

The fabrication of an active (Tm^{3+}- doped) surface channel waveguide, by combining the LPE and the diamond saw dicing methods resulted in a record slope efficiency (82.6%) almost approaching the theoretical limit. Fs-DLW buried channel waveguides (with circular and hexagonal optical-lattice-like cladding), surface channel waveguides (with half-ring-shaped cladding) and Y-branch splitters (with rectangular cladding) were fabricated and studied in a monoclinic double tungstate crystalline material, for the first time.

Fs-DLW Tm^{3+} waveguide laser capable of delivering a watt-level output power was demonstrated around 2 μm spectral range. In-band pumping of such Tm^{3+} waveguide laser resulted in a record slope efficiency (85.7%) and output power (1.37 W). In the pulsed operation regime, sub-100 ns pulses with MHz repetition frequency were demonstrated.

Passive *Q*-switching of Tm^{3+} surface waveguide laser based on an evanescent field interaction led to stable operation with a higher *Q*-switching conversion efficiency (approaching 90%) and a lower intensity instability in the pulse train (below 15%) than for normal incidence on the saturable absorbers. Additionally, the first demonstration of Er^{3+}- doped, Ho^{3+}- doped, and (Ho^{3+}, Tm^{3+}) co-doped fs-DLW waveguide lasers in a monoclinic double tungstate crystalline material are also presented in this thesis work.

Keywords: Crystal growth, Er^{3+}, Tm^{3+} and Ho^{3+}- doped waveguide lasers, channel waveguides, solid-state lasers, *Q*-switched lasers, femtosecond direct laser writing, saturable absorbers, liquid phase epitaxy.

Preface

The Ph.D. investigation contained in this thesis has been carried out at the group of Física i Cristal.lografia de Materials i Nanomaterials (FiCMA-FiCNA) at the Departament de Química Física i Inorgànica of the Universitat Rovira i Virgili, Tarragona, Spain and was supervised by Dr. Xavier Mateos Ferré and Prof. Dr. Magdalena Aguiló Díaz.

This thesis has been carried out in collaboration with the following groups and researchers: Dr. Valentin Petrov and Dr. Uwe Griebner at the Max-Born Institute for Nonlinear Optics and Short Pulse Spectroscopy (Berlin, Germany), Dr. Pavel Loiko and Prof. Patrice Camy at the CIMAP laboratory, Université de Caen (Caen, France), Dr. J. R. Vázquez de Aldana, at the University of Salamanca (Salamanca, Spain), Prof. Fabian Rottermund at KAIST (Daejeon, Republic of Korea), Prof. Viktor Zakharov and Prof. Andrey Veniaminov at ITMO University (Saint Petersburg, Russia), Prof. Huaijin Zhang and Prof. Haohai Yu at the State Key Laboratory of Crystal Materials, Shandong University (Jinan, China), Dr. Venkatesan Jambunathan, Dr. Antonio Lucianetti and Dr. Tomas Mocek at the HILASE Center, Institute of Physics ASCR (Dolní Brezany, Czech Republic), and Prof. Mikael Ostling at KTH Royal Institute of Technology, (Stockholm, Sweden).

This work was financially supported by

Agencia de Gestió d'Ajuts Universitaries i de Recerca, AGAUR, de la Generalitat de Catalunya through the fellowships 2016FI_B00844, 2017FI_B100158 and 2018FI_B200123.

Spanish Government (MAT2016-75716-C2-1-R (AEI/FEDER,UE) and TEC2014-55948-R); Generalitat de Catalunya (2017SGR755).

Esrom Aschenaki Kifle
Tarragona, 2019

Acknowledgments

My journey during this thesis work would not have been successful without the support of my family, friends, and colleagues. I am very grateful to my supervisors Prof. Dr. Magdalena Aguiló and Dr. Xavier Mateos for giving me the opportunity to conduct my Ph.D. research in FiCMA-FiCNA group and for their constant encouragement. I would like to especially acknowledge Dr. Xavier Mateos, for his constant motivation, guidance, for his patience, and his friendly advice. I thank Prof. Dr. Francesc Díaz for welcoming me into the group and encouraging me along this journey.

My thesis work was also greatly supported by Dr. Pavel Loiko, Dr. Josep Maria Serres, Dr. Venkatesan Jambunathan, and Dr. Arian Ródenas, I am very grateful for all the discussions and support during my time in the laboratory. I would also like to thank all the professors and other members of the FiCMA-FiCNA group, especially the technicians: Agustí, Nicole, Dr. Gemma Marsal, and Dr. Josué Mena; fellow students: Marc, Irina, Albenc, and Raja.

I am very grateful to Dr. Valentin Petrov and Dr. Uwe Griebner for giving me the opportunity to work at the Max Born Institute, Germany and to Prof. Patrice Camy for welcoming me into the CIMAP laboratory, France during my research visit. I acknowledge Dr. J. R. Vázquez de Aldana, at the University of Salamanca, Spain and Prof. Fabian Rottermund at the KAIST, Republic of Korea, for their collaboration in fabricating some of the samples used in this thesis work.

My deepest gratitude to all my friends especially those in the Pash community, to Imad, and to all my family in Ethiopia, for their constant encouragement, compassion, and prayers without which it would have been impossible for me to undertake this tough but finally fulfilling journey. I would like to say a special thank you to Tsedi, for patiently being with me along every step of this long journey. I would also like to thank Bab, Sistu, Mengiste, Brehane, Bishop David O.Oyedepo, Past. Olusing Olutade, Past. Zenebe, and Rev. Tezera for their constant prayers and words of encouragement. I would like to express my deepest gratitude to all the Brothers and Sisters at Winners' Chapel International Barcelona, for their encouragement, and prayers.

Lastly, I thank the Catalan Government for their generous support through the fellowships 2016FI_B00844, 2017FI_B100158, and 2018FI_B200123.

“I know thy works: behold, I have set before thee an open door, and no man can shut it: for thou hast a little strength, and hast kept my word, and hast not denied my name.” Rev.3:8

Table of contents

Chapter 1 General introduction

1.1 Introduction

Since the first demonstration of flashlamp pumped ruby laser by Theodore H. Maiman in 1960, lasers have transformed almost every aspect of our lives [1]. They had an estimated worldwide market worth more than $ 13 billion in 2018 [2]. Currently, lasers are being applied in various fields such as, astrophysics - for monitoring the velocity of astronomical objects [3], archaeology - for analysing ancient artefacts [4], military - for free space communications and target recognition in the battlefields [5], medicine - for implementing therapeutics and diagnostic procedures [6], surveillance - for direct remote sensing of greenhouse gases and harmful toxins [7, 8], holography - for optical recording of holograms for image displays [9], femtochemistry - for studying the dynamics of chemical bonds during reactions [10], material processing – for cutting, welding, and stacking in industries [11, 12], optical sensing – for a lab-on-a-chip integrated bio-medical and chemical analysis [13], lithography [14], and telecommunications [15]. We also encounter them in our everyday lives: lasers in our CD-players scanning the disk for reading the signals, the pointers we use during presentations contains fully functional lasers and during concerts “light shows” are being organized using lasers.

Depending on the nature of the output emission, a laser is said to be operating in the continuous wave (CW) or pulsed regime. In CW regime, the gain medium is continuously pumped for generating a constant output power as a function of time. In December 1960, the first CW laser, helium-neon (He-Ne) laser operating at 1.15 µm, was demonstrated at Bell Labs [16]. In the case of the pulsed operation regime, the output power is emitted as an optical pulse within short time windows. Depending on the pulse duration, the pulse energy, and the repetition frequency, different techniques would be implemented for achieving such regimes. The first theoretical work predicting the generation of short optical pulses (through suddenly changing the cavity-losses) was proposed in 1961 by Robert W. Hellwarth, followed by an experimental demonstration using the ruby laser [17]. The intense research efforts, over the last five decades, have led to the dramatic improvement of lasers in terms of their performance as well as their costs [18, 19].

In recent years, a lot of attention has been given to the development of lasers emitting at ~2 µm. Such an emission corresponds to the absorption bands of a number of atmospheric molecules (H_2O, CO_2, N_2O). Due to the strong water absorption band, such emission falls into the category of “eye-safe” lasers which makes them especially suitable for open - space applications, e.g. in range-finding (LIDAR systems), atmospheric sensing and wind mapping [7, 20]. Additionally, the minimally affected zones (i.e. local surgical incisions) and the subsequent coagulation that could be achieved with 2 µm lasers makes them crucial in medical applications [21]. Due to the moderate absorption of such lasers in plastic materials, they are suited for engraving, marking and welding of transparent plastics [22]. In molecular spectroscopy, where mid-infrared sources are needed, 2 µm lasers are better suited for pumping the nonlinear crystals that are implemented for generating such longer wavelengths [22].

Typically, a laser emission at ~2 µm is achieved using solid-state materials doped with the trivalent rare-earth thulium (Tm^{3+}) or holmium (Ho^{3+}) ions or a combination (co-doping) of them. Based on the type of gain medium they can be bulk, fiber, slab, thin-disk or (planar / channel) waveguide lasers. Since the first demonstration [23], waveguide lasers have progressively attracted interest from various emerging applications [24-26]. The unique advantage offered by such a source is, its compactness as the optical modes are confined and index-guided in a small volume. This would lead to higher gain, lower laser threshold, small footprints, better heat dissipation and good beam quality [24]. High power CW and pulsed waveguide lasers operating ~ 2 µm are potentially suitable for making compact LIDAR devices operating on a surveillance-airplane or a satellite for directly monitoring and mapping atmospheric CO_2 [21, 22]. As there are mature technologies capable of fabricating waveguides with different designs and complexity, incorporating additional structures such as Bragg gratings and modulators would lead to more robust lasers [27]. By taking advantage of the direct access (to the gain media) offered by surface waveguides, integration with nonlinear materials would lead to more compact devices having advanced functionalities. Furthermore, specific functionalization (with bioreceptor molecules) or decorations (with plasmonic

nanoparticles) of the deposited materials may lead towards active-biosensing and on-chip spectroscopy applications. Hence, the potential applications in environmental monitoring, security, and medicine, greatly motivate the development of such waveguide lasers.

The goal of this thesis work was, the fabrication and characterization of compact and efficient waveguide lasers operating around 2 µm. To achieve this, thulium and holmium doped monoclinic double tungstate crystalline materials were chosen as gain media, owing to their excellent spectroscopic properties. Their polarized laser emission as well as the high absorption and emission cross-sections, make these gain media suited for designing compact and monolithic waveguide lasers. Different waveguide structures were fabricated and tested as lasers operating in the CW and pulsed regimes.

1.2 Key achievements

Some of the highlights of the results achieved in this thesis are given below. The different units expressed in this section as well as in the rest of the thesis are based on their implementation within the corresponding papers.

1. Carbon nanostructures based saturable absorbers (i.e. graphene, SWCNTs) were implemented for passive *Q*-switching of epitaxially grown Tm^{3+}-doped double tungstate waveguide lasers resulting in MHz pulse repetition frequency.
2. Demonstration of the first highly-doped Tm^{3+}channel waveguide laser based on low-symmetry (monoclinic) crystal and diamond saw dicing technique featuring an output power of 262 mW with a record slope efficiency (82.6%) almost approaching the theoretical limit.
3. The first demonstration of fs-laser-written waveguide lasers in Tm^{3+} doped double tungstate crystals. Passive *Q*-switching of these waveguides using novel nanostructured saturable absorbers such as graphene, SWCNTs, and MoS_2 resulted in sub-100 ns pulse widths with MHz repetition frequency.
4. The first demonstration of evanescent field interaction -based passive *Q*-switching of Tm^{3+} surface waveguide laser resulting in a high *Q*-switching conversion efficiency (approaching 90%) and low intensity instabilities in the pulse trains (<15%).
5. Active Y-splitter waveguide operating in the ~ 2 µm spectral range was demonstrated exhibiting an almost 50% / 50% power splitting ratio and a total output power of 0.46 W, paving the way towards advanced photonic structures such as a Mach – Zehnder interferometer for biosensing application.
6. Demonstration of fs-laser-written Tm^{3+} waveguide laser capable of delivering watt-level output power (in CW regime) and few-ns / µJ pulses with kW peak power (in passive *Q*-switched regime) at ~2 µm. In-band pumping of these Tm^{3+}waveguides resulted in a record slope efficiency (85.7%) and output power (1.37 W).
7. The first demonstrations of singly Er^{3}-doped, Ho^{3+}-doped and (Ho^{3+}, Tm^{3+}) co-doped fs-laser-written waveguide lasers in double tungstate crystals.

1.3 Thesis synopsis

After giving the brief introduction and describing the key achievements, this thesis begins in chapter 2, with a general introduction of the relevant theoretical concepts and a brief summary of the hosts and the active ions studied. Chapter 3 discusses the experimental techniques used for fabricating and characterizing the laser gain media. Chapter 4 briefly describes the selected results achieved in this work, regarding the growth of the crystals, the physical and the spectroscopic characterizations. The CW and the passive *Q*-switching results obtained with Tm^{3+}- doped gain materials are presented in chapter 5. The laser results obtained with Er^{3+}, Ho^{3+} and (Ho^{3+},Tm^{3+}) co-doped gain materials are also discussed in this chapter. Finally, the conclusions and future works are given in chapter 6.

Chapter 2 Theoretical background

A general introduction of the relevant theoretical concepts and a brief summary of the hosts and the active ions studied are discussed in this chapter. The basic theory about waveguide modes is presented. The laser parameters in quasi-3-level systems are introduced and discussed. As femtosecond direct laser writing is the main method implemented for fabricating most of the waveguides used in this work, the fundamental physical processes involved in this method are presented. Pulsed laser generation by passive *Q*-switching technique is also discussed. For specific saturable absorbers implemented in this thesis work, the basics of the band structures, absorptions, and relaxation mechanisms are also addressed.

2.1 Optical waveguides

Optical waveguides (WGs) are structures that can confine and propagate light over a certain distance. They are constructed by having a high refractive index material (i.e. core) sandwiched/surrounded by materials with lower refractive indices (i.e., claddings). The confinement of the propagating light field could be along one dimension (1D) or 2D, constituting the planar and channel waveguide configuration, respectively. The cross-sectional geometry of the channels could be either rectangular or circular, depending on the fabrication method employed. The schematics of the different waveguide configurations are given in Fig 2.1

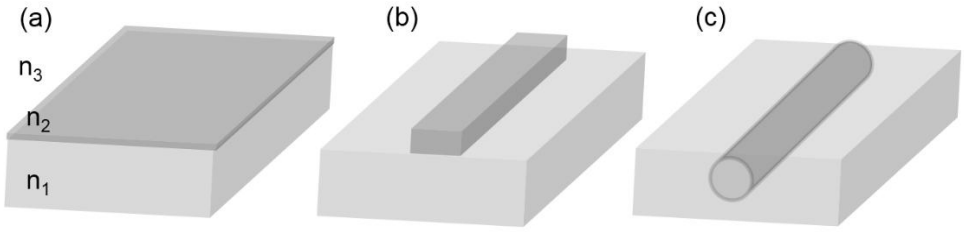

Figure 2.1 (a) Planar waveguide; Channel waveguide with (b) rectangular and (c) circular core geometry. n_1, and n_2 are the refractive indices of the substrate and the core regions, respectively. $n_2 > n_1$. n_3 is the upper cladding, in (a, b) this would be air.

When considering WGs, an obvious question that arises is, the nature (i.e. angle of incidence, spectral and spatial extent) of the light fields that would be confined and guided – the WG modes. It would be determined by the cross-sectional size of the core and the refractive index contrast with the cladding. In WGs, the propagation of the light fields could be described using the ray optics or the wave optics approaches. There is an important collection of scientific literature and textbooks discussing, in great detail, these approaches [28-31]. However, a brief summary will be given here, highlighting the concepts that were essential in this thesis work.

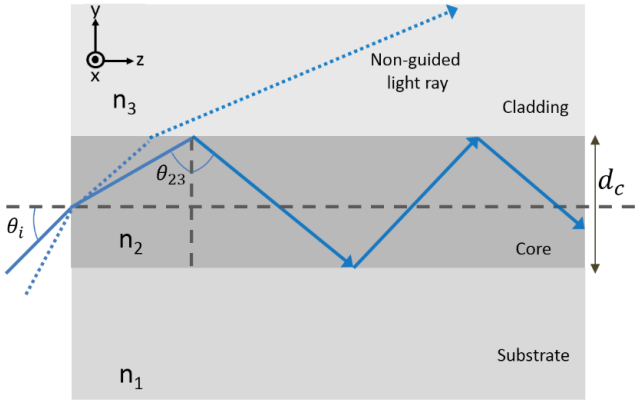

Figure 2.2. Light propagation by a successive total internal reflection (TIR) at the interfaces of a planar waveguide. n_1, n_2, and n_3 are the refractive indices of the substrate, the core, and the cladding regions, respectively. $n_2 > n_1$ and n_3.

A light ray, traveling from a high refractive index medium towards a lower one will undergo total internal reflection (TIR), if the angle of incidence at the interface θ_{23} is above a critical value (θ_c) set by the Snell's law, Fig. 2.2. However, not all the light rays that are incident at the input facet would satisfy the condition to undergo TIR. The maximum angle of incidence that is allowed θ_{i_max} determines the numerical aperture of the WG $N.A. = Sin\left(\theta_{i\_max}\right)$. Due to the TIR, the propagating light will undergo a polarization dependent phase shift, as described by the Goos–Hänchen effect [32, 33]. The propagation direction of such rays, traveling in a material with refractive index n_2, is described by the wavevector $\boldsymbol{k}$.

$$\boldsymbol{k} = k_0 n_2 \, \hat{k} = \frac{2\pi}{\lambda} n_2 \, \hat{k} \tag{2.1}$$

Where, k_0 is the free space wavevector and λ is the wavelength. After propagating over a distance of l_y, the beam would acquire an extra phase shift given by $\phi = k_0 n_2 \, l_y$. After each round-trip reflection at the interfaces, they must undergo a constructive interference – the total phase shift acquired must be integer multiples of 2π.

$$k_0 n_2 cos(\theta_2) 2d_c - \phi_1 - \phi_3 = \mathrm{m}2\pi \tag{2.2}$$

Where, $k_0 n_2 cos(\theta_2)$ represents the wavevector component along the y-axis (i.e. towards the interfaces, $\theta_{23} = \theta_2$), d_c is the thickness of the core with refractive index n_2 , ϕ_1 and ϕ_3 are the phase shifts acquired from the TIR, see Fig.2.2. Considering only light rays with transverse electric (TE) polarization, the phase shifts would be given as [34],

$$\tan\left(\frac{\phi_1}{2}\right) = \frac{\sqrt{(n_2 \, sin(\theta_2))^2 - {n_1}^2}}{n_2 \, cos(\theta_2)} \tag{2.3}$$

$$\tan\left(\frac{\phi_3}{2}\right) = \frac{\sqrt{(n_2 \, sin(\theta_2))^2 - {n_3}^2}}{n_2 \, cos(\theta_2)} \tag{2.4}$$

Using the propagation constant β (expressed in terms of the effective refractive index n_{eff}, see equation 2.5) and after inserting equations 2.3 and 2.4 into equation 2.2, the generalized mode guiding conditions for TE polarized light (propagating in a planar waveguide) could be derived, equation 2.6 [33, 34]. Following the same procedure, a similar expression could be derived for the transverse magnetic (TM) polarization.

$$\beta = k_0 n_2 \sin(\theta_2) = k_0 n_{eff} \tag{2.5}$$

$$[(k_0 n_2)^2 - \beta^2]^{1/2} d_c \; - tan^{-1}[\frac{\beta^2 - (k_0 n_1)^2}{(k_0 n_2)^2 - \beta^2}]^{1/2} \; - tan^{-1}[\frac{\beta^2 - (k_0 n_3)^2}{(k_0 n_2)^2 - \beta^2}]^{1/2} \; = m\pi \tag{2.6}$$

Equation 2.6 is a transcendental equation that could be solved numerically in order to analyse the number of modes that can be supported by a planar waveguide, along its guiding direction (i.e. the y-axis, in Fig.2.2).

For analysing the mode guiding conditions for WGs with channel geometry, the wave optics based analysis using Maxwell's equations could be applied. Such an analysis will also reveal the spatial field distribution of the modes in WGs with different cross-sectional geometries. The propagation of light fields in a medium without free charge ρ and current density J, is governed by the Maxwell's equations [28, 34].

$$\nabla \, X \, \boldsymbol{H} = \; \varepsilon \, \frac{\partial \boldsymbol{E}}{\partial t} \tag{2.7}$$

$$\nabla X \boldsymbol{E} = -\mu \frac{\partial \boldsymbol{H}}{\partial t} \tag{2.8}$$

$$\nabla . \boldsymbol{E} = 0 \tag{2.9}$$

$$\nabla . \boldsymbol{H} = 0 \tag{2.10}$$

Where, $\boldsymbol{E}$ and $\boldsymbol{H}$ are the electric and magnetic fields, ε and μ are the electric permittivity and the magnetic permeability of the medium, respectively. These equations govern, the nature of the electromagnetic (light) waves inside the medium. By combining and re-arranging them [28, 34], a single equation, in terms of one of the fields $\boldsymbol{E}(\boldsymbol{r},\boldsymbol{t})$ or $\boldsymbol{H}(\boldsymbol{r},\boldsymbol{t})$ – also known as the "wave equation" would be derived.

$$\nabla^2 \boldsymbol{E}(\boldsymbol{r},\boldsymbol{t}) - \varepsilon\mu \frac{\partial^2 \boldsymbol{E}(\boldsymbol{r},\boldsymbol{t})}{\partial t^2} = 0 \tag{2.11}$$

Where, $\boldsymbol{r} = x\boldsymbol{i} + y\boldsymbol{j} + z\boldsymbol{k}$ is the spatial vector. For a time-harmonic electric field $\boldsymbol{E}(\boldsymbol{r},\boldsymbol{t}) = E(r)\, e^{-i\omega t}$, oscillating in time with a single frequency ω (monochromatic), the time-independent wave equation, known as the Helmholtz equation would be derived from equation 2.11 [28].

$$\nabla^2 \boldsymbol{E}(\boldsymbol{r}) + \omega^2 \varepsilon\mu\, \boldsymbol{E}(\boldsymbol{r}) = 0 \tag{2.12}$$

In order to calculate the mode field distribution of the channel WGs, finite element method (FEM) based simulation tools (such as COMSOL Multiphysics ™) could be applied for solving the Helmholtz equation by applying the appropriate boundary conditions. From the intensity profile of the fundamental mode, the mode field diameter (MFD), taken at the $1/e^2$ value of the intensity, could be calculated by fitting with a Gaussian function which is expressed as,

$$I(y) = I_0 e^{-\frac{(y-y_0)^2}{2\sigma^2}} \tag{2.13}$$

Where, I_0 is the maximum intensity, σ is the standard deviation of the Gaussian function, y_0 is the spatial position around which the function is centered and y is the spatial distance. From the fitting, the corresponding MFD could be calculated as,

$$MFD = 4\sigma \tag{2.14}$$

2.2 Laser gain media

Laser gain media with a WG configuration would tightly confine and store the energy in the form of optical modes. Such a tight confinement will result in high optical intensity over the full propagation length of the WG [24]. Solid-state materials, such as crystals, glasses or ceramics, that incorporate active ions (dopants) could serve as the gain media.

For near-IR laser emissions, the active ions could be trivalent lanthanides (Ln^{3+}) such as neodymium (Nd^{3+}), holmium (Ho^{3+}), Erbium (Er^{3+}), thulium (Tm^{3+}) and ytterbium (Yb^{3+}) or transition metal ions such as titanium (Ti^{3+}) or chromium (Cr^{2+}, Cr^{3+}, Cr^{4+}) among others. In the latter case, the electronic transitions responsible for the laser emission have strong interaction with the phonon modes of the host material resulting in a broader gain bandwidth.

The trivalent Ln^{3+} ions have a ground state electronic configuration that consists of a core which is similar to Xenon and additional higher orbital electrons. In the case of Xenon, its electronic configuration is expressed as: $1s^2 2s^2 2p^6 3s^2 3p^6 3d^{10} 4s^2 4p^6 4d^{10} 5s^2 5p^6$. Its shells with n=1, 2, 3 and the s, p and d sub-shells of n = 4 are completely

filled. However, its 4f sub-shell is completely empty while the outer lying 5s and 5p sub-shells are filled. The Ho^{3+} ion has 10 electrons in its 4f sub-shell and has an electronic configuration of [Xe] $4f^{10}$. Similarly, Er^{3+} and Tm^{3+} have an extra 11 and 12 electrons in their 4f sub-shells and have [Xe] $4f^{11}$ and [Xe] $4f^{12}$ electronic configurations, respectively. The 4f – 4f optical transitions in Ln^{3+} ions are shielded from the host's lattice field experiencing narrow linewidths in their electronic transitions. Those fields are considered as a small perturbation upon the 4f sub-levels determining the extent of the stark splitting in the multiplets (originating from the spin-orbital (LS) interactions), Fig 2.3 [35].

The host materials incorporating the Ln^{3+} ions must have good optical, thermal and mechanical properties. The absorption and emission cross-sections of the active Ln^{3+} ions are influenced by the host materials. The larger those cross-sections are, the more efficient the corresponding interactions between the ions and the photons. The interaction also depends on the wavelength and polarization of the photons. The thermal properties of the host, such as the thermal conductivity and thermo-optic coefficients, determine the cooling efficiency and temperature induced refractive index changes, respectively. During fs-DLW of channel WGs, the thermal properties of the material determine the nature of the modification at the focus volume. The mechanical properties are important during sample preparations (cutting and polishing) as well as withstanding high pump powers.

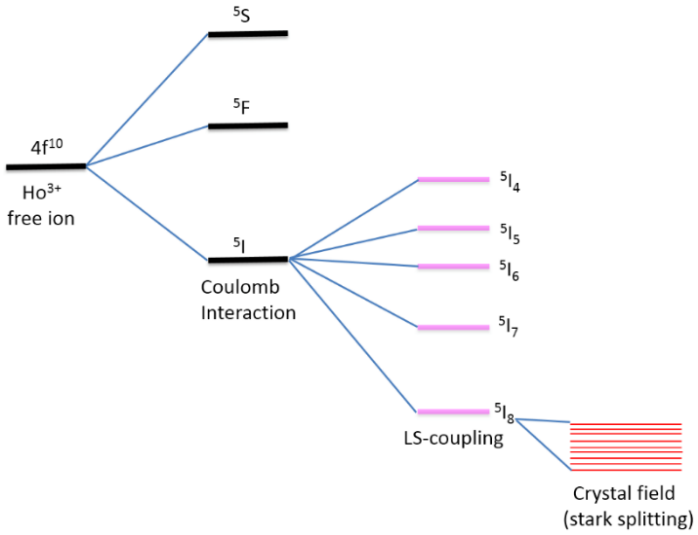

Figure 2.3. Energy level structure of Ho^{3+} ions showing the different splitting mechanisms and stark splitting levels. Reproduced from [35].

2.2.1 Monoclinic double tungstate crystal

The crystal structure of potassium rare-earth double tungstate $KRE(WO_4)_2$ (hereafter KREW) was first reported in early 1968 [36]. It belongs to the monoclinic system ($a \neq b \neq c$; $\alpha = \gamma = 90^0$, $\beta > 90^0$) with C2/*c* space group, where the unit cell contains 4 K atoms, 4 RE atoms, 8 W atoms, and 32 O atoms [37]. In the unit cell, the RE is eight-fold coordinated by oxygen forming distorted square antiprisms. The active Ln^{3+} dopants substitute for the RE^{3+} ions from their local site symmetry. The RE^{3+}- RE^{3+} interatomic distance determines the energy transfer processes between the neighbouring Ln^{3+} ions, after substitution during the doping process. This distance in KLuW and KGdW crystals is 4.045 A^0 and 4.070 A^0, respectively, favouring higher doping levels without significant luminescence quenching [37, 38].

The units with W_2O_8 are constituted from two distorted octahedra (WO_6) sharing O – O edges. They also make a double O chains along the crystallographic *c* – axis of the KREW crystals. The single and double oxygen bonds constitute the characteristic stretching and bending vibrations of the KREW crystals. After the fs-DLW procedure, by monitoring the changes in the vibrational modes of the bonds, information regarding the nature and extent of the laser induced damages are revealed (cf. chapter 4).

Monoclinic KREWs are biaxial crystals. Nevertheless, the 3 orthogonal principal optical axes, N_p, N_m, and N_g are used to define their optical indicatrix. The refractive indices of the crystals along these axes are $n_p < n_m < n_g$. The N_g and N_m principal optical axes are located in the *a-c* crystallographic plane while the N_p axis is parallel to the *b* – crystallographic direction, which is also the optimum crystal growth direction for high quality crystals. With respect to the *c* – crystallographic axis, the N_g optical axis is located clockwise (assuming the *b* –crystallographic axis pointing towards the observer) at an angle κ' of 18.5^0 (KLuW and KYW) and 21.5^0 (KGdW) [38-40], Fig. 2.4.

The Ln^{3+} doped KREW crystals would serve as laser gain media which could broadly be classified as 3-level, 4-level or quasi-3-level systems, Fig. 2.5. The pump source (exciting the ions to the pump level) would create a population inversion between the upper and lower laser levels. If the ground level from where the ions are being pumped and the lower laser level are the same, as in the 3-level systems, higher pump powers would be required to achieve population inversion. A typical example of such a laser system is Cr^{3+}:Al_2O_3 (ruby) which was the first laser demonstrated by Maiman [1]. The transitions from the pump level to the upper laser level are fast and non-radiative processes.

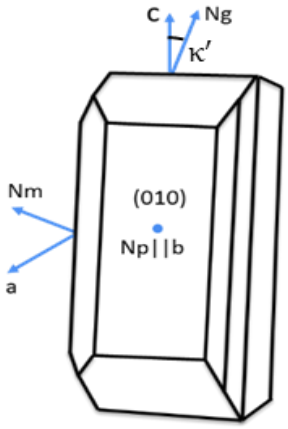

Figure 2.4. The orientation of the principal optical axes with respect to the crystallographic axes in the KREW crystals.

In 4-level systems, the lower laser level is well above the ground level and doesn't possess appreciable population density at room temperature. Such systems are known to have a lower lasing threshold due to the ease to achieve population inversion and negligible reabsorption of emitted laser photons. Neodymium based lasers operating at ~ 1 µm are 4-level systems [41] when pumped around 0.8 µm.

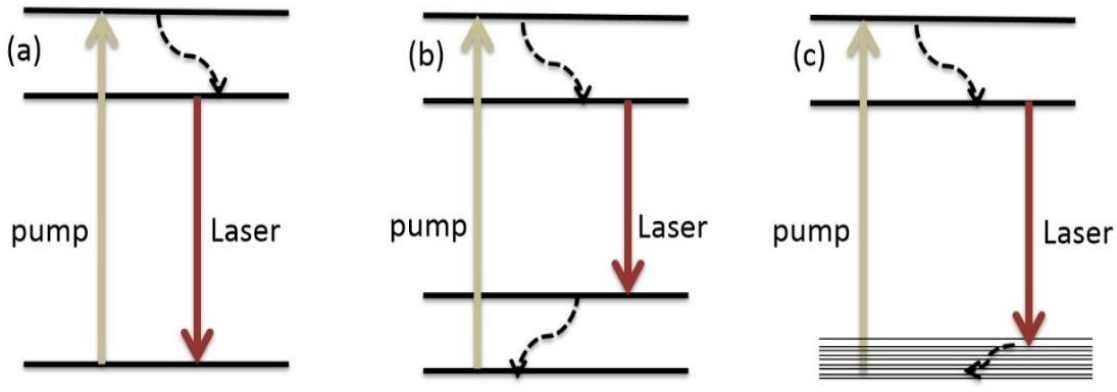

Figure 2.5. Energy level schematic diagrams of (a) 3 – level; (b) 4 – level and (c) quasi-3-level laser systems.

In quasi-3-level systems, the lower laser level is an upper stark component of the ground level multiplet and it is thermally populated at room temperature, leading to laser reabsorption losses at the weakly pumped region of the medium. Consequently, as compared to 4-level systems, they have a higher lasing threshold. The laser

emission wavelength also depends on the cavity losses for such quasi-3-level systems. For higher losses, the gain has to be large enough to compensate them. This would require higher population inversion (excitation level), for which the peak of the gain spectra is shifted towards shorter wavelengths.

It should be noted that longer wavelengths are less affected by the reabsorption losses. At lower inversion levels, where a significant thermal population exists, longer wavelengths would prevail to reach the laser threshold. While for high inversion levels, the thermally populated lower multiplet is depleted and the reabsorption losses are reduced, hence the shorter wavelength would dominate. Hence, increasing the output coupling (OC) transmission of the cavity mirrors would result in a blue shift in the lasing wavelength for the quasi-3-level systems. Er^{3+} and Tm^{3+} doped gain medium operates in such a system.

2.2.2 Tm^{3+} ion doped KLuW crystal

The ~ 2 µm emission from Tm^{3+} ion is described as a quasi – 3 – level system. The energy level diagram of the Tm^{3+} ion is given in Fig. 2.6, along with the various transitions and energy transfer processes involved. The excitation of the Tm^{3+} laser is from $^3H_6 \rightarrow {}^3H_4$ energy levels using a pump source with a wavelength of λ_P ~ 800 nm. The unquenched lifetime of the $^3H_4$ pump level is short τ = 240 µs [42] and a subsequent phonon assisted non-radiative decay to $^3F_4$ upper laser level would take place. The laser transition towards the upper stark levels of the $^3H_6$ energy level would generate the λ_L ~ 1.84 µm emission (typical for Tm^{3+}-doped WG lasers, using high OC transmissions). The stokes efficiency of such laser transitions would be $\eta_{st} = \lambda_P/\lambda_L$ ~ 0.43. But thanks to the non-radiative cross – relaxation (CR) processes happening between two adjacent enough Tm^{3+} ions, the upper laser level ($^3F_4$) would be populated with the so-called “two-for-one” scheme [43].

An electron in one of the ions, de-excited from its pump level to the upper laser level, would be accompanied by a ground level electron (in the neighbouring ion) being excited to the upper laser level ($^3H_4 + {}^3H_6 \rightarrow {}^3F_4 + {}^3F_4$). Consequently, one pump photon will generate two laser photons. This process is more efficient for higher Tm^{3+}-doping levels, whose pump quantum efficiency η_q approaches ~ 2. Such a special advantage in Tm^{3+} -doped lasers would increase the stokes efficiency to $\eta_{st} = 2\lambda_P/\lambda_L \sim 0.86$. As the stokes efficiency is related to the heat generated in the crystals (i.e. heal loading) $\eta_h = 1 - \eta_{st}$, an efficient CR process would lead to lower thermal stress favouring power scalability.

In addition to the CR, other processes such as excited state absorption (ESA) also play a significant role in the efficiency of Tm^{3+} -doped lasers. The electrons in $^3H_4$ and $^3H_5$ (after non-radiative decay from $^3H_4$) would get excited to the higher level multiplet ($^1G_4$) by a pump photon, from where they would decay back to $^3H_5$, $^3F_4$, and $^3H_6$ levels with up-conversion luminescence (UCL) in the near-infrared (~ 770 nm), red (~ 650 nm) and blue (~ 480 nm) emissions, respectively. A second CR process ($^1G_4 + {}^3H_6 \rightarrow {}^3F_3 + {}^3F_4$) is also possible, further contributing to the population of the upper laser level.

Typically, in Tm^{3+} -doped WG lasers (viewed under lasing conditions), bright blue UCL could be easily noticed (cf. chapter 5). Such up-conversion losses further contribute to the heat loading in the sample, necessitating efficient heat management. This is especially crucial considering the quasi-3-level nature, where the lower laser level is thermally populated. It should be noted that undoped KLuW crystals have a thermal conductivity κ of 3.41 W/mK, 2.34 W/mK and 3.59 W/mK along their N_m, N_p and N_g principal optical axes, respectively [44]. These values are lower compared to other undoped host materials such as YAG (11 W/mK), Vanadates (averaged to 5.1 W/mK) and fluorides (averaged to 4.3 W/mK) [45].

An alternative pumping scheme for Tm^{3+} -doped lasers is the so-called in-band pumping (for instance, at ~ 1.68 µm from an Er^{3+}/ Yb^{3+} Raman fiber laser), where the ground state electrons are directly excited to the upper laser level ($^3H_6 \rightarrow {}^3F_4$ transition). For such an in-band pumping, as compared to ~ 0.8 µm pump, processes such as multi-phonon non-radiative decay ($^3H_4 \rightarrow {}^3H_5 \rightarrow {}^3F_4$ transition), ESA and its succeeding up-conversion losses would be alleviated [46]. Hence, the Tm^{3+}-doped lasers would have a higher stokes efficiency ($\eta_{st} \sim 0.88$) and a lower quantum defect leading to a higher laser efficiency as well as lower thermal loading.

The spectroscopic characterization of the laser materials are needed for knowing the optimum pump wavelength as well as the highest laser gain. In the quasi-3-level laser systems, the gain cross-sections calculated from the absorption and emission cross-sections are used to estimate the expected laser emission wavelength. Additionally, for biaxial crystals, the dominating laser polarization will be determined from the gain cross-sections (calculated as a function of wavelength) along the different crystal orientations. Such characterizations were already investigated and reported for the different Ln^{3+} ions and KREW host materials [47-49].

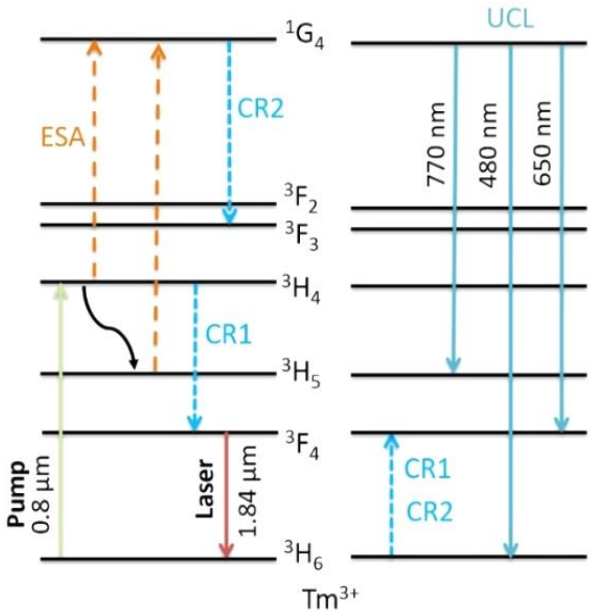

Figure 2.6. Energy-level scheme of Tm^{3+} ions [50]: ESA – excited state absorption, CR1 and CR2 – cross-relaxation mechanisms, UCL – up-conversion luminescence.

The absorption cross-section σ_a could be calculated from an optical transmission measurement. Such measurement depends on the orientation of the crystal, because of the anisotropy (i.e. along N_m, N_p, or N_g, principal optical axes). Once the absorption cross-sections are known, the emission cross-sections can be calculated using the reciprocity method [35]. In this method, the knowledge of the individual stark levels of the manifolds involved in the transitions are needed. For the Tm^{3+}-doped KLuW laser crystal they were reported in [48]. However, such an information might not always be available, especially for new laser materials. Consequently, other method known as the modified reciprocity method [51] was developed to calculate the emission cross-section, from the radiative lifetime τ_{rad} (which could be experimentally measured) and the polarized absorption cross-sections of the laser materials. Other method known as the Füchtbauer-Ladenburg equation [35] which requires the radiative lifetime and the measured fluorescence spectra could also be used. For the quasi-3-level system, such a measurement can be affected by the reabsorption of the fluorescence signal.

After determining the absorption and emission cross-sections, the gain cross-section $\sigma_g(\lambda)$ can be calculated as, $\sigma_g(\lambda) = \beta\sigma_e(\lambda) - (1-\beta)\sigma_a(\lambda)$ Where, β is the population inversion level calculated as $\beta = N_u/N_T$, N_u is the population density in the upper laser level and N_T is the total population density. Using the gain cross-sections, the relation between the round-trip gain G and total round-trip cavity losses δ' can be deduced, which is important to understand the onset of the laser emissions.

$$G = \sigma_g(\lambda)N_T 2l = \delta' = -\ln(1 - L_{in}) - \ln(1 - T_{OC}) \quad (2.15)$$

Where l is the cavity (WG) length, L_{in} is the intrinsic cavity loss (for WG lasers – propagation losses) and T_{OC} is the transmission of the output coupling mirror. For different cavity losses or T_{OC}, the required gain (population inversion level β) to reach the lasing condition would also be different. The absorption, emission and the calculated gain cross-sections of Tm^{3+}-doped KLuW crystal are presented in Fig. 2.7 and 2.8.

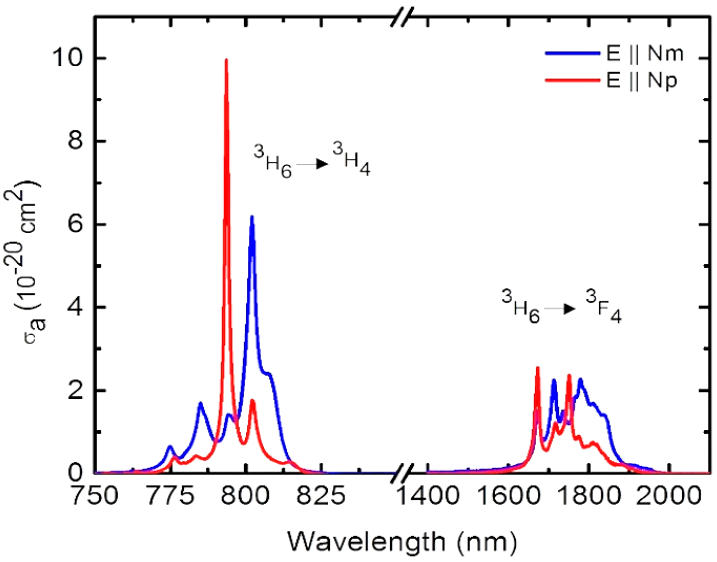

Figure 2.7. Polarized absorption cross-sections for $^3H_6 \rightarrow {}^3H_4$ and $^3H_6 \rightarrow {}^3F_4$ transitions of Tm^{3+}:KLuW [50].

For the $^3H_6 \rightarrow {}^3H_4$ transition, the maximum absorption cross-section is σ_a = 6.2 x 10^{-20} cm^2 at 802 nm with a full width at half maximum (FWHM) linewidth of ~ 4.5 nm, for E || N_m polarization. On the other hand, E || N_p polarization has larger σ_a = 9.9 x 10^{-20} cm^2 with a much narrower linewidth (~ 1.5 nm) at 793.5 nm [50]. The availability of high-power commercial laser diodes near 800 nm makes pumping along the N_m orientation more interesting because of their broadband nature although most of the fiber-coupled diode lasers are unpolarized. Additionally, considering the slight variation of the pump's central wavelength (due to variation in the operating temperature of the laser diodes), a broader absorption linewidth would have an advantage (i.e. less sensitivity of the laser to the pump wavelength). For direct excitation towards the upper laser level ($^3H_6 \rightarrow {}^3F_4$ transition) with ~ 1.68 μm pump, the absorption cross-sections are slightly lower, σ_a = 9.8 x 10^{-21} cm^2 (|| N_m) and σ_a = 9.2 x 10^{-21} cm^2 (|| N_p), Fig 2.7.

The emission cross-sections, calculated using the reciprocity method from the absorption cross-section values, Fig 2.8 (a), for the $^3F_4 \rightarrow {}^3H_6$ transition are σ_e = 3.74 x 10^{-20} cm^2 at 1840.9 nm (for E || N_m), while it is slightly lower σ_e = 1.57 x 10^{-20} cm^2 at a shorter wavelength (1820.3 nm) for E || N_p.

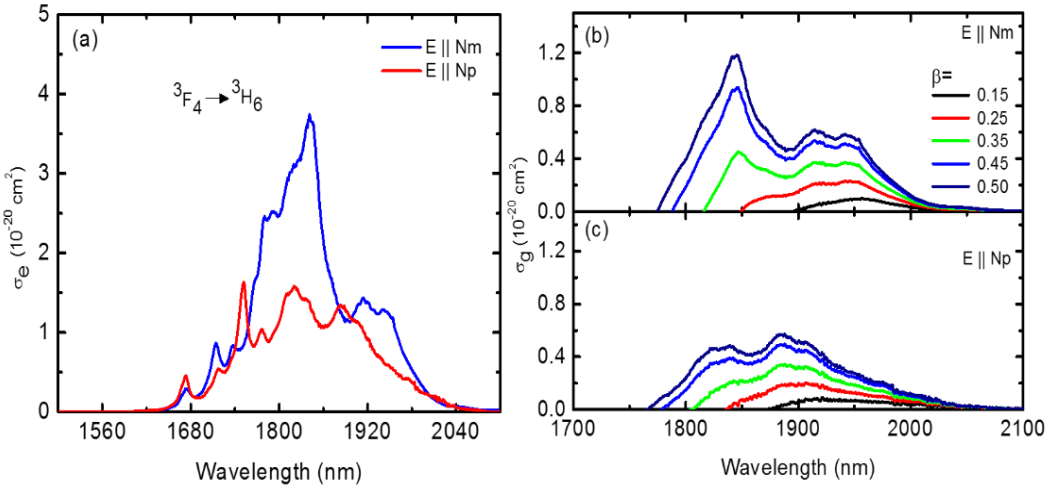

Figure 2.8. (a) Calculated emission cross-section; calculated gain cross-sections for (b) E || N_m and (c) E || N_p polarization, for various population inversion levels β [50].

The gain cross-section indicating the spectral extent of the cavity gain for a range of inversion levels β can be observed in Fig 2.8 (b, c). Larger gain cross-section values would be achieved for the E || N_m orientation as compared to E || N_p. This would mean that the emission whose polarization is along E || N_m, would overcome the cavity losses and reach its lasing threshold first (i.e. the emitted laser polarization would be naturally selected by the gain anisotropy of the medium).

2.2.3 Er^{3+} ion doped KLuW crystal

The Erbium (Er^{3+}) ion is known for its laser emission around 1.5 µm due to the $^4I_{13/2} \rightarrow {}^4I_{15/2}$ transition, Fig.2.9. It possesses a complex energy level scheme with several resonant energy-differences between multiplets. This determines various possible transfer processes of electronic excitation, e.g., energy-transfer up-conversion (ETU), ESA or CR, Fig.2.9. For the 1.5 µm laser emission, all these these processes are parasitic limiting the laser efficiency and causing unwanted heat loading. Thus, the selection of a proper Er^{3+} -doping concentration, as well as a pumping scheme is critical.

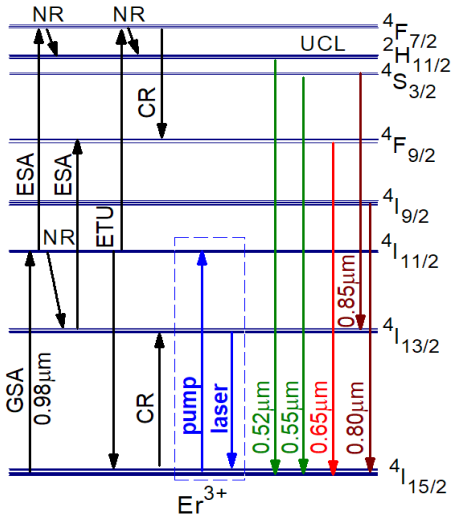

Figure 2.9. Energy-level scheme of Er^{3+}:KLuW [52] and the main spectroscopic processes: GSA and ESA – ground- and excited-state absorption, respectively, ETU – energy-transfer up-conversion, CR – cross-relaxation, UCL – up-conversion luminescence, NR: non-radiative relaxation.

A well-known scheme is (Er^{3+},Yb^{3+}) co-doping with Yb^{3+} ions serving as a sensitizer and providing a strong absorption at 0.98 µm (suited for InGaAs laser diode pumping). For a very limited number of materials like phosphate glasses, this scheme is rather efficient [53]. However, the poor thermal properties of glasses limit the output power. In-band pumping of Er^{3+} ions at ~1.5 µm (directly to the $^4I_{13/2}$ upper laser level) has proven its potential for power-scalable crystalline lasers, e.g., Er^{3+}:YAG [54], but the suitable pump sources are not widely spread and are expensive. Pumping of singly Er^{3+}- doped crystals at 0.98 µm (to the $^4I_{11/2}$ level) can be a cheap alternative, although the optical-to-optical efficiency of such lasers is limited by the low $^4I_{15/2} \rightarrow {}^4I_{11/2}$ absorption. Moreover, the Stokes efficiency of such pumping, for the 1.5 µm laser transition, would be $\eta_{st} \sim 0.65$.

For Er^{3+}- doped KLuW crystal under 0.98 µm excitation, the most intense UCL emissions are expected in the green (0.52-0.56 µm) due to the transition from the $^2H_{11/2} + {}^4S_{3/2}$ states to the ground state ($^4I_{15/2}$). Much weaker emissions in the red (0.65-0.67 µm) and near-IR (0.79-0.83 µm and 0.84-0.86 µm) spectral regions are also present, due to the $^4F_{9/2} \rightarrow {}^4I_{15/2}$, $^4I_{9/2} \rightarrow {}^4I_{15/2}$ and $^4S_{3/2} \rightarrow {}^4I_{13/2}$ transitions, respectively.

Pumping at ~ 0.98 µm, the excitation corresponds to the ground-state absorption (GSA) transition, $^4I_{15/2} \rightarrow {}^4I_{11/2}$. The lifetime of the $^4I_{11/2}$ state in KREW is relatively long ($\tau \sim 150$ µs [40]) and the $^4I_{11/2} \rightarrow {}^4F_{7/2}$ ESA process is rather probable. The ETU process, $^4I_{11/2} + {}^4I_{11/2} \rightarrow {}^4F_{7/2} + {}^4I_{15/2}$ can additionally populate the higher-lying $^4F_{7/2}$ state. The subsequent non-radiative (NR) relaxation populates the green-emitting levels $^2H_{11/2}$+$^4S_{3/2}$, for which $\tau \sim 30$ µs [40]. The red-emitting state ($^4F_{9/2}$) can be populated by a NR relaxation from the upper-lying states or by a second but

less probable ESA process ($^4I_{13/2} \rightarrow {}^4F_{9/2}$) that occur after the NR relaxation from the $^4I_{11/2}$ pump level. The value of τ for this state is rather short, ~1 μs [40]. The possible CR, $^4F_{7/2} + {}^4I_{15/2} \rightarrow {}^4F_{9/2} + {}^4I_{13/2}$, which is known to assist the population of the red-emitting state, is inefficient for low Er^{3+} concentrations leading to weak red UCL.

The polarized transition cross-sections of Er^{3+} ions in KLuW are shown in Fig.2.10 (a-c). For the $^4I_{15/2} \rightarrow {}^4I_{11/2}$ pump transition, the maximum absorption cross-sections are σ_a = 1.21 x 10^{-20} cm^2 at 979.1 nm with a linewidth (FWHM) of ~ 9.3 nm (for E || N_m) and σ_a = 1.27 x 10^{-20} cm^2 at 981.6 nm with a linewidth of ~ 5 nm (for E || N_p), Fig.2.10(a). The broader linewidths are more favourable for implementing diode pumped Er^{3+}:KLuW WG lasers. For an unpolarized pumping source, the σ_a values averaged over both polarizations (E || N_m and E || N_p) would be considered. From the absorption cross-section values of the $^4I_{15/2} \rightarrow {}^4I_{13/2}$ transition, the corresponding emission cross-sections calculated using the reciprocity method, Fig.2.10 (b, c). Thus, the E || N_m polarization shows a maximum value of σ_e = 3.0 x 10^{-20} cm^2 at 1534.7 nm while for E || N_p, it is slightly lower, σ_e = 1.9 x 10^{-20} cm^2 at 1534.8 nm [55].

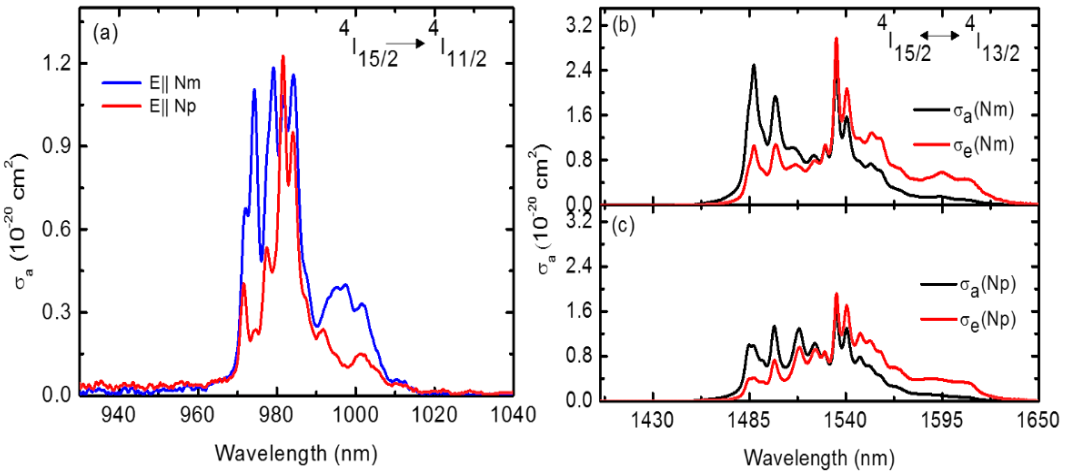

Figure 2.10. (a) Polarized absorption cross-sections for the $^4I_{15/2} \rightarrow {}^4I_{11/2}$ transition of Er^{3+}:KLuW; Absorption and emission cross-sections of the $^4I_{15/2} \leftrightarrow {}^4I_{13/2}$ transition for (b) N_m and (c) N_p crystal orientations [55].

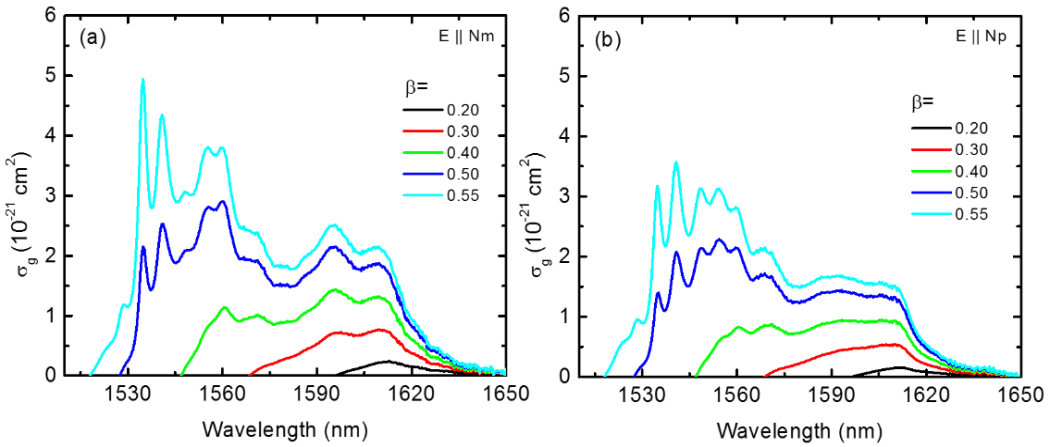

Figure 2.11. Calculated gain cross-sections for $^4I_{15/2} \rightarrow {}^4I_{11/2}$ transition of Er^{3+}:KLuW crystal for (a) E || N_m and (b) E || N_p polarization, for various population inversion levels β [55].

The gain cross-sections for various inversion levels are shown in Fig. 2.11 (a, b). For lower inversion levels $\beta < 0.3$, the gain spectra had a local peak at ~ 1610 nm. However, for very high $\beta > 0.5$ (i.e. strongly bleached lower laser levels), the peak of the gain spectra shifts to ~ 1535 nm. The higher gain values for E || N_m polarization points that, it would be the selected laser emission polarization.

2.2.4 Ho^{3+} ion doped KGdW crystal

The laser emission from Ho^{3+} ions typically occurs slightly above 2 μm due to the $^5I_7 \rightarrow {}^5I_8$ transition. One of the common schemes for exciting the Ho^{3+} ions is co-doping them with Tm^{3+} ions. In such case, the pump would be ~ 800 nm from AlGaAs laser diodes or a Ti:Sapphire laser, assisted with the energy transfer (ET) process between the Tm^{3+} ($^3F_4$) and Ho^{3+} ($^5I_7$) ions: $^3F_4 + {}^5I_8 \rightarrow {}^3H_6 + {}^5I_7$ transition, Fig.2.12. Alternatively, the $^3F_4$ (Tm^{3+}) level could also be populated by a ~ 1.6 μm in-band pumping, using, for instance, an Er^{3+}/ Yb^{3+}- doped Raman fiber laser.

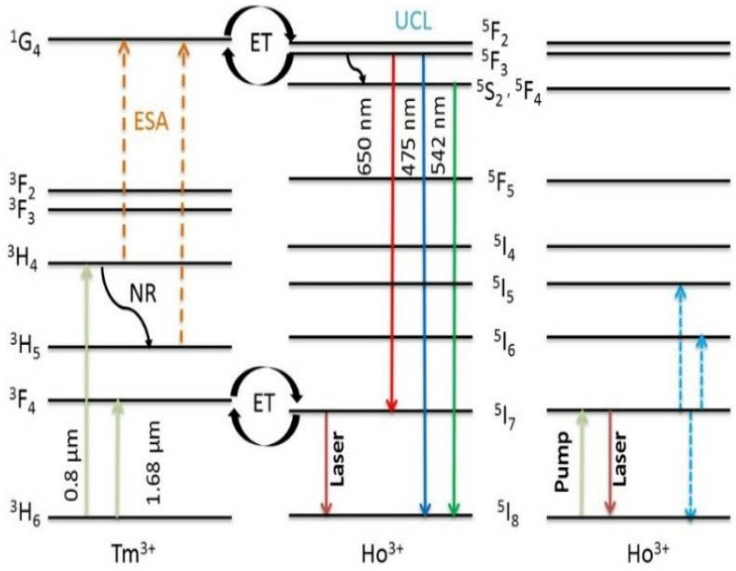

Figure 2.12. Energy-level scheme of (Tm^{3+}, Ho^{3+}) co-doped and Ho^{3+} doped KREW [56], with the main spectroscopic processes: ESA – excited-state absorption, ET – energy-transfer, UCL – up-conversion luminescence, NR: non-radiative relaxation.

As it was previously described, the ESA processes in Tm^{3+} ions would populate the $^1G_4$ energy level, from where a second ET process to the $^5F_3$ Ho^{3+} level may well happen. Subsequently, from the $^5F_3$ level, NR relaxation towards the $^5S_2 + {}^5F_4$ Ho^{3+} level, followed by a green (542 nm) UCL towards the $^5I_8$ ground level is possible. Direct UCL transitions, $^5F_3 \rightarrow {}^5I_7$ (~ 650 nm, red) and $^5F_3 \rightarrow {}^5I_8$ (~ 475 nm, blue) are also possible [56]. Hence, due to the various up-conversion processes, the (Tm^{3+}, Ho^{3+}) co-doped laser medium would suffer from significant thermal loading, demanding a proper optimization of the co-doping ratios and an efficient cooling scheme [57]. Furthermore, the finite efficiency of the ET process would also limit the Ho^{3+} lasing performance, as some of the pump power would be kept in the excited Tm^{3+} ions [58].

Another approach for the excitation of the Ho^{3+} ions is the so-called in-band (resonant) pumping where the electrons are directly excited to the upper laser level ($^5I_8 \rightarrow {}^5I_7$ transitions). This could be accomplished using AlGaIn-AsSb laser diodes [59], Tm^{3+} – doped fibers [60] or solid-state lasers [58] emitting slightly below 2 μm. The very close pump (λ_P ~ 1960 nm) and laser (λ_L ~ 2054 nm) photon energies would result in a rather high stokes efficiency η_{st} ~ 0.95, favouring a high slope efficiency and minimizing the heat loading. However, for high inversion levels, UC processes such as $^5I_7 + {}^5I_7 \rightarrow {}^5I_8 + {}^5I_6$ and $^5I_7 + {}^5I_7 \rightarrow {}^5I_8 + {}^5I_5$ transitions, assisted by the lattice phonons, are also possible.

The polarized absorption and calculated emission cross-sections of the $^5I_7 \leftrightarrow {}^5I_8$ transitions in Ho^{3+}-doped KGdW laser medium are shown in Fig.2.13. For the $^5I_8 \rightarrow {}^5I_7$ pump transition, the maximum σ_a = 2.0 x 10^{-20} cm^2 (E || N_m) located at 1961 nm would be spectrally suitable for implementing a Tm^{3+}:KLuW microchip laser based pumping. For E || N_p polarization, the absorption maximum (at 1959 nm) is lower, σ_a = 1.1 x 10^{-20} cm^2, Fig.2.13 (a, b) [61]. The peaks of the emission cross-sections are located at 2054 nm (σ_e = 2.7 x 10^{-20} cm^2) and 2020 nm (σ_e = 1.5 x 10^{-20} cm^2), for E || N_m and E || N_p respectively. The calculated gain cross-sections reveal distinct characteristics: the E || N_m is the dominant polarization and depending on the inversion ratio, $\beta = N_2(^5I_7)/N_{Ho}$, laser operation is expected around 2070 nm or 2054 nm, Fig.2.13 (c, d).

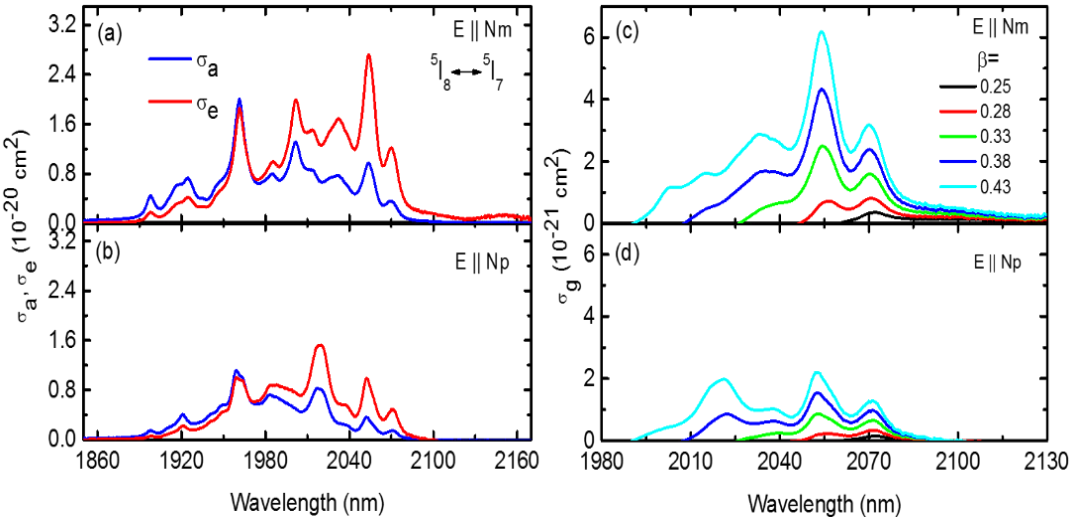

Figure 2.13. Polarized absorption and emission cross-sections for $^5I_7 \leftrightarrow {}^5I_8$ transition of Ho^{3+}:KGdW [61] for (a) E || N_m, (b) E || Np polarization; calculated gain cross-sections for (c) E || Nm and (d) E || Np polarization, for different population inversion levels β.

2.3 Fundamentals of waveguide fabrication

Several methods have been used to fabricate WGs based on Ln^{3+} doped laser materials. A combination of non-aqueous tape casting and vacuum sintering method was used for fabricating multilayer YAG composite layers doped with Nd^{3+} [62] and Tm^{3+} [63] ions. The direct-bonding method, where polished materials are joined together by van der Waals intermolecular forces, for making Yb^{3+} and Tm^{3+} doped WG structures was reported in [64, 65]. A combination of ion-diffusion with laser ablation was used to fabricate a ridge WG structure in Nd^{3+}: $LiNbO_3$ crystal [66]. The fabrication of a planar WG in Er^{3+}/Yb^{3+} doped silicate glass was achieved using a lower refractive index optical barrier created with proton implantation [67]. Reactive co-sputtering was also used to fabricate Tm^{3+}:Al_2O_3 WGs on Complementary Metal–Oxide–Semiconductor (CMOS) compatible silicon chip [68]. A layer – by – layer crystal film growth of Yb^{3+} doped YAG was also reported by the pulsed laser deposition (PLD) method [69]. This method, while being suitable for simple cubic oxides, is challenging for growing layers of oxides with monoclinic structure, as a deviation from stoichiometry or formation of unwanted crystal phases could occur [70].

In this work, for growing single crystalline Ln^{3+} doped KREW layers, the well-known liquid phase epitaxy (LPE) method was implemented. It is a non-vacuum method, where high quality single crystalline layers could be grown on an oriented substrate using supersaturated molten solutions. The simple and low-cost equipment's involved, as well as the high growth rates of the layers makes LPE one of the most widely used WG fabrication method. Using this method, Yb^{3+}:KYW layers on undoped KYW substrate [71], Nd^{3+} doped yttrium aluminum borate ($YAl_3(BO_3)_4$) films on un-doped $YAl_3(BO_3)_4$ substrates [72], (Er^{3+}, Yb^{3+}) [73] doped lattice-matched layers grown onto undoped KYW substrates, Tm^{3+}:$KY_{1-x-y}Gd_xLu_y(WO_4)_2$ [74] and Ho^{3+}:KYW [75] layers grown on undoped KYW substrates were grown and further utilized as amplifiers, WG and thin-disk lasers operating in ~ 1µm – 2 µm spectral ranges. However, the long fabrication time (i.e. needed for the substrate growth and preparation, for the growth of the active layer and the subsequent cutting and polishing processes) is the drawback of the LPE method.

Diamond saw dicing is a method that is gaining an interest in the field of optics, for making channel WGs. In combination with other fabrication techniques, WGs with advanced functionalities have been already demonstrated using this method [76]. A proper choice of the dicing blade and the fabrication parameters leads to a good quality ridge (channel) WG. Femtosecond direct laser writing (fs-DLW) also referred to as ultrafast laser inscription (ULI) was also implemented in this thesis work for fabricating channel WGs in Ln^{3+} doped KREW materials. Fs-DLW is a relatively new WG fabrication approach [77] where the output of an ultrafast (fs) oscillator is tightly focused in a transparent laser material causing a permanent variation of its refractive index. An inscription

of a three-dimensional structure may thus lead to the waveguiding behaviour. Fs-DLW is attractive because it allows for fabricating a variety of photonic microstructures in different materials (from glasses to crystals and ceramics) [78]. As fs-DLW was the main method implemented for fabricating most of the WGs used in this thesis, the fundamental physical processes and the fabrication parameters involved in this method are addressed in the subsequent sections.

The near-infrared radiation from laser sources such as a Ti:sapphire (~ 800 nm) and Yb doped fiber lasers (~ 1 μm) are not absorbed by undoped dielectric materials that are relevant for applications in photonics [78]. However, the high peak intensity generated from tightly focused fs pulses from such laser sources encounters nonlinear absorption inside the dielectric materials. This results in the excitation of the valance band electrons to the conduction band, after absorbing multiple photons - multiphoton absorption and/or by quantum tunneling - due to strong field induced band structure modification [79]. The electrons in the conduction band also interact with the laser pulse (free carrier absorption) and collide with other bound electrons resulting impact (avalanche) ionization. For the ultrashort (fs) laser pulses, the laser-matter interaction time is significantly shorter than the lattice heating time (~ ps), resulting in a negligible thermal coupling of the electrons and lattice ions [80]. Once the laser pulse has passed, it leaves a "hot" free electron plasma that subsequently transfers its energy to the lattice ions, inducing material modifications [78, 79]. The nature of the induced modifications depends on the properties of the materials such as its refractive index, thermal conductivity and the bandgap. It also depends on other experimental parameters such as the pulse duration, repetition frequency, pulse energy, polarization, focusing optics and translation speed [79, 81].

In crystals, due to the laser induced damage (at the focal volume), there is local amorphization of the crystalline material leading to lower refractive index [82]. As the amorphized volume expands, it induces a local stress in the immediate vicinity of the damage track modifying (increasing) the refractive index through the stress-optic effect [79]. The characteristics of the modification could be different along the different crystal orientations, resulting in a birefringent optical behaviour [83]. In glasses, after the laser pulse has traversed, melting and rapid quenching at the focal volume results in local densification and an increase in the refractive index [82]. As the modification occurs directly at the focal volume (not indirectly through stress-optic effect like in crystals), higher refractive index contrast could be achieved in glasses favouring more compact WG structures. However, the better thermal conductivity, higher damage threshold and the possibility to incorporate higher doping levels without significant luminescence quenching as well as achieving polarized laser emission, make crystals the favoured WG laser media [78, 82].

The fabricated WGs are generally classified depending upon how the core region is defined with respect to the laser modified regions. In the literature, one of the well-accepted classifications is those discussed in [78] as Type I, Type II and Type III WGs, Fig 2.14. If the core region is located inside the laser modified track, having a higher refractive index than the unmodified bulk, it is regarded as Type I WG. Such WGs have been implemented in various glasses including chalcogenide [84], bismuth-borate [85] and germanate [86]. Since the light is confined inside the focal volume, the core geometry could be tailored for fabricating more advanced 3D structures using the multi-scan procedure [87]. Only a few crystals, Nd^{3+}:YCOB [88], ZnSe [89], under specific conditions have shown a refractive index increase at the laser damaged volume.

In Type II WGs, the core region is indirectly defined through the stress induced refractive index increase near the vicinity of the damage track that has undergone a local volume expansion. In this case, the light confining and guiding could be accomplished near the top or bottom apex of the damage track or to its left/right sides. Considering KREW materials, Yb^{3+}:KYW [90] and KGdW [91] have been used to fabricate such WG structures. The unpredictable nature of the core's location in such structures has made the so-called dual line Type II WGs more widely employed. Such a structure has its core region between the two lower refractive index damage tracks. Additionally, by optimizing the track separation, the stress induced by the two tracks could be made to overlap and create a smooth, higher refractive index core region capable of confining and guiding light [78]. In the literature, a wide number of crystals and ceramics were used to realize such WG structures for applications in lasers and nonlinear frequency conversion. However, in some cases, these WGs may manifest a polarization

favouring nature which might not be necessarily needed in naturally anisotropic laser gain media and phase matched frequency conversion [78, 92].

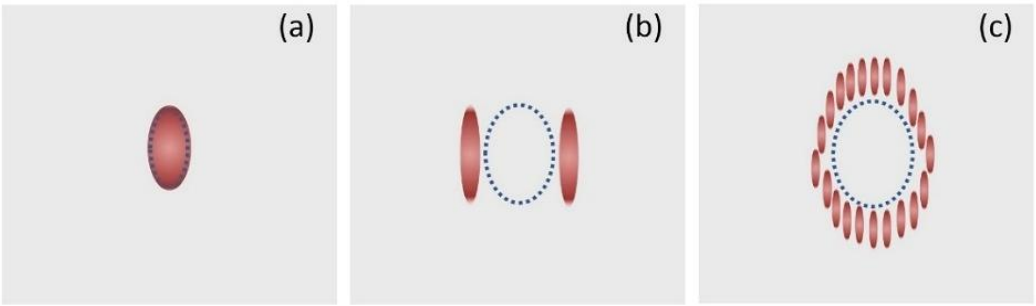

Figure 2.14. Schematic of the fs-DLW WGs: (a) Type I; (b) Type II and (c) Type III structures. The dotted circles represent the core regions.

A core region encircled by quasi-continuous lower refractive index damage tracks is classified as Type III (Depressed-index cladding) WG [82]. This design is analogous to optical fibers where the refractive index contrast between the core and the surrounding cladding is used to confine the light field. In depressed-index cladding WGs, the core region maintains the inherent crystalline and spectroscopic properties making them appealing for lasing applications. Such WG lasers were demonstrated in Nd^{3+} doped YAG [93] and gadolinium gallium garnet (GGG) [94], Yb^{3+}:YAG [95], Er^{3+}:$LiLuF_4$ [96], Pr^{3+}:YLF [97] and Tm^{3+} doped ZBLAN [98]. By tailoring the cladding structures and laser writing conditions, WGs with different cross-sectional geometry and supporting both TE and TM polarizations could be achieved [99]. In this thesis work, buried and surface depressed-index cladding WGs with circular and rectangular core geometries were fabricated in the low-symmetry monoclinic Ln^{3+}-doped KREW crystals.

2.4 Laser parameters in quasi-3-level laser systems

As the Ln^{3+}-doped KREW materials implemented in this thesis belong to the quasi-3-level laser systems, the main laser parameters (threshold pump power and slope efficiency) deduced from the rate equations are discussed in this section. The notations and derivations implemented in [24, 100, 101] were adopted here to enable a complete understanding of the basic concepts needed to describe the laser parameters and the achieved results.

For the Ln^{3+} ions described in the previous sections, considering efficient NR and CR processes, the electronic population in the rest of manifolds, except those manifolds containing the stark levels serving as the upper and lower laser levels, could be considered negligible. For instance, in Tm^{3+} ions $N_{H_6^3} + N_{F_4^3} \approx N_{Tm^{3+}}$ where, $N_{Tm^{3+}}$ is the total Tm^{3+} ion doping concentration.

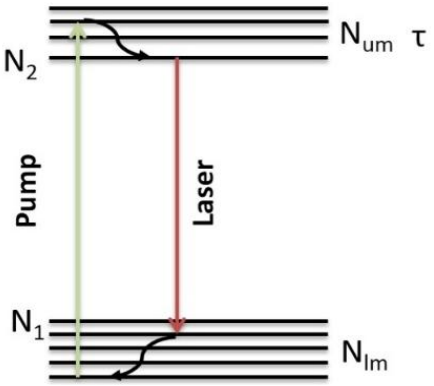

Figure 2.15. Schematic of the upper and lower manifolds: $N_1$and N_2 are the populations of the lower and upper laser levels, N_{lm} and N_{um} are the total population of the lower and upper manifolds, τ is the lifetime of the upper laser level.

At thermal equilibrium, the electronic population in the different stark levels of the manifolds shows a Boltzmann distribution. The electronic population in the lower (N_1) and upper (N_2) laser levels (see Fig.2.15) could be calculated from their respective fractional population as: $N_1 = f_1 N_{lm}$ and $N_2 = f_2 N_{um}$ where f_1 and f_2 are fractional population of the lower and upper laser levels, N_{lm} and N_{um} are the total population in the lower and upper manifolds.

The electronic population of the upper and lower laser levels are governed by the different transitions (i.e. pump, stimulated and spontaneous transitions) constituting the rate equations. If the depletion of the ground (pump) energy state is not significant and single-pass pump absorption is assumed with no spatial hole burning effect, the rate equations would be given as,

$$\frac{dN_2}{dt} = \frac{f_2 \eta_a \eta_q P_P r_p(x,y,z)}{h\nu_p} - \frac{f_2 \sigma c \Phi (N_2 - N_1)\phi_L(x,y,z)}{n} - \frac{(N_2 - N_2^0)}{\tau} \tag{2.16}$$

$$\frac{dN_1}{dt} = \frac{f_1 \sigma c \Phi (N_2 - N_1)\phi_L(x,y,z)}{n} - \frac{f_1 \eta_a \eta_q P_P r_p(x,y,z)}{h\nu_p} - \frac{(N_1 - N_1^0)}{\tau} \tag{2.17}$$

Where, $\Phi = \frac{2nl}{c}\frac{P_L}{h\nu_L}$ is the total cavity photon density, n and l are the refractive index and length of the gain medium, c is the velocity of light, h is the Planck's constant, $P_L(P_P)$ and $\nu_L(\nu_P)$ are the laser (pump) power and frequency, respectively, τ is the lifetime of the upper laser level, σ is the emission cross-section of the laser transition and η_q is the pump quantum efficiency. In those rate equations, the absorption and emission cross-sections of the stark levels involved in the laser transitions (upper & lower laser levels) are considered. They are related as $\sigma_e = \sigma_a g_1/g_2$ where $g_1$and g_2 are the degeneracy of the levels. Hence, $\sigma_e = \sigma_a = \sigma$ is considered for the upper and lower laser levels with the same degeneracy, $g_1 = g_2$ [100]. The pump absorption efficiency is given by $\eta_a = 1 - e^{-\alpha_p l}$, where α_p is the pump absorption coefficient. The initial (unpumped) population of the lower and upper laser levels are N_1^0 and N_2^0, respectively. The spatial distribution of the pump $r_p(x,y,z)$ and laser $\phi_L(x,y,z)$ modes are assumed to be Gaussian without significant diffraction within the gain medium. The rate of the population inversion density $\Delta N = N_2 - N_1$ can be expressed from equations 2.16 and 2.17 as,

$$\frac{d\,\Delta N}{dt} = \frac{f \eta_a \eta_q P_P r_p(x,y,z)}{h\nu_p} - \frac{f \sigma c \Phi \Delta N \phi_L(x,y,z)}{n} - \frac{(\Delta N - \Delta N^0)}{\tau} \tag{2.18}$$

Where, $f = f_1 + f_2$ and $\Delta N^0 = N_2^0 - N_1^0$ is the initial population inversion density. Subsequently, the rate of the cavity photon density expressed in terms of the population inversion density will be given by,

$$\frac{d\Phi}{dt} = \frac{\sigma c \Phi}{n} \iiint \Delta N \phi_L(x,y,z)dx\,dy\,dz - \frac{c\Phi\delta'}{2nl} \tag{2.19}$$

The total round-trip cavity losses δ' consist of the intrinsic cavity loss L_{in} (related to the WG propagation loss as, $\delta_{WG} = L_{in}/2l$) and the output coupling loss $\gamma_{OC} = -ln(1 - T_{OC})$. For the lasing to proceed, the round-trip gain averaged over the cavity modes G should compensate the total round-trip losses. Under the steady-state pumping condition, the population inversion density and cavity photon density will be constant, ($\frac{d\,\Delta N}{dt} = 0$ and $\frac{d\Phi}{dt} = 0$), implying the following relations,

$$G = \delta' = 2\sigma l \iiint \Delta N \phi_L(x,y,z)dx\,dy\,dz \tag{2.20}$$

$$\Delta N = \frac{\frac{f\tau\eta_a\eta_q P_P r_p(x,y,z)}{h\nu_p} - N_1^0}{1 + \frac{2l\, P_{out} f\sigma\tau\phi_L(x,y,z)}{h\nu_L T_{oc}}} \tag{2.21}$$

Where, $P_{out} = T_{OC}P_L$ is the laser output power emitted at the OC mirror. In the expressions, N_2^0 is ignored as it is significantly lower than N_1^0, for the unpumped gain medium. Equation 2.21 represents the population inversion density under steady-state conditions. For a Gaussian pump and laser spatial mode distributions with $w_x(\frac{1}{e^2})$ and $w_y(\frac{1}{e^2})$ beam radii along x and y (transversal) axes, by inserting equation 2.21 into equation 2.20, the expressions for the threshold absorbed pump powers in bulk (P_{th_b}) and WG (P_{th_Wg}) lasers are derived [24, 101].

$$P_{th\_Wg} = \frac{h\nu_p}{f\sigma_e\tau\eta_a\eta_q}\frac{\pi}{4}(w_{Px}^2 + w_{Lx}^2)^{\frac{1}{2}}\left(w_{Py}^2 + w_{Ly}^2\right)^{\frac{1}{2}}(L_{in\_wg} + L_{OC} + 2N_1^0\sigma_a l) \tag{2.22}$$

$$P_{th\_b} = \frac{h\nu_p}{f\sigma_e\tau\eta_a\eta_q}\frac{\pi}{4}\left(\overline{w_{Px}}^2 + \overline{w_{Lx}}^2\right)^{\frac{1}{2}}\left(\overline{w_{Py}}^2 + \overline{w_{Ly}}^2\right)^{\frac{1}{2}}(L_{in\_b} + L_{OC} + 2N_1^0\sigma_a l) \tag{2.23}$$

$$\overline{w_{P(L)}} = \sqrt{\frac{\lambda_{P(L)} l}{\sqrt{3}\pi n}} \tag{2.24}$$

As a focused pump beam is incident on the gain media, the spot size of the beam changes (along the medium) due to diffraction. However, in WG laser this is not a problem, due to the tight confinement inside the high refractive index core. For bulk laser, the Rayleigh length of the focused pump beam should be closer to the length of the gain medium, so that significant diffraction does not occur during its propagation. The same holds for the laser beam. Consequently, in the case of the bulk lasers, the pump and laser spot sizes averaged over the gain medium $\overline{w_{P(L)}}$ are to be used in equation 2.23 [24]. The re-absorption loss arising from the thermally populated lower laser level, $2N_1^0\sigma_a l$, is considered as a cavity-loss that is needed to be surpassed before the laser reaches its threshold.

Gain materials exhibiting a longer upper laser level lifetime τ and larger emission cross-sections σ_e at the laser wavelength are potentially suited for lasers with lower laser threshold. For instance, among the common hosts for Tm^{3+} ions, YAG (τ=10.5 ms, σ_e =0.15 x10^{-20} cm^2) [35], YLF (τ=15.6 ms, σ_e =0.4 x10^{-20} cm^2) [102], Lu_2O_3 (τ=3.8 ms, σ_e =0.28 x10^{-20} cm^2) [103], $GdVO_4$ (τ ~ 1.9 ms, σ_e =0.25 x10^{-20} cm^2) [103], the monoclinic KLuW has relatively lower τ ~ 1.3 ms but much larger σ_e = 3.74 x 10^{-20} cm^2 (for E || N_m). As these parameters are spectroscopic properties of the gain media, they would influence the laser threshold of both bulk and WG lasers in a similar fashion. It should be mentioned that, the upper laser level lifetime τ also determines the energy storage capacity of the gain media. This is crucial in *Q*-switched lasers.

WG lasers show an advantage in confining the pump and laser beams in small cross-sectional areas favouring lower threshold powers, as compared to bulk lasers. This advantage is even more pronounced in channel WGs than in their planar counterparts, as the confinement is along both transversal directions. In bulk lasers, the transversal laser mode sizes are determined by effects such as thermal guiding and gain guiding [104, 105]. In those cases, for longitudinally pumped bulk materials with radially symmetric temperature distribution, if the material has a positive thermo-optic coefficient, the slightly higher refractive index at the pumped region will act as a thermal WG defining the transversal laser mode sizes. If the absorption length of the pump beam is shorter than the length of the gain medium, the thermally induced refractive index change will be considered as a lens (thermal lensing) in the cavity, influencing the transversal laser mode sizes. Gain guiding is also similar, the pumped region of the bulk laser material defines the transversal laser mode sizes. These effects make it possible to operate compact plane – plane microchip bulk lasers, whose typical mode sizes ($2w(\frac{1}{e^2})$ ~ 200 µm [106]) are larger than

those in WG lasers. One important distinction between the bulk and the channel WG laser fabricated in a similar gain material is, in the latter case, the tight confinement of the beams would allow the laser to operate without an OC mirror (i.e., solely relying on the Fresnel reflection at the interface). Such operation regime may not be possible in bulk lasers, due to the very high cavity losses involved. Furthermore, the intrinsic cavity losses introduced by the various cavity components could be different for bulk and WG lasers. Especially the propagation losses in WG lasers, arising from the different fabrication and structuring procedures, should be minimized not to lose the advantages acquired by the tightly confined nature of the modes.

The slope efficiency η_s of a laser describes the conversion efficiency of the incident or absorbed pump power P_{abs} towards the useful laser output P_{out}. The maximum slope efficiency that could be achieved is determined based on various parameters in the laser system [43].

$$\eta_s = \frac{dP_{out}}{dP_{abs}} = \eta_m \eta_{st} \eta_q \eta_{out} \tag{2.25}$$

Here, $\eta_{out} = ln(1 - T_{OC}) / ln[(1 - T_{OC})\,(1 - L_{in})]$ is the cavity output coupling efficiency, describing the fraction of the laser photons emitted through the OC mirror. In the expression, the logarithmic intrinsic cavity loss is considered, - $ln(1 - L_{in})$. The high T_{OC} typically used in WG lasers could result in a high slope efficiency, at the expense of an increased threshold. The mode-overlap efficiency η_m describes the overlap between the laser and pump beams. As both beams are tightly confined inside the core region, a WG laser could have η_m~ 100%. This is crucial as all the excited ions would be accessed by the oscillating laser radiation inside the cavity, leading to a high slope efficiency. The pump quantum efficiency η_q describes the number of upper laser level excitations per one pump photon. For instance, in gain materials favouring a relatively high Tm^{3+} doping levels (like in KREWs) the quantum efficiency could reach η_q ~ 200%, due to the efficient CR processes among the neighbouring ions.

2.5 Pulsed laser generation - passive *Q*-switching

In addition to the CW operation regime, where the intensity of the output laser is constant as a function of time, periodic emission of "short bursts" of light intensity, is possible in pulsed wave operation regime. The duration of the pulses depends on the technique implemented, μs – ns pulses are achieved using *Q*-switching, while much shorter pulses (~ few fs) are feasible by implementing mode-locking techniques. In the context of this thesis work, the *Q*-switching technique was implemented for short pulse generation, therefore some of the basic concepts are discussed in this section.

As the name suggests, *Q*-switching involves changing the quality factor (*Q*-factor) of the laser cavity. This could be accomplished by introducing some losses (extra absorption) into the laser cavity, preventing laser oscillation. If the losses are modulated with an electrical drive signal, using electro-optic or acousto-optic modulators, it is called active *Q*-switching [107, 108]. In passive *Q*-switching (PQS), the losses are modulated using a non-linear optical element (saturable absorber, SA) inserted in the laser cavity. The SA has a linear absorption matching the laser wavelength which, under high laser intensity (fluence), can be bleached providing a much faster loss modulation mechanism than electronically controlled modulators.

Initially, the SA in the cavity prevents lasing and the population inversion of the gain material increases far above its threshold value (i.e. high loss, low *Q*-factor cavity). As the pumping proceeds, the amount of amplified spontaneous emission (ASE) grows rapidly, reducing the absorption (loss) induced by the SA. The laser radiation starts to oscillate building its intra-cavity intensity, which further bleaches the SA (i.e. low loss, high *Q*-factor cavity). As the gain in the laser cavity is well above the level of the losses, a short and intense laser pulse is emitted at the output. In the meantime, the SA recovers and the gain in the cavity is depleted, the *Q*-factor is again lower, paving the way for the formation of the next laser pulse [109].

In the laser cavity, the SA could be implemented in transmission (deposited onto a transparent substrate) or reflection configuration (with mirrors serving as a substrate for the SA layer). In this thesis work, all the implemented SAs operate in transmission mode. Generally, few parameters are used to characterize the SAs. The non-saturable loss α'_{NS} is the unwanted loss that arise from some defects and limitations during the fabrication of the SA. For instance, scattering at the interface between the substrate and the deposited SA layer would contribute to such loss and needs to be minimized. It limits the conversion efficiency of the PQS laser with respect to CW mode of operation. Under high laser intensity (fluence), the saturable loss α'_S could be reduced leading to the bleaching of the SA. Hence, this loss controls the modulation depth (MD) of the SA. The saturation intensity I_{sat} (fluence F_{sat}) determines the laser intensity (fluence) needed to reduce the saturable part of the absorption by ½ ($1/e$) from its small – signal value, Fig 2.16. After an interaction with a short laser pulse, the relaxation of the SA towards an equilibrium state determines its recovery time τ_{rec}. If the duration of the laser pulse is longer than the recovery time of the SA, the absorber is considered as a "fast" SA, which is promising for generation of nanosecond PQS pulses at high repetition rates. The opposite situation corresponds to the so-called "slow" SA for which the pulses are shorter than the recovery time of the SA. Usually, such a SA provides high pulse energy at low pulse repetition rates.

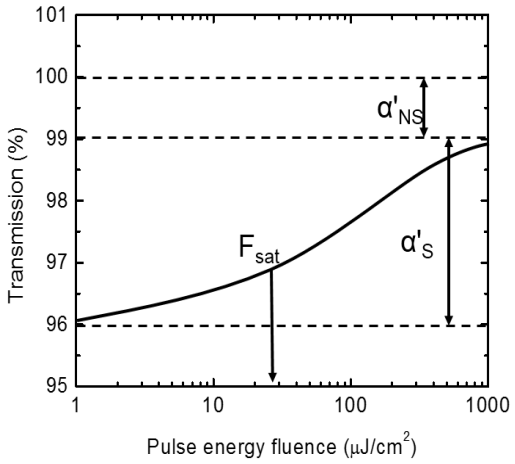

Figure 2.16. Representative characteristic curve of the nonlinear transmission of a SA as a function of the incident pulse fluence. F_{sat} is the saturation fluence, α'_S and α'_{NS} are the saturable and non-saturable losses.

The F_{sat} and α_S' of a SA could be experimentally determined through an absorption saturation measurement. The open – aperture Z – scan method is usually implemented for this purpose [110]. In this method, the SA is translated along the focus of a pulsed laser while monitoring its transmission T (absorption α), as a function of the incident laser fluence, $T(F) = 1 - \alpha(F)$. In small – signal regime, $T_0 = 1 - \alpha'_0$ where the small – signal absorption $\alpha'_0 = \alpha'_S + \alpha'_{NS}$. The measured curve will be fitted using an appropriate model function using F_{sat} and α'_S as free fitting parameters. Once the α'_S value is known, the corresponding α'_{NS} could be deduced from the small – signal absorption value of the SA. The recovery time could be measured using the pump-probe spectroscopic technique. Basically, a pump beam is used to excite the SA into a non-equilibrium state, followed by interrogation with a probe beam for monitoring the dynamic transmission response of the SA, as a function of the time delay between the beams. If the response is fitted with a bi-exponential function, different relaxation mechanisms may be involved in the SA [111].

The numerical modeling of the PQS laser operation has been reported in the literature, see for example [109, 112]. Such models were implemented to study the influence of different parameters on the output characteristics of the lasers. In [109], a model describing the PQS of a microchip laser using a semiconductor saturable absorber mirror (SESAM) operating in the "slow" SA regime ($\tau_{rec} > \tau_p$, where τ_p is the pulse width) was reported. A set of rate equations describing the intracavity photon density, upper laser level population density (of the gain material) and the excited state population density (of the SA) were solved. Assumptions such as, much lower saturation fluence for the SA F_{sat} than the laser medium F_{lm} ($F_{sat} << F_{lm}$), no spatial hole burning and beam divergence inside the cavity were considered in the model. From the numerical simulations, the time-dependent intracavity

power, gain and losses were determined, describing the evolution of the pulse build-up processes and its emission from the cavity. For more details, the reader is advised to refer to [109], but here, the final analytical expressions describing some of the important PQS output characteristics and their relation with the cavity and SA parameters are discussed. Although the model was developed as a design guideline for microchip lasers, it could still be used to understand PQS WG lasers operating in similar operation regime.

The pulse width is described as $\tau_p \sim 3.52\, T_R/(MD)$ where, $T_R = 2nl/c$ is the roundtrip cavity time. For the generation of shorter pulses, compact cavities (as in microchip and WG lasers) and SA with larger MD are suited. In the "slow" SA operation regime, the pulse width is not strongly dependent on the absorbed pump power. The pulse energy is expressed as $E_P \sim F_{lm} A_L (MD) \eta_{out}$ where, A_L is the laser mode area. SAs with large MD are needed for generation of high pulse energies. Using high T_{OC} the pulse energy would also increase, given the proper intracavity intensity for saturating the SA is available. A small laser mode area (on the SA), would result in a lower pulse energy, which in WG lasers is typically in nJ levels.

In [112] the modeling of Tm^{3+}-doped microchip lasers using graphene SA was discussed. As the characteristic pulse width from Tm^{3+}-doped microchip lasers were much larger than the recovery time, the absorber was treated as a "fast" SA. The model is basically similar to the one described above. It involves solving the rate equations for the quasi-3-level system, that included the intensity dependent absorption of the SA. Subsequently, the time dependent intracavity intensity was used to deduce the corresponding intracavity power, from which the pulse characteristics (τ_p, E_P and pulse repetition frequency) were estimated. For an increase in the absorbed pump power, the pulse widths were getting shorter while the pulse energies increased. At very high pump powers, the SA was completely bleached and the pulse characteristics were not changing much. The pump power dependent pulse characteristics, were related to the variable bleaching of the SA which is typical for "fast" SAs [112]. "Fast" SAs such as SWCNTs, graphene or MoS_2 are saturated by the laser intensity (unlike "slow" SA which are saturated by the energy fluence). With an increase of the pump power, the intracavity intensity on the SA I_{in} (i.e., $I_{in} = X \cdot (2E_p/(\pi w_L^2 \Delta\tau^*))$, where $X = (2 - T_{OC})/T_{OC}$ is the output-coupling factor and $\Delta\tau^* \approx 1.06\tau_p$ is the effective pulse duration, assuming both Gaussian laser mode and temporal pulse profile) increases, leading to larger MD - asymptotically approaching the α_S' value of the SA. This, in turn, leads to an increase of the pulse energy and shortening of the pulse duration. A similar modeling was implemented, in this thesis work, in order to explain the pulse characteristics of the PQS WG lasers.

Recently, in addition to PbS-quantum-dot-doped glass [113], SESAMs [114], transition-metal doped chalcogenide crystals (Cr^{2+}:ZnSe or ZnS) [115], multiple studies were dedicated to novel nanostructured SAs featuring a broadband linear and saturable absorption due to the special band structure. The most prominent examples are carbon nanostructures, such as graphene [111, 112], representing a 2D layer of carbon atoms arranged in a honeycomb lattice, and single-walled carbon nanotubes (SWCNTs), representing rolled sheets of graphene. Other materials, such as few-layer transition metal dichalcogenides [110](e.g., MoS_2, $MoSe_2$, or WS_2), topological insulators, and related nanomaterials (e.g., Bi_2Te_3, Bi_2Se_3, or Sb_2Te_3) [116], black phosphorus [117] and graphene oxide [118] were also studied. As for the carbon nanostructure based (graphene and SWCNTs) SAs implemented in this thesis work, the basics of the band structure, absorption, and relaxation mechanisms are addressed in the following sections.

2.5.1 Single-walled carbon nanotubes saturable absorber

Single-walled carbon nanotubes (SWCNTs) have increasingly become promising for developing novel SA materials in ultrafast laser generation [119]. They are currently being pursued as a good alternative to other SAs such as SESAMs, especially in the ~ 2 μm spectral range [120]. The simple and cost-effective fabrication processes (such as spin coating and spray methods) make them more favourable for mass production [119]. For SWCNTs structures, the diameter and chirality of the tubes determine their metallic or semiconductor nature. The absorption resonances of the electronic inter-band transitions are also dependent on the tube diameter and chirality, resulting in a broadband absorption in layers containing mixtures of randomly oriented individual SWCNTs [121].

The first and second van Hove optical transitions (of a single nanotube structure density of states), indicating the excitation and emission processes, is given in Fig. 2.17. The transmission spectra of SWCNTs SA contains two broad absorption bands, spanning from ~ 0.8 – 1.2 μm and ~ 1.6 – 2.2 μm. The first absorption band is due to the second van Hove optical transition E_{22} while the second absorption band is from the fundamental transition (E_{11}) of the semiconducting carbon nanotubes [111]. It should be noted that the synthesis methods implemented for fabricating the SWCNTs determines the spectral location of these absorption bands [121]. For a given SA layer thickness, it is possible to vary the absorption (i.e. MD of the SA) by increasing the concentration of the SWCNTs.

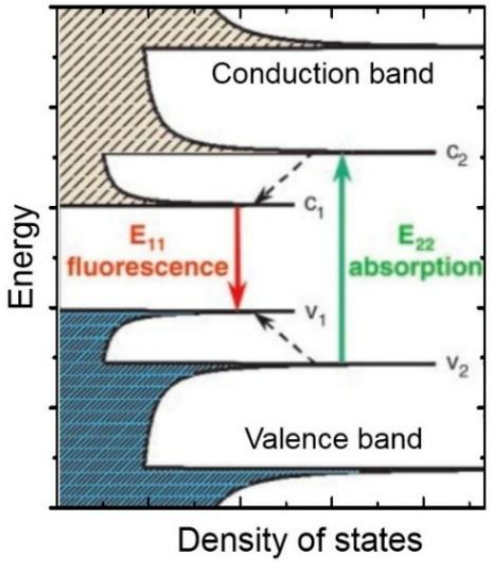

Figure 2.17. Schematic of the density of electronic states for a single carbon nanotube structure. The solid lines represent the optical transitions and dashed lines represent the non-radiative relaxations of the carriers (from [122]).

Under high-intensity excitation, the charge carriers will get promoted from the valence to the conduction bands. However, once all the excited states are occupied, the SWCNTs SA will be bleached with its absorption dropping towards the non-saturable value. For SWCNTs SA (as the one used in this thesis work), the dynamic transmission response (relaxation processes) was studied by the pump-probe technique at 1.92 μm, revealing two characteristic recovery times. The “fast” component (0.25 ps) due to the intra-band carrier relaxation and the “slow” component (1.16 ps) arising from inter-band carrier re-combinations [111]. Considering the nanosecond pulse widths, typical from the PQS WG lasers, the SWCNTs SA was treated as a “fast” SA.

2.5.2 Graphene saturable absorber

Graphene is the most prominent example of 2D materials. It consists of a single layer of carbon atoms arranged in a honeycomb lattice. Graphene features hollow-cone valence and conduction bands meeting each other at the Dirac point, Fig.2.18. Such a zero-bandgap electronic structure leads to the wavelength-independent small signal absorption of graphene ($\pi\alpha \approx 2.3\%$, $\alpha = e^2/4\pi\varepsilon_0\hbar c \approx 1/137$ is the fine structure constant) [123].

For samples containing multilayer (n) graphene, the small signal absorption scales almost linearly ~ $n\pi\alpha$. Moreover, graphene exhibits broadband (0.8 – 3 μm) saturable absorption due to the finite number of electron and hole states, according to the Pauli blocking principle [123, 124]. When a photon with energy $h\nu$ is absorbed, an electron gets excited from the valence to the conduction bands, resulting photogenerated carriers in the respective bands. under high-intensity excitations, the $h\nu/2$ energy intervals of both bands get filled blocking further absorption and bleaching the graphene SA [123], Fig.2.18.

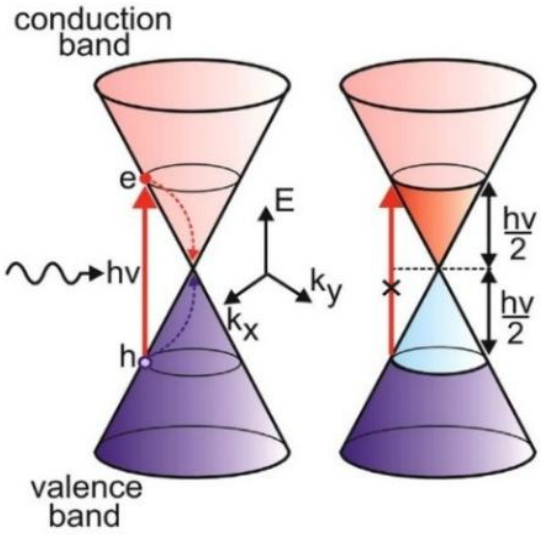

Figure 2.18. Schematic of the band structure and the absorption saturation process in graphene (from [112]).

The small signal absorption is almost independent of the photon energy $h\nu$. Nonetheless, the saturation intensity I_{sat} increases with $h\nu$ owing to the band structure [125]. It is easier to achieve saturation of the graphene at longer wavelengths. Thus, the application of graphene for lasers emitting at ~2 μm is of particular interest [112]. As a SA, graphene offers relatively low I_{sat}, ultrafast recovery time, and sufficiently high laser-induced damage threshold. The graphene SAs employed in this work were of transmission-type. The ultrafast relaxation processes in graphene SA were investigated by the pump-probe technique at 1.56 μm [126]. It revealed two characteristic decay times, from the bi-exponential fitting model. The "fast" component of ~ 0.18 ps due to the intra-band carrier scattering and a "slow" component of ~ 1.3 ps due to the electron-hole recombination as well as the electron-phonon interaction [126]. Hence, the implemented graphene SA is expected to have similar relaxation dynamics, as such, it was treated as a "fast" SA in the PQS WG laser operations.

Chapter 3 Experimental techniques

The experimental techniques used for fabricating and characterizing the waveguide lasers are discussed in this chapter. The Top-Seeded Solution Growth slow-cooling method implemented for growing the substrates as well as the Liquid phase epitaxial growth method implemented for fabricating the active layers are described. Micro-structuring of the samples using diamond saw dicing and femtosecond direct laser writing methods are presented. Furthermore, spectroscopic and microscopic characterizations of the fabricated waveguides are addressed. Finally, the techniques and experimental setup used for waveguide characterization and laser experiment are described.

3.1 Crystal growth and sample preparation

3.1.1 Top-Seeded Solution Growth slow-cooling method

The Top-Seeded Solution Growth (TSSG) slow-cooling method, is one of the so-called high-temperature solution (HTS) growth methods used for fabricating single crystalline materials [127]. This method is suited for fabricating materials that normally undergo a phase transition below their melting point. The polymorphic nature of the KREW crystals along with the corresponding phase transition have been studied in [37, 38, 50]. It was shown that such crystals undergo a phase transition, from β-phase (tetragonal) to α-phase (monoclinic crystal system), below their melting point. Therefore, growing such crystals from their melt may lead to the formation of the undesired crystal phase, critical strains, and fractures. Consequently, a solution-based growth method (such as TSSG) is more suitable.

The TSSG growth method was extensively studied and optimized in the FiCMA-FiCNA group [48, 50, 128, 129]. In the course of this thesis work, a vertical tubular furnace with kanthal heating element was employed for growing the crystals using the TSSG method. The photograph of such a furnace is shown in Fig.3.1. The furnace was thermally isolated from the environment (using fire-bricks and metallic cover sheets) in order to maintain the desired growth temperature. Inside the furnace, an S-type thermocouple connected to a programmable temperature controller (EUROTHERM 2604) was used for controlling the temperature with a precision of 0.01 K. The furnace also has a mechanical pull-handle for vertically translating the alumina-rod on which the seed-crystal was attached, Fig.3.1. The vertical translation of the rod (seed) was monitored using a Mitutoyo micrometer with a precision of 10 µm. A motor whose rotational speed is controlled using a DC power supply was used to rotate the rod (seed) with the desired revolution-per-minute (rpm).

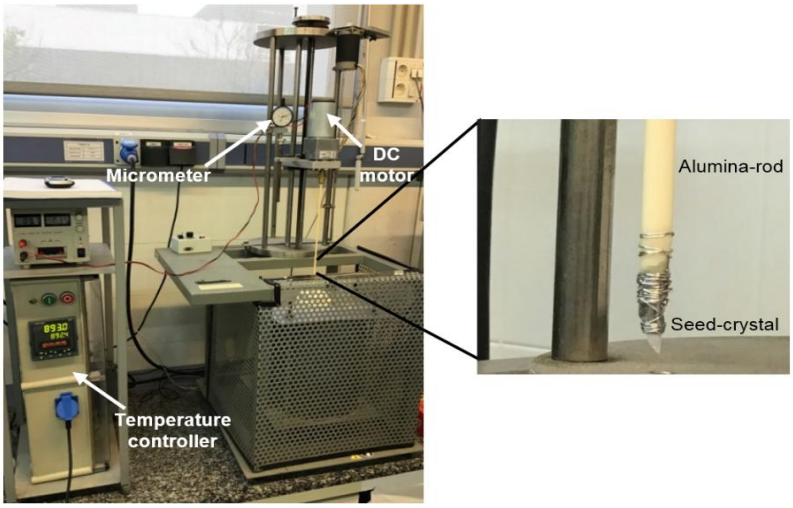

Figure 3.1 The vertical tubular furnace used for the growth of the crystalline KREW samples and the seed-crystal tied onto the alumina-rod with platinum wires.

During each crystal growth, the corresponding precursor oxides (K_2CO_3, Y_2O_3, Lu_2O_3, Gd_2O_3, Tm_2O_3, Er_2O_3, Ho_2O_3) were chosen and dissolved in a platinum crucible. The solution was later placed inside the furnace, making sure that the appropriate thermal gradient is maintained (~ 0.1 K/cm). This is to avoid unwanted nucleation and mini-crystal formation at the bottom of the solution in the crucible. Potassium ditungustate ($K_2W_2O_7$) was used as a solvent. This solvent is proven to be favourable for growing KREW crystals, as it contains no foreign ions and has a low melting point [49, 127]. The optimization of the solute/solvent molar ratio, for achieving good quality KREW crystals, has been addressed in [48, 50, 130]. For instance, from the solubility curve of $KLu(WO_4)_2$ in $K_2W_2O_7$ shown in Fig.3.2, it can be seen that, by choosing different molar ratios, the temperature-induced growth-rate of the solute could be varied. However, there should be a compromise between the growth-rate and the crystal quality (absence of defects and inclusions). For all the bulk crystals grown in this work, a solute/solvent ratio of 12 mol% / 88 mol% was chosen.

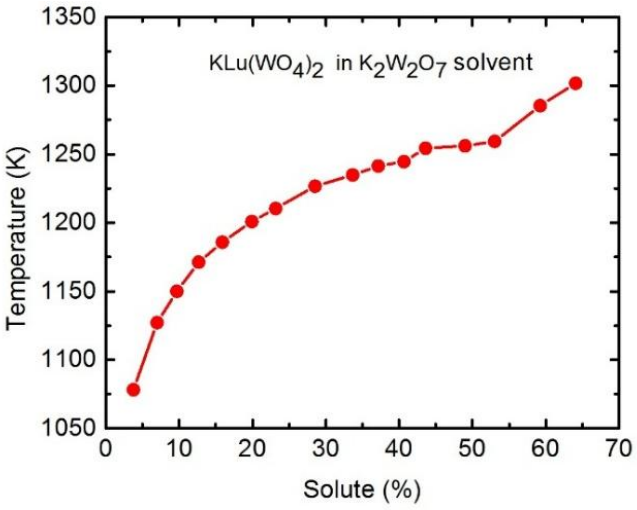

Figure 3.2 The solubility curve of $KLu(WO_4)_2$ in $K_2W_2O_7$ solvent, reproduced from [50]

After preparation, the solution was kept at ~30 – 40 K above the saturation temperature (for at least 6 h), in order to homogenize it. Once the solution was properly homogenized, the saturation temperature (T_S) of the solution was determined using a *b*-oriented seed-crystal tied to the alumina rod (see Fig.3.1). It has been previously reported that the *b*-oriented seed favours bigger crystal size with the absence of inclusions and defects [49]. Rather than directly introducing the seed, it was kept slightly above the furnace, for about 30 minutes, in order to avoid a thermal shock. Once it is inserted, the seed has to be vertically translated, until it reaches the surface of the solution, with a step of 1 cm / 5 min. The revolution speed of the seed was set to ~ 40 rpm. This helps to enhance the homogenization and improve the mass and heat transfer, resulting in an inclusion-free crystal growth [129].

During the seeding procedure (for determining the T_S), the growth or dissolution of the seed that is in contact with the surface of the solution is monitored every 5 – 15 min. If it is dissolving/growing, the current temperature of the furnace (solution) has to be reduced/increased, respectively. Such iterative procedure was performed, until the temperature at which neither dissolution nor growth is reached. This temperature is taken as the T_S of the solution. For every growth run or a new solution prepared, the T_S has to be accurately measured implementing a similar procedure.

After the determination of the T_S, the seed that is already touching the surface of the solution is slowly pulled up to a height where its contact with the meniscus is about to break (~ 200 µm before losing the contact). This will determine the portion of the seed that is inside the growing crystal, and if not optimized, it might lead to defects and cracks near the vicinity of the seed. The growth process is initiated by suddenly decreasing the temperature of the solution by ~30 – 35 K (from T_S) with a rate of ~0.12 – 0.15 K/h. This will induce the supersaturation of the solution, resulting in a layer-by-layer growth of the solute around the seed [49, 131]. Once the growth process was finalized, the grown crystal is slowly extracted (1 mm / 5 min) until it reaches a height of about 1 mm above the surface of the solution. This is to avoid any thermal shock and cracking during extraction. Similarly, the

temperature of the furnace is cooled down to room temperature, with a rate of ~ 15 – 20 K/h. An even slower cooling rate could be implemented at the expense of increasing the overall fabrication time.

3.1.2 Liquid phase epitaxial growth

Liquid phase epitaxial (LPE) growth is a method by which, a high quality single crystalline layer is grown on a substrate with the desired crystal orientation [131, 132]. Using this method, active planar WG with different film thickness and doping levels could be grown. In such waveguiding application, the desired confinement and propagation of the light field would require a refractive index contrast between the grown layer and the substrate. The lattice mismatch should also be as minimum as possible. This is to avoid material stress and defects at the interface. Such stress and defects are the sources of scattering loss in LPE grown WG, affecting its performance. The lattice mismatch might also lead to the cracking of the layer during the LPE growth process.

In this thesis work, Tm^{3+} - doped $KY(WO_4)_2$ layers were grown on an undoped $KY(WO_4)_2$ substrates using the LPE method. The growth and characterization of such lattice matched Ln^{3+}:KREW layer on a KREW substrate have already been reported [71, 133-135]. The Ln^{3+}dopant ions (i.e. Tm^{3+}, Lu^{3+}, Gd^{3+}) in the LPE grown layer, replace the corresponding RE^{3+}cation in the KREW matrix (e.g., Y^{3+} in KYW). The Ln^{3+}- doped LPE layer has a higher refractive index than the undoped substrate (which has the same stoichiometry).

The LPE growth procedure is similar to the one described for the TSSG method. A solution is prepared using the precursor oxides needed for having the intended active dopant and layer matrix. $K_2W_2O_7$ was still used as a solvent. The solute/solvent molar ratio is chosen as 7 mol% / 93 mol %, as this ensures a slower growth rate) and better final layer quality [129]. Additionally, the temperature gradient of the solution should be kept minimum (close to zero). This ensures a more uniform growth over the surface of the substrate. After homogenizing the solution, its saturation temperature is determined following the same procedure as described in the TSSG method.

For the LPE layers grown in this work, a (010) oriented undoped $KY(WO_4)_2$ substrate was prepared from a bulk crystal that was previously grown by the TSSG method. The relatively slower growth rate along the (010) crystal face favours a layer-by-layer solute deposition, resulting in a high-quality, defect-free LPE layer [136]. A brief description regarding the preparation of the substrate will be given in the next section. However, before the actual growth process, proper cleaning of the substrate has to be performed. This is intended to avoid any contamination that might be introduced into the solution while dipping the substrate. For this purpose, first, the substrate was dipped and rotated in a mixture of Nitric acid/distilled water (1:3 volume ratio) for 10 minutes, followed by 5 min rinsing in a distilled water. Later, it was cleaned with acetone (5 min) and finally rinsed with ethanol (5 min).

The substrate, which was tied onto an alumina-rod (with a platinum wire) was kept directly over the entrance of the furnace for about 30 min. This was to avoid a thermal shock that might lead to cracking. Afterward, it was lowered down to the surface of the solution, at a rate of 1cm / 10 min. Once the substrate reached a height of about 1 mm above the surface of the solution, it was kept there for about 60 min, again for avoiding a thermal shock. The rotation of the alumina-rod (substrate) was set to 10 rpm. Prior to dipping the substrate into the solution, the temperature of the furnace (solution) was raised by 1 K, from its T_S value. Once the substrate was dipped, it was kept for 5 min. This was intended for dissolving the superficial surface of the substrate removing any defects or scratches (from the polishing) that might impact the growth quality at the interface. Generally, the length of the substrate to be dipped into the solution is determined based on the size of the substrate as well as the length of the sample needed. However, a small portion of the substrate is left free in order to serve as a reference for measuring the as-grown layer thickness.

To initiate the LPE growth process, the temperature of the solution is suddenly reduced by 3K (from T_S value), inducing the supersaturation of the solution. The growth would progress for about ~ 2.5 – 3 h, depending on the desired final layer thickness. Once finished, the substrate would be slowly extracted until it was about ~1 mm above the surface of the solution. Finally, the temperature of the furnace is cooled down to a room temperature at a rate of 15 K/h. If a sample with an external cladding is needed, the as-grown sample would have to be polished

down to the desired layer thickness and would serve as the substrate for the subsequent growth, following the same procedure.

3.1.3 Samples cutting and polishing

The as-grown samples (from the TSSG and LPE methods) undergo further preparations which mainly involves cutting and polishing. During the cutting procedure, as the sample is optically biaxial, the desired orientation of the axes would be carefully aligned using a goniometer. The undoped bulk $KY(WO_4)_2$ crystal was used to prepare the substrate needed for the LPE growth. To obtain such a substrate, the bulk crystal was sliced (perpendicular to the *b*-crystallographic axis) using a Minitom Struers diamond disk saw, ending up with (010) oriented slabs. As the sliced substrate would have a high surface roughness, a subsequent polishing procedure would be performed. For this, it would be mounted on a circular lapping jig and lapped to a laser grade quality using slurry solutions prepared from alumina powders with 9, 3, 1 and 0.3 µm in diameter, consecutively. A Logitech PM5 machine was employed for the polishing procedure, Fig.3.3.

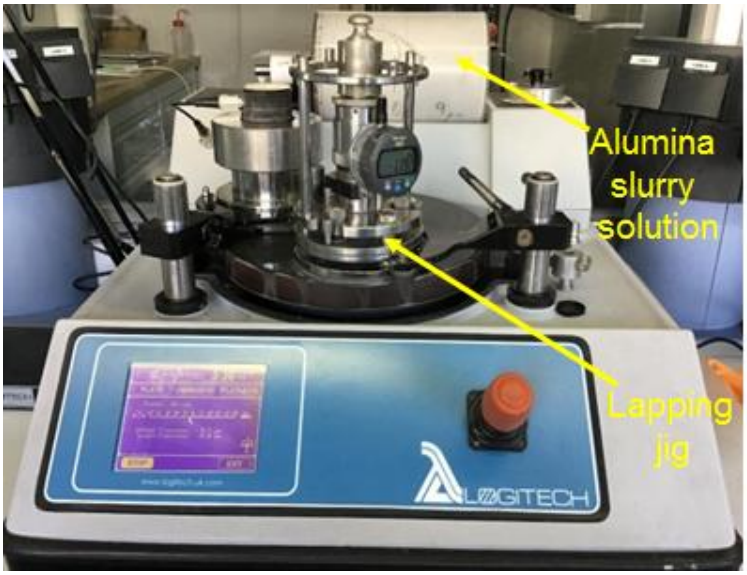

Figure 3.3 The Logytech PM5 polishing machine used for polishing the sample fixed on the jigsaw-disk.

In addition to the substrates needed for the LPE growth, the samples implemented for the inscription of the fs-DLW channel WGs were also prepared using a similar procedure. As the channel WGs are written along the N_g principal optical axis, the prepared samples (after cutting and polishing procedures) were cut perpendicular to this axis. Subsequently, the two end-facets of the samples were carefully polished to a laser grade quality (following the procedures described above). High-quality end-facets are crucial, as they would affect the efficiency of the coupling into the fabricated channel WGs.

After the LPE growth, the as-grown layers were also prepared using a similar procedure (in order to obtain the final waveguiding structure). Once the layers were extracted from the furnace, the quality of the as-grown layers (on either side of the substrate) were assessed. This was done by performing thickness measurement (at different positions) over the surface of the substrates and with a visual inspection of the layers for the presence of any defects. Based on those assessments, the as-grown layers were polished down to the desired thicknesses.

After the polishing was done, the LPE samples were cut perpendicular to N_g principal optical axis and the two end-facets were polished. However, the edge-bending effect that might arise during the polishing of such LPE layers needs to be avoided, as it is detrimental for light coupling into the layers. Therefore, during the polishing procedure, the samples were sandwiched and glued between two flint glasses. Such flint glasses were suited (to be implemented as a supporting mechanism) during end-facet polishing, owing to their hardness (~7 Mohs [137]) which is closer to that of the KREW layers (~ 4.5 – 5.5 Mohs [38]) being polished.

3.2 Micro-structuring of the samples

As it was previously discussed, the LPE grown layers (after cutting and polishing) would directly serve as a planar WGs. However, for confining and guiding the light field along both transversal directions, further structuring of the layers would be needed. In many applications, such 2D confinement may lead to better performance, as long as the extra loss associated with the structuring is kept minimum. So far, different methods have been implemented for the structuring of the KREW materials. Among them, ion-beam etching has been widely used. This method has been implemented for the structuring of both bulk and LPE grown $KY(WO_4)_2$ materials [71, 138]. The standard photolithographic techniques (i.e., mask design, photoresist deposition, UV exposure, and photoresist-development) need to be performed for defining the desired structure. Typically, it has a slower etching rate (limited channel height) and requires longer fabrication time [133]. Similarly, He^+ ions implantation (creating a lower refractive index barrier) was applied to fabricate channel WG in a LPE grown $KY(WO_4)_2$ layer [139]. In this thesis work, the diamond saw dicing and the fs-DLW were applied for the structuring and fabrication of the channel WGs.

3.2.1 Diamond saw dicing

Diamond saw dicing is a technology that is well developed in the semiconductor packaging industry (for wafer sawing) [140]. Recently, this method is gaining an interest in the field of optics for making channel WGs. Basically, it involves ductile-type material removal using a specialized diamond blade attached to spindler with a smooth rotational action [141]. In combination with other fabrication techniques, WGs with advanced functionalities have been already demonstrated using this method [76]. In this thesis work, a Dicing Saw machine (Disco DAD 321), having an air-bearing spindler with the rotational speeds in the range of 3000 – 40000 rpm was used, Fig.3.4. An adhesive-tape with 0.8 mm thickness was used to mount the samples. The translation speed of the "sample-bed" could be set between 0.1 – 300 mm/s. The movement of the blade (in the vertical direction) could be controlled with a precision of 0.1 µm.

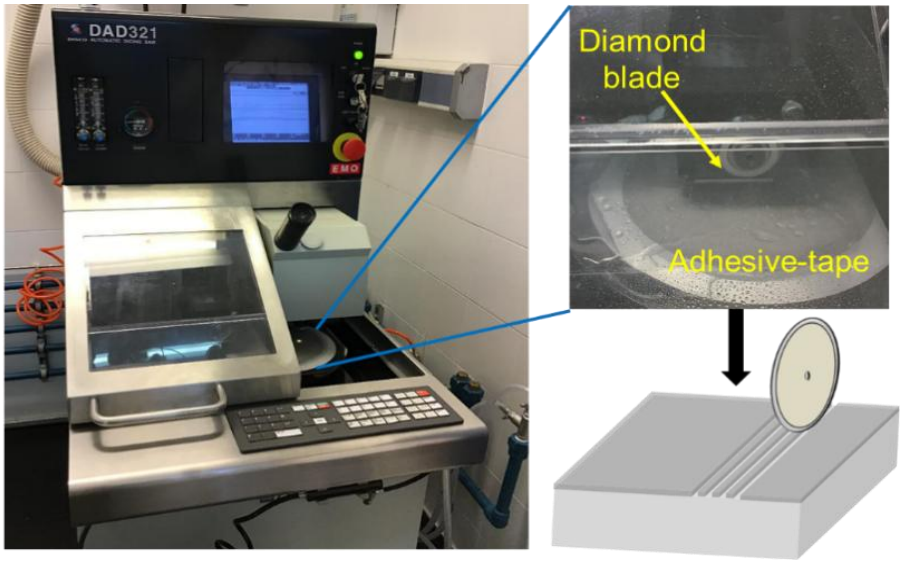

Figure 3.4 The Disco DAD 321 diamond dicing machine and schematic of the diamond saw diced (channel) ridge WGs.

In order to achieve a good quality ridge (channel), the type of the blade to be used, its rpm and the translation speed of the sample need to be optimized. For structuring the LPE grown $KY(WO_4)_2$ layer, a resin bonded blade with synthetic diamonds (P-series, Disco) was chosen. Resin bonding favours easy removal of the dull diamonds, bringing forth the new ones (i.e. self-sharpening). Hence, no separate blade dressing procedure was needed. Additionally, the excellent elasticity of such a blade would create less heating and friction, making it better suited for hard and brittle crystal materials. However, such a blade has a short lifetime as it wears out quickly. The blade that was used had an outer diameter of 54 mm. It had a thickness of 0.1 ± 0.002 mm, while the grit size was 6000.

Blades with larger grit size (smaller abrasive diamonds) would lead to smoother ridges, while small grit sizes would result in a deeper scratch and higher surface roughness [142].

The dicing parameters were optimized by performing various cuts on test samples of similar KREW crystals. The feed rate (i.e. distance traveled by the blade in each of its revolutions), was determined from the blade rotation and the translation speed. Values in the range of 0.15 – 0.3 μm/rev (limited by the maximum rotation speed) were tested by assessing the surface roughness of the cuts. The smaller feed rates gave the lowest surface roughness. Thus, for the LPE layer structured in this work, the feed rate of 0.15 μm/rev was selected (rotation speed: 40000 rpm, horizontal translation speed: 0.1 mm/s). The dicing depth was also optimized by the inspection of the channel side walls using a confocal microscope. During the dicing procedure, the blade and the sample were cooled with room temperature deionized water flowing at a rate of 1 l/min. It served as a lubricant during the cutting process and it also helped to remove the cutting debris from the region currently being diced.

3.2.2 Femtosecond direct laser writing

As it was discussed in chapter 2, fs-DLW has been implemented for fabricating channel WGs in the low-symmetry monoclinic KREW crystals [90, 143]. This method has an advantage in its flexibility (for achieving different channel geometry), simple fabrication steps and short fabrication time. This makes the method more desirable for fast prototyping. Unlike other methods, such as ion beam etching, mask preparation and photolithographic based design transfers are not needed. This makes it relatively cheaper and more favourable. In this thesis work, buried WGs (with a circular and a hexagonal optical-lattice-like cladding), surface WGs (with a half-ring-shaped cladding) and a Y-branch splitter (with a rectangular cladding) were fabricated. The different cladding geometries were realized using a computer script that allowed for pre-visualization of the intended designs. All the fabrications were performed in collaboration with Dr. J. R. Vázquez de Aldana, at the University of Salamanca, Spain.

The depressed-index channel WGs were fabricated using pulses from a Ti:Sapphire regenerative amplifier (Spitfire, Spectra Physics) with a 795 nm central wavelength and a 120 fs pulse duration. As the underlying modification process is based on the nonlinear absorption inside the samples, the fs-pulses needed to be tightly focused (i.e., to reach to the high-intensity level required for the inscription). A 40x microscope objective with a high numerical aperture ($N.A.$= 0.65) was used for this purpose. Considering a Gaussian shaped beam, the spot size of the laser at its focus was about $2w(\frac{1}{e^2})$ ~ 2 μm. Focusing such a Gaussian beam would lead to an asymmetric focal volume - elliptically shaped laser written track. An objective with lower $N.A.$ would further increase the asymmetry, while too large $N.A.$ would lead to the fast divergence of the laser at its focus (i.e. smaller modification region). The repetition frequency of the pulses (PRF) was 1 kHz.

During fs-DLW, the samples were translated through the laser focus with speeds of v ~ 0.4 – 0.5 mm/s, along the N_g principal optical axis, Fig.3.5. This procedure was repeated at different depth and lateral positions of a sample for achieving the desired cladding geometry. It should be noted that the translation speed needs to be optimized for achieving the best writing condition. For instance, a 40 μm core diameter circular cladding WG fabricated in a 3 mm long sample with v= 0.4 mm/s takes less than 6 minutes. However, if v is too slow, it might lead to severely damaged tracks resulting in a low-quality WG. Likewise, if it is too fast, there wouldn't be a strong enough modification, in which case the propagating light field (photons) can tunnel out of the cladding (as a radiation loss). The lateral separation between two adjacent tracks was 2 μm (for a circular cladding) and 8 μm (for a hexagonal cladding) WGs. The transverse thickness of the cladding and the magnitude of the refractive index reduction (at the cladding) are the key parameters that allow for controlling the WG loss related to the "leaky modes" [144]. In all cases, a bottom-up writing approach was implemented to ensure that the incoming pulses were not blocked or distorted by the previously made tracks.

The buried channel WGs were fabricated at a depth of 80 – 120 μm below the surfaces of the samples. The depth was optimized, as the efficiency of the nonlinear absorption and the optical aberration in the birefringent KREW crystal, determine the quality of the tracks. The incident pulse energy on the sample was controlled using a set of $\lambda/2$ plate, a linear polarizer, and a calibrated neutral density filter. For most of the WGs fabricated in this work, the

pulse energies were in the range of 50 – 80 nJ. For such pulse energy, after being tightly focused, the peak intensity at the focus was estimated to be ~ 13.2 – 18.5 TW/cm^2. Such a high peak intensity is needed to efficiently induce the nonlinear absorption process - generating enough free-electron plasma which is the origin of the material modification [78].

The polarization of the writing laser was set perpendicular to the sample's translation direction (i.e., E || N_m). All the implemented fabrication conditions (pulse energy, translation speed, writing depth and track separation) were achieved after performing numerous tests and optimizations on a test sample of KREW crystal. The schematic and photograph of the fs-DLW setup are shown in Fig. 3.5 (a, b).

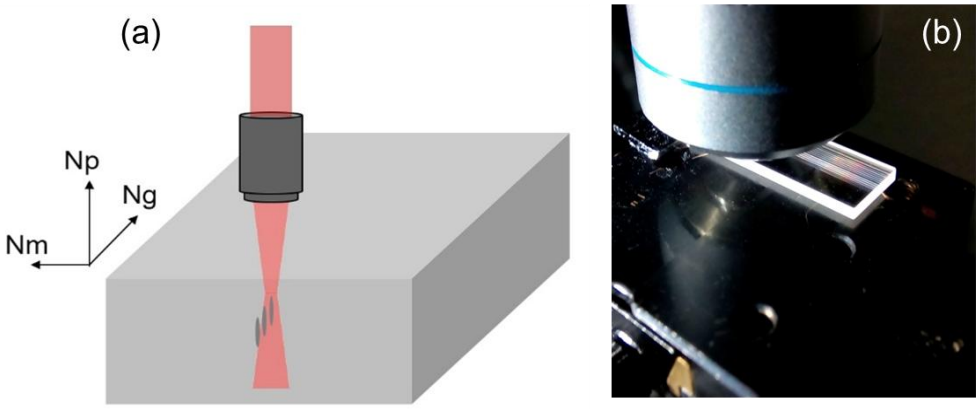

Figure 3.5 (a) Schematic of the fs-DLW; (b) photograph of the experimental setup.

3.3 Fabrication of single-walled carbon nanotubes

The single-walled carbon nanotubes (SWCNTs) SAs employed in the PQS experiments were fabricated in collaboration with the group of Prof. Fabian Rotermund, at the Korean Advanced Institute of Science and Technology, KAIST, South Korea. The details of the fabrication procedure have been reported in [119, 145].

As a starting material, commercially available SWCNTs (Mejio Nano Carbon Co. Ltd.) synthesized by an arc-discharge method were used. The tube diameters had a variation between ~1.5 to 2.2 nm. Initially, they were dried in a vacuum for more than 12 h and later dispersed in a 1,2-dichlorobenzen (o-DCB), with a concentration varying between 0.1 – 0 .35 mg/ml (i.e., for tuning and optimizing their nonlinear absorption). The dispersed SWCNTs were agitated for about 12 h using an Ultrasonicator (Sonoswiss, 600 W, 38 kHz). Subsequently, they were centrifuged for about 20 min, to induce sedimentation of the large bundles and the metal impurities. The upper portion of the centrifuged solution was carefully decanted and mixed with a separately prepared polymethyl solution (100 mg/ml in o-DCB). A volume ratio of 1:1 was implemented and the mixture was subsequently stirred overnight.

In order to fabricate a transmission-type SA, the SWCNT/PMMA film was spin-coated onto an uncoated ~1 mm-thick quartz substrate. For the evanescent field coupled SA, the film was directly spin coated onto the top surface of the sample containing the channel WGs. The WG end-facets were protected during the spin-coating procedure. The spin-coating speed was set to 1500 rev/min. Finally, the coated sample was placed on a vacuum oven (~ 150 ^{o}C), in order to dry the deposited film.

3.4 Fabrication of inkjet-printed graphene

The inkjet-printed graphene SA used in this work was fabricated and provided by the group of Prof. Mikael Ostling, at KTH Royal Institute of Technology, Sweden. The brief description of the fabrication procedure is given in this section. For further details, the reader is advised to refer to *Paper III* and references therein.

The distillation-assisted solvent exchange method [146] was used to prepare the graphene ink. Graphite in dimethylformamide (DMF) was ultrasonicated in order to get the graphene flakes by exfoliation. In order to stabilize the graphene flakes, 8 mg/ml of ethyl cellulose (Sigma-Aldrich, viscosity 22 cP for 5 w/v% in 80:20 toluene:ethanol) and 2 mg/ml of ethyl cellulose (Sigma-Aldrich, viscosity 4 cP for 5 w/v% in 80:20 toluene:ethanol) were added to the solution. Later, the DMF solvent was replaced by terpineol using distillation. Ethanol was used to dilute the dispersion with a volume ratio of 3:1(terpineol:ethanol). A commercial inkjet printer (DMP 2800, Dimatrix-Fujifilm Inc.), with 10 pL cartridges (DMC-11610) was used to print the graphene film onto a microscope slide serving as the substrate (SuperFrost slides, ~ 1 mm thickness). The graphene films were fabricated by implementing a 40 µm drop-spacing and a total of 20 printing passes. The jetting voltage was set to 27 V while the plate temperature was 45 ^{o}C. Finally, the substrate (with the printed graphene film) was dried for 1 h (at 80 ^{o}C) and annealed at 400 ^{o}C (for 1 h).

3.5 Spectroscopic characterization

3.5.1 µ-Raman mapping characterization

The Raman spectra of the Ln^{3+}- doped KREW crystals were studied in order to identify the different phonon modes. After the fs-DLW, the alteration of these vibrational modes (over the crystal surface) reveal the structural modifications induced by the laser writing procedure. The measurements were done using a Renishaw inVia Reflex confocal Raman microscope equipped with a 514 nm Ar^{+} laser and a 50x Leica objective. It has a monochromator for spectrally resolving the backscattered Raman signal and a filter for blocking the excitation laser. A set of $\lambda/2$ plate and a linear polarizer was used to select the orientation of the collected Raman signal.

After fabricating the fs-DLW channel WGs, the crystal quality and the modification at the laser written tracks as well as the induced-stress distribution were assessed by performing µ-Raman mapping characterization. This method is suited to characterize the integrity of the inherent crystal structure at the core regions of the fs-DLW WGs. For the mapping characterization, a similar equipment and measurement condition to that of the Raman spectroscopy described above was used. It should be noted that, for the fabricated channel WGs, the end-facet cross-sections are located on the N_p X N_m crystal plane and the mapping measurements were performed under $g(mm)\bar{g}$ measurement condition, i.e., N_g (N_m) – the propagation (polarization) direction of the excitation source and collected Raman signal.

During the mapping measurement, a high precision motorized 3D – stage was used to control the position of the excitation laser, by translating the sample. Initially, the end-facet of the WG would be aligned to be at the focus of the laser. The sample would then be translated up-wards by about 15 µm (i.e., the measurement would be performed slightly below the top surface of the sample). This was to avoid defocusing of the excitation laser when translating the sample across the measurement area. The *Wire 3.5™* software was used to set-up the measurement condition, to collect and analyse the data in order to create the final map. The Raman spectrum of the sample was taken with a spatial resolution of 0.4 µm, over the desired measurement area (containing the cladding structure of the WG). For most of the measurements, the typical area size was ~ 140 µm (N_p) x 140 µm (N_m). Once the measurement was completed, a Raman peak measured from the unmodified bulk region would be fitted using the Lorentzian function. The best fitting parameters were then used to assess, how the peak height (intensity), peak position and peak width of all the other measured spectra varied over the measured area. A 2D plot of these variations would create the desired maps, revealing the distinct nature of the laser modified areas (damage tracks).

3.5.2 µ-Luminescence mapping characterization

The µ-Luminescence mapping characterization of the WGs follows the same basic procedure as described in the µ-Raman mapping. In this case, the measured and analysed peaks are from the luminescence of the active Ln^{3+}dopants. The laser source needs to be chosen, considering its suitability for exciting the Ln^{3+} ions doped in the KREW sample. In WGs intended for laser application, such mapping gives unique access for monitoring the

emission property of the active ions in the core and the cladding regions. As the crystal field of the host material determines the level of the stark splitting (affecting the emission bands of the active ions), the lattice disorder induced by the fs-DLW could be investigated by monitoring the peak intensity, peak width and peak position (i.e. emission wavelength) of the luminescence signal. After performing the fitting procedure, the 2D µ-Luminescence map would be created. The mapping measurements were performed under $g(mm)\bar{g}$ measurement condition. For the Er^{3+} and Ho^{3+} - doped channel WGs, 514 nm and 488 nm excitation source were implemented, respectively.

3.6 Microscopic characterization

3.6.1 Confocal microscopy

Confocal imaging microscopy is a technique implemented for assessing the surface-topography of various samples with nanometric resolution [147]. Its non-contact nature makes it desirable for measuring delicate samples. The fs-DLW channel WGs were characterized using a confocal laser scanning microscopy (Carl Zeiss LSM 710). It incorporated a polarizer as well as an analyser and was operated in transmission mode. The illumination sources were from a GaN laser (405 nm) and an Ar^{+} ion laser (488 nm).

The cladding structures of the WGs were examined under polarized light illumination, in order to assess the degree of the damages and the spatial extent of the tracks. The presence of collateral damage, near the laser-written structure, was also studied. Such damage, under high pump power, could lead to fracture or cracking making the sample unusable. By performing a top-view study, the continuity of the damage tracks along the full length of the WG was investigated. using the end-facet study, the lateral and longitudinal extent of the tracks were estimated. Investigation with crossed polarizers (i.e. the two polarizers oriented along the optical indicatrix axes – perpendicular to each other) were performed to study the laser-induced-stress distributions arising from the fs-DLW procedure. All the characterizations were performed in collaboration with Prof. Viktor Zakharov and Prof. Andrey Veniaminov at the ITMO University, Saint Petersburg, Russia.

3.6.2 Environmental scanning electron microscopy

Environmental scanning electron microscopy (ESEM) is a powerful method for investigating the surface topography and the material structures in a wide range of samples [148]. For studying dielectric materials, as in this work, ESEM is better suited (than SEM), as it doesn't require deposition of a thin metallic coating. In ESEM, beams of electrons (from an electron-gun located in a high vacuum chamber) are used for bombarding the surface of the sample. Both the backscattered and the secondary electrons generated from the sample are captured for constructing the desired images. The electrons near the surface of the sample are ejected as secondary electrons. Hence, they reveal the surface topography information of the sample. The high energy electrons impinging the sample will traverse deeper. Therefore, the backscattered electrons arise due to the elastic scattering with the nuclei of the sample. Consequently, regions with different chemical compositions (average atomic numbers) will generate different level of brightness, on the images. In this work, a FEI Quanta 600 ESEM was used to investigate the surface topography of the diamonded saw diced channel WG. Additionally, for the epitaxially grown WGs, qualitative examinations of the layers were also performed with ESEM. As the samples were not conductive, all measurements were performed in low vacuum conditions.

3.7 Experimental setup for waveguide laser experiments

The scheme of the laser setup is shown in Fig.3.6. For the laser experiments, the samples were mounted on aluminium or copper holders using silver paste, to enhance the heat dissipation. The holders were mounted on a 4-axis optomechanical stage, with an angle adjustment for optimizing the coupling. For all the experiments, no active cooling of the holders or the samples were implemented. As pump sources, a Ti:Sapphire laser (tuned to 802 nm, E || N_m delivering a maximum of 2 W in CW) , a fiber-coupled InGaAs laser diode (981 nm, unpolarized) and an in-house Tm^{3+}:$KLu(WO_4)_2$ microchip laser (1.96 µm, E || N_m) were used for pumping the Tm^{3+}, Er^{3+}, and

Ho^{3+}- doped samples, respectively. During my research visit to the CIMAP laboratory, at the University of Caen Basse-Normandie, a Ti:Sapphire laser (tuned to 802 nm, E || N_m delivering a maximum of 3.2 W in CW and an Er^{3+}/ Yb^{3+} Raman fiber laser (1.68 µm, E || N_m) were used as pump sources.

A 10x microscope objective, with a long working distance (*W.D.*=30.5 mm) and $N.A.$= 0.28 was used to couple the Ti:Sapphire laser (with a spot size of $2w$= 40±5 µm, at the focus). The Er^{3+}/ Yb^{3+} Raman fiber laser was coupled with a spherical lens having a focal length of f = 50 mm. The focused pump spot diameter $2w$ was ~ 30 ± 5 µm. The fiber coupled InGaAs laser diode was collimated and focused using a lens assembly with a 1:1 imaging ratio and f = 30 mm. The pump spot size was ~ 105 µm. A pair of spherical lenses (making a telescope arrangement) with f = 150 mm (for collimation) and f = 60 mm (for coupling) were used. For the in-house Tm^{3+}:$KLu(WO_4)_2$ microchip laser, see Fig 3.7. All the coupling systems were placed on a separate 3 – axis optomechanical stage whose position can be adjusted with a micrometer resolution for fine-tuning the pump launching condition.

A spherical lens, placed on a similar 3 – axis optomechanical stage was used to collect and collimate the output beam. For further optimization of the pump coupling, a monitoring microscope camera (100x USB Digital microscope) was placed above the sample. The laser cavity consisted of a flat pump mirror (PM) that was anti-reflection (AR) coated for the pump wavelength and highly-reflective (HR) coated for the laser wavelength and a flat OC having different T_{oc} at the laser wavelength. The PM and the OC were placed on separate stages, which allowed for controlling the horizontal and vertical tilts of the mirrors (optimizing the cavity alignment). The air-gap between the mirrors and the WG end-facets were kept as minimum as possible. No index-matching liquid was used. Such liquid, under high pump power, might burn and damage the WG end-facets, prompting sample re-polishing or induce coating damage to the mirrors. The non-absorbed pump power was blocked using a suitable long pass filter.

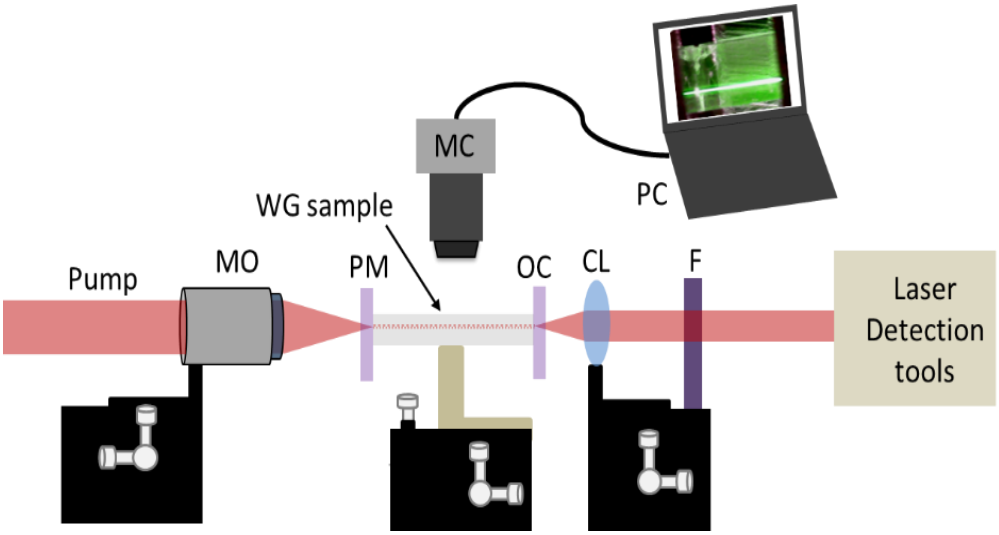

Figure.3.6. Schematics of the WG laser setup. MO – microscope objective, MC - microscope camera, CL – collimation lens, F – filter, PC – personal computer.

The characteristics of the output laser beam were measured/analyzed by implementing different detection (diagnostics) tools. To study the input-output characteristic, a sensitive power meter (Ophir Nova, P/N 1Z01500) was implemented. The emission spectrum was measured using an optical spectrum analyzer (Yokogawa, AQ6375B). The beam profile was captured with a FIND-R-SCOPE near-IR camera (model:85726, sensitivity: 0.4 – 2.2 µm). During the PQS laser operation, an InGaAs photodiode and a 2GHz Tektronix DPO5204B digital oscilloscope were implemented for measuring the pulse widths and the repetition frequencies. A photograph showing one of the laser setup (for the in-band pumped fs-DLW 5% Ho^{3+}:$KGd(WO_4)_2$ WG laser) is shown in Fig.3.7.

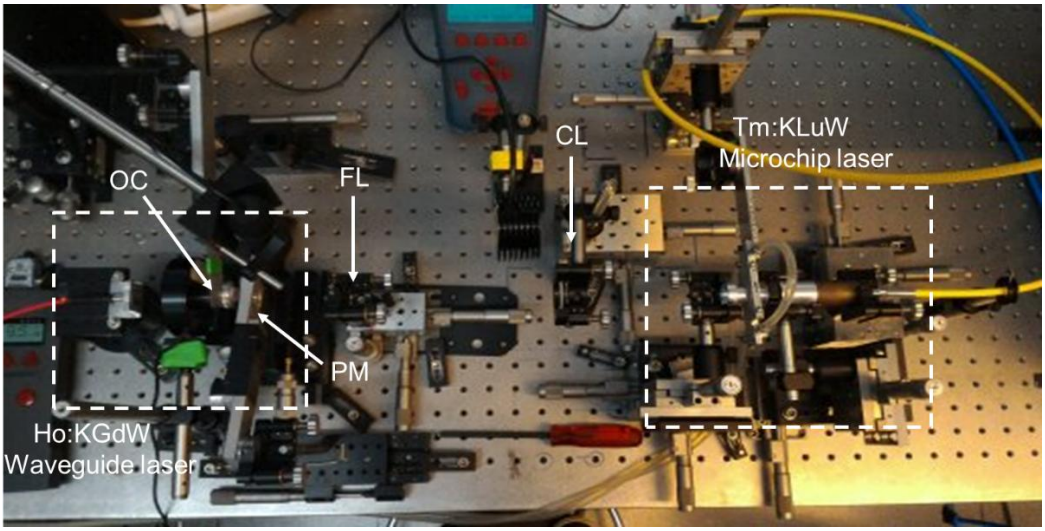

Figure.3.7. Photograph of the in-band pumped fs-DLW 5% Ho^{3+}:$KGd(WO_4)_2$ WG laser: CL and FL –collimating and focusing lenses, respectively.

3.8 Estimation of the refractive index contrast

The refractive index reduction (Δn), at the cladding region of the fs-DLW WG was estimated from the experimentally measured divergences θ (half-angle) of the laser beam. Using the approximation for the step-index WG, $N.A. \approx \sqrt{2n_c\Delta n} = sin(\theta)$, where n_c is the refractive index of the core region, the refractive index reduction (Δn) could be deduced [149]. For the epitaxially grown WGs, the dispersion curves of the undoped $KGd(WO_4)_2$, $KLu(WO_4)_2$ and $KY(WO_4)_2$ substrates, along the optical indicatrix axes were calculated using the published Sellmeier coefficients [150, 151]. As for the epitaxial layers, that comprise both active and inert dopant ions (Tm^{3+}, Lu^{3+}, Y^{3+}, Gd^{3+}), a linear approximation procedure [150] (i.e., considering a linear variation of the refractive indices, with the proportion of the dopant ions) was followed to estimate the refractive index contrasts with respect to the undoped substrates.

3.9 Estimation of the absorbed pump power and coupling efficiency

For the WG lasers studied in this work, the absorbed pump power was determined, in order to calculate the corresponding slope efficiencies. For instance, in the case of Tm^{3+}- doped WG, pump-transmission measurements at 802 nm and 830 nm (out of the Tm^{3+} ions absorption), were performed under non-lasing condition. Those values could be expressed, using the following relations.

$$p_f = \eta_f^2\,\eta_c(1-l^{in})\,p_i \qquad \text{for 830 nm measurement} \qquad (3.1)$$

$$p'_f = \eta_f^2\,\eta_c\left(1-l^{in}\right)(1-Abs)\,p'_i \qquad \text{for 802 nm measurement} \qquad (3.2)$$

Where p_f and p'_f are the transmitted pump powers measured after its propagation through the WG, p_i and p'_i are incident pump powers measured after the coupling objective, l^{in} is the internal passive propagation loss factor and η_f and η_c are the Fresnel loss and coupling efficiency, respectively. From equations.3.1 and 3.2, assuming all other parameters are similar (during the two measurements), the pump absorption (Abs) values at 802 nm could be deduced. Under non-lasing condition, the Abs values would decrease with an increase of the incident pump power (due to the bleaching of the ground state populations, in the quasi-3-level laser system). However, when the incident pump power reaches the laser threshold, the recycling effect will compensate the bleaching and the Abs value would remain fixed to its threshold value. Hence, this value would be used to calculate the

absorbed pump power. Alternatively, the small-signal absorption ($\eta_{abs,0}$), calculated from the spectroscopic parameters was also used to estimate the absorbed pump power. Knowing the Ln^{3+} doping level present in the sample $N_{Ln^{3+}}$ and the absorption cross-sections σ_a at the pump wavelength, the small-signal absorption, $\eta_{abs,0} = 1 - \exp(-\sigma_a l N_{Ln^{3+}})$ was calculated. The Fresnel loss $\eta_f = 1 - R$, where $R = \frac{(1-n_c)^2}{(1+n_c)^2}$, at the end-facets of the WG was calculated using the refractive index (n_c) of the sample and by assuming a normal incidence condition.

From the pump-transmission measurement discussed above, after determining the Fresnel and the propagation losses, the coupling efficiency η_c could be estimated. However, as a first order approximation, the pump coupling efficiency could also be estimated as the geometrical overlap between the focused pump beam and the WG core size. Nevertheless, for WGs which are strictly operating in the single-mode regime, a more rigorous approach based on the normalized overlap integral of the complex electric fields needs to be performed [79].

3.10 Estimation of the propagation loss

The optical attenuation (loss) of the pump and the laser beams are crucial issues limiting the performance of WG lasers. High propagation loss would result in diminished output power and lower slope efficiency. In the quasi-3-level lasers, the emission wavelength of the lasers would also be affected by the increase of the cavity loss. In WGs, the propagation loss is mainly constituted from the radiation, the absorption, and the scattering losses. The radiation loss is important in the low refractive index contrast WGs (such as the depressed-index cladding WGs), where the guided modes propagating inside the core are partially leaked into the cladding region. The absorption from the active dopants is useful (in lasers) while those from impurities and vacancy defects are unwanted. In high-quality crystals, the impurities and defects are negligible. The different imperfections, such as laser-induced cracks, dust-contaminants and surface roughness (from polishing and structuring), would lead to scattering loss.

A number of methods have been developed for estimating the WG propagation loss [152]. One such method is the cut-back technique [30] where the transmitted powers are measured, from the same sample, by progressively reducing its length (cutting back the sample). By comparing the transmitted power values, from the different sample lengths (assuming all the other parameters remained the same), the WG propagation loss could be estimated. However, due to the destructive nature of this method, it was not suited for WGs used in this work. The Fabry-Perot method [153], which is based on analysing the resonances of the cavity created between the two end-facets, is only applicable for single-mode WGs. The relatively simpler method, involving a careful measurement of the input and output powers from the WG (the so-called transmission method) was applied in this work. The measurement was performed by tuning the Ti:Saphhire source out of the absorption band of the active dopant ions, as discussed in the previous section. From such measurement, the propagation loss δ_{WG} could be calculated as,

$$\delta_{WG}(dB) = \frac{-10\, log(\frac{p_f}{\eta_f^2\, \eta_c p_i})}{l} \tag{3.3}$$

Where p_i is the incident power measured after the coupling optics and p_f is the transmitted power measured after propagating through the WG with the length l. From the knowledge of the Fresnel loss and the coupling efficiency, the propagation losses could be deduced.

3.11 Caird analysis to determine the propagation loss

The propagation loss of a WG operating as a laser can be experimentally deduced based on its lasing performance. The Findlay-clay method, which is applicable for lasers with no significant ground state bleaching (as in the 4-level laser system) is one of such methods [154]. By measuring the lasing thresholds, for the different T_{OC} mirrors, the upper limit of the propagation loss can be estimated. Another method that is more suited for the quasi-3-level laser system, is the so-called Caird analysis [155, 156]. In this work, the Caird analysis modified for

the case of high T_{OC} [157] is applied. The dependence of the experimentally measured slope efficiency η on T_{OC} and the intrinsic cavity loss per pass $L = L_{in}/2$ is expressed as,

$$\frac{1}{\eta} = \frac{1}{\eta_0}(1 + \frac{2\gamma}{\gamma_{OC}}) \tag{3.4}$$

$$\gamma = -\ ln(1 - L) \quad \text{and} \quad \gamma_{OC} = -\ ln(1 - T_{OC}) \tag{3.5}$$

Where, η_0 is the intrinsic slope efficiency, representing the ideal case where there is no intrinsic cavity loss and γ_{OC} is the output coupling loss. From the linear fitting of the plot showing the inverse of the experimental slope efficiency versus the inverse of the output coupling loss, the values for η_0 and 2γ would be extracted. The propagation loss of the WG is finally calculated using,

$$\delta_{WG}(dB) = \frac{4.34\ L}{l} \tag{3.6}$$

Chapter 4 Experimental results

The experimental results regarding the LPE and the fs-DLW WG fabrications as well as the confocal microscopy, μ-Raman, and μ-Luminescence mapping characterizations are briefly summarized in this chapter. They are shown for specific samples. The reader is referred to the corresponding published articles for further details on the rest of samples not shown here for the sake of brevity.

4.1 Epitaxially grown Tm^{3+} waveguides

As it was described in the previous chapter, the TSSG and LPE methods were implemented for fabricating the Tm^{3+} - doped planar and channel WGs. In the case of the TSSG method, the total growth process usually takes ~ 10 - 12 days, after which bulk crystals with an average size of ~10 x 12 x 25 mm^3 and weight of ~12.5 g were extracted, Fig.4.1(a). The bulk crystals were sliced (perpendicular to the *b*-crystallographic axis) ending up with (010) oriented substrates. The typical size of such a substrate was ~ *a** (8 mm) x *c* (15 mm) x *b* (2 mm), along its crystallographic axes. Usually, from a single bulk crystal, about 2 – 3 such substrates could be obtained for the LPE growth process. The photographs of the as-grown and the polished 5%Tm^{3+}- doped $KY_{0.61}Gd_{0.22}Lu_{0.12}(WO_4)_2$ LPE layer are shown in Fig.4.1(b, c), see *Paper II and III* for details.

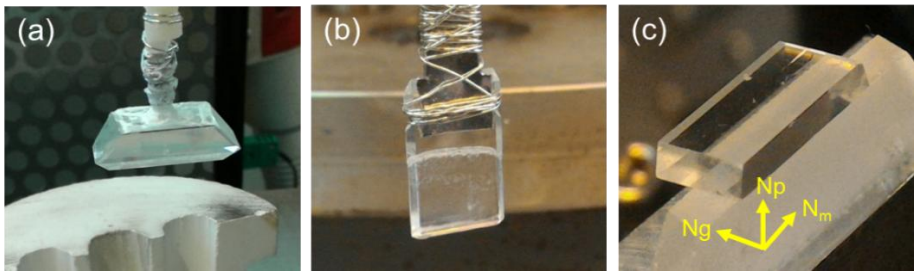

Figure 4.1(a) Undoped as-grown $KY(WO_4)_2$ bulk crystal; A 5%Tm^{3+} - doped $KY_{0.61}Gd_{0.22}Lu_{0.12}(WO_4)_2$ LPE (b) as-grown layer and (c) after cutting and polishing procedures. The white particulates seen on the as-grown layer are superficial and arise from evaporation of the solution,removed after rinsing with water.

4.2 Confocal microscopy characterization

In this thesis work, buried WGs (with a circular and a hexagonal optical-lattice-like cladding), surface WGs (with a half-ring-shaped cladding) and Y-branch splitters (with a rectangular cladding) were fabricated. For these WGs, a detailed characterization of the cladding structures was performed. The input and output facets were studied in transmission mode, using polarized light (being parallel to N_p) with λ = 405 nm, Fig.4.2 (a-d). The dark cladding regions formed by the damage tracks were clearly observed. The inner part (i.e., the core) was darker than the surrounding bulk region, which was attributed to the sample's illumination condition not perfectly matching the acceptance light cone of the WG and hence, the illumination source not being coupled into the core region.

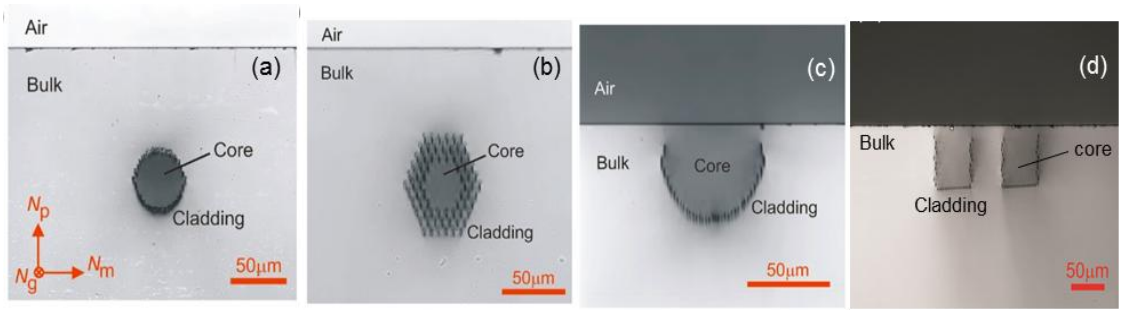

Figure 4.2 Depressed-index buried cladding WGs (a) with circular, (b) hexagonal optical-lattice-like geometry; (c) half-ring-shaped surface cladding (d) Y-branch splitter with rectangular cladding, in 3%Tm^{3+}:$KLu(WO_4)_2$ samples.

For the Y-branch WG, special attention was given to the splitting region in order to fine-tune the fabrication parameters and attain an optimum splitting performance. The top surface image contained a dark net-like structure representing the bottom of the WG cladding formed by the damage tracks, Fig. 4.3(a). The Y-junction appears to be much darker than the rest of the cladding because of the proximity of the two sets of damage tracks forming the inner "walls" of the two arms, Fig. 4.3(b). Furthermore, this area was inspected with crossed polarizers (being parallel to N_g and N_m, respectively, i.e. perpendicular to each other), see Fig. 4.3(c, d). For the optically biaxial KREW crystal placed between two crossed polarizers oriented along any of the two optical indicatrix axes, no light would be transmitted as seen in the black part of Fig. 4.3(c). However, the WG cladding in this figure appears as a bright area. This is due to the photo-elastic effect. The fs-laser writing induced an anisotropic stress field, which locally changed the orientation of the optical indicatrix axes. Note that the refractive index changes are strongly localized around the damage tracks which appears to be bright under a close view, Fig. 4.3(d). The Y-branch region corresponds to the stronger material modification as seen in Fig. 4.3(d). Further details regarding all the confocal studies discussed in this section are described in the respective papers (see *Paper VI – XII*).

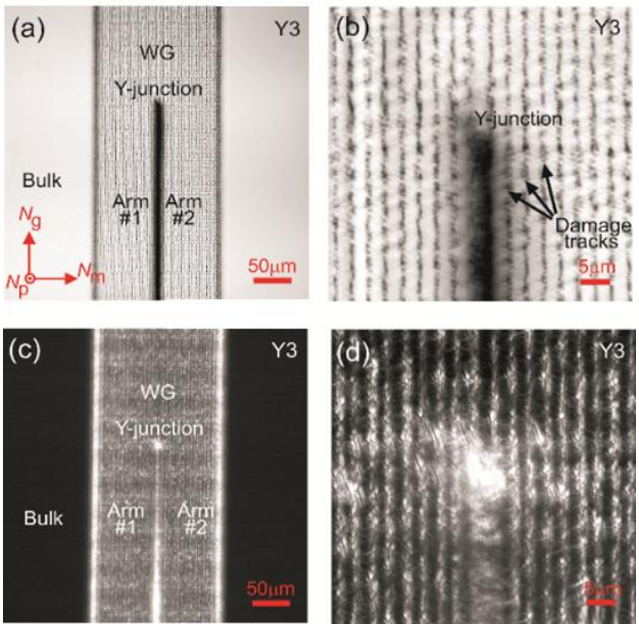

Figure 4.3. Top-view confocal laser microscopy study of the Y-branch for fs-DLW WG in a 3%Tm^{3+}:KLuW. Transmission mode, λ = 405 nm, (a,b) polarized light (|| N_m), (c,d) crossed polarizers (parallel to N_g and N_m, respectively). (b,d) a close view of the Y-branch structure.

4.3 μ-Raman mapping characterization

To characterize the crystal structure modification in the core and the cladding regions, a μ-Raman mapping analysis was performed. The results of such analysis for the fs-DLW 3%Tm^{3+}:KLuW WG with a hexagonal optical-lattice-like cladding structure are given in Fig 4.4. The two intense Raman modes, namely the 907.6 cm^{-1} and the 686.5 cm^{-1} were analysed, in order to create the 2D maps. Inside the core region, the crystalline quality of the material was preserved as the intensity of the Raman bands was almost similar to that of the bulk volume, see Fig. 4.4(a, d). This feature confirms the feasibility of the WG for lasing operation, as the intrinsic spectroscopic properties are kept unmodified. The cladding region consisted of a slightly damaged material as indicated by the decreased intensity as well as the broadening and the shifting of the phonon modes, Fig. 4.4 (a-f). The two latter effects are especially pronounced for the 686.5 cm^{-1} mode which is characteristic of the MDT structures (cf. section 3.2 of *Paper VII*). The existence of a residual anisotropic stress field was evident from the observed phonon energy shift outside the cladding regions, see Fig. 4.4 (c, f). Furthermore, the corresponding reduction in the peak intensity was ~ 40% (for 686.5 cm^{-1}) and ~ 36% (for 907.6 cm^{-1}) while the peaks shifted towards higher phonon energy with ~ 0.6 and 0.4 cm^{-1} for 686.5 and 907.6 cm^{-1} modes, respectively (see *Paper VII* for further details).

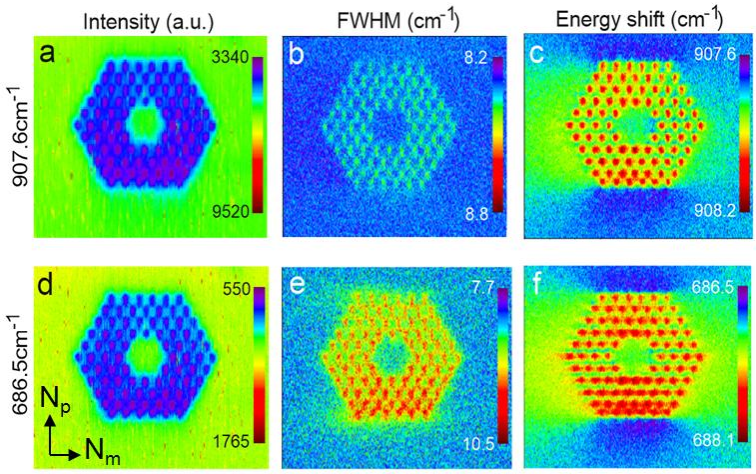

Figure 4.4. Micro-Raman mapping of the facet cross-section of the fs-DLW hexagonal optical-lattice-like cladding in a 3%Tm^{3+}:KLuW WG at 907.6 cm^{-1}: (a) peak intensity, (b) full width at half maximum (FWHM) and (c) phonon energy shift. Similar maps are given for the Raman band at 686.5 cm^{-1} in (d) peak intensity, (e) FWHM and (f) phonon energy shift. Excitation / detection light polarization is ***E*** || N_m.

4.4 μ-Luminescence mapping characterization

The μ-Luminescence mapping characterization gives unique access for monitoring the emission properties of the active ions in the core and the cladding regions. Such luminescence mapping measured from a buried channel WG in a 1% Er^{3+}- doped $KLu(WO_4)_2$ crystal is shown in Fig.4.5 (a-c). The luminescence peak at 552.8 nm, due to the Stark-to-Stark transition within the $^4S_{3/2} \rightarrow {}^4I_{15/2}$ emission band was monitored to create the 2D maps. In the WG core region, no notable change of the luminescence response is detected with respect to the bulk crystal, Fig.4.5 (a). In the WG cladding region, the luminescence intensity is suppressed and the Stark-to-Stark emission peak is broadened experiencing a red-shift. The former effect is attributed to the luminescence quenching by the fs-DLW induced color centers (structure imperfections) and the two latter effects – attributed to the slightly modified crystal-field arising from the lattice disorder in the cladding (see *Paper XI* for details). In Fig. 4.5 (b, c), a faded horizontal area extending over the WG cores were observed where the emission was weakly altered. It is attributed to the anisotropic stress field induced by the fs-DLW.

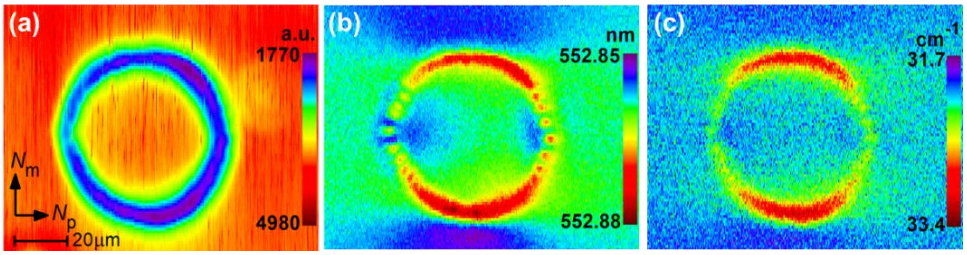

Figure.4.5. μ-luminescence mapping of the polished end-facet of a fs-DLW 1%Er^{3+}-doped $KLu(WO_4)_2$ WG for the $^4S_{3/2} \rightarrow {}^4I_{15/2}$ Er^{3+} transition: (a) luminescence intensity, (b) peak position, (c) peak width, λ_{exc} = 514 nm, λ_{lum} = 552.8 nm, excitation/detection light polarization is ***E*** || N_m

Chapter 5 Laser results

The main results regarding the CW and the PQS Ln^{3+} doped KREW WG lasers are described in this chapter. Some of the results are shown while the rest are referred to the corresponding published articles. The results are divided into three sections. First, the Tm^{3+} - doped WG lasers based on an epitaxially grown planar and channel structures are discussed. A more comprehensive and systematic study of the fs-DLW depressed-index buried and surface cladding WGs in Tm^{3+}- doped KREW materials are described next. For the PQS operation, different SAs (CVD/inkjet printed graphene, Cr^{2+}:ZnS/ZnSe, SWCNTs and MoS_2) were implemented, generating sub-100 nanosecond pulses with MHz repetition frequency ~ 2 µm. Finally, the prospect of other Ln^{3+} ions (i.e., Er^{3+} and Ho^{3+}) doped fs-DLW channel WGs in KREW hosts are presented.

5.1 Epitaxially grown Tm^{3+} waveguide lasers

5.1.1 3% Tm^{3+}:KYW buried planar waveguide laser

The WG core had a composition of $KY_{0.58}Gd_{0.22}Lu_{0.17}Tm_{0.03}(WO_4)_2$. The thickness of the core and the undoped cladding was 12.4 µm and 58 µm, respectively (see *Paper I* for further details). The length of the sample was l= 5 mm, along the N_g optical indicatrix axis. In the CW operation mode, using an OC with T_{OC}= 5%, the laser generated a maximum output power of 14.4 mW at 1835.4 nm. The slope efficiency was η=18 % (*vs.* P_{abs}). The laser threshold was at P_{abs}= 38 mW. Under lasing conditions, a bright – blue upconversion luminescence was observed from the Tm^{3+} ions (cf. chapter 2), Fig.5.1(a).

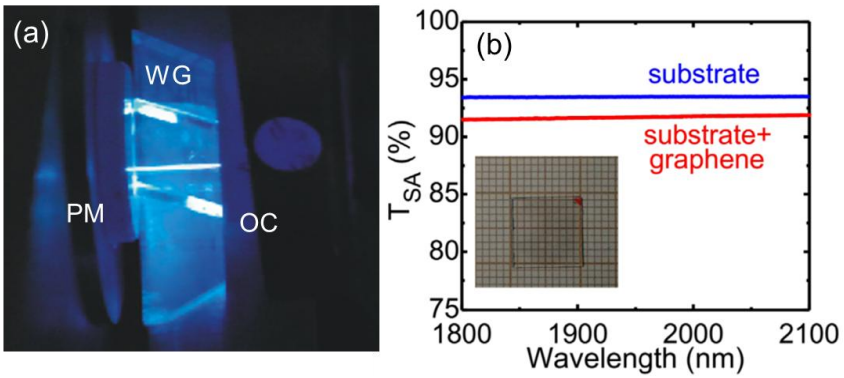

Figure 5.1. (a) Photograph of the 3%Tm^{3+}:KYW planar WG under lasing condition with the blue upconversion luminescence from the Tm^{3+} ions; (b) absorption spectrum of the graphene-SA, *inset*: image of the SA.

Using the same OC, the PQS operation was achieved by inserting a transmission-type graphene SA into the laser cavity. A commercial single – layer graphene (α_0'=2.3 %, I_{sat}=0.6 MW/cm^2 and α_s'= 0.12 %) fabricated by a CVD method was used, Fig.5.1(b). This work was the first demonstration of Tm^{3+}- doped double tungstate WG laser PQS by a graphene SA. The maximum average output power was 6.5 mW with η=9 % at a slightly blue-shifted wavelength of 1831.8 nm with respect to the CW operation mode. The conversion efficiency of this laser with respect to the CW operation mode was η_{conv}= 45 %. In both the CW and the PQS regimes, the laser polarization was linear and naturally selected by the gain anisotropy of the medium (E || N_m). The output beam profile was elliptical, extending along the none-guided direction of the planar WG (see *Paper I* for further details). Regarding the pulse characteristics, when the P_{abs} increased, the pulse duration τ_p (determined as FWHM) shortened from 312 to 195 ns and the pulse energy E_p increased from 2.3 to 5.8 nJ. This was accompanied by a nearly linear increase of the PRF, in the range 0.73 –1.13 MHz. Such a behaviour is typical for the PQS WG laser containing a "fast" SA. It is related to the variable bleaching of the SA (cf. chapter 2). The maximum peak power P_{peak} reached ~30 mW. These results were in reasonable agreement with the numerical modeling performed by considering the graphene as a "fast" SA. The intensity instability in the pulse trains were < 20% while the pulse-to-pulse timing jitter was < 15%. This is mainly due to the heating of the SA by the non – absorbed pump power.

Notably, those results in terms of the output power and the slope efficiency could be improved by implementing higher T_{OC} (i.e. increasing the η_{out}) at the cost of an increased P_{th}. Additionally, increasing the Tm^{3+} doping level is desirable for increasing the laser quantum efficiency (here, η_q ~ 1.66 for the 3%Tm^{3+}:KYW sample). In the PQS operation, further shortening of the τ_p and scaling of the E_p could be achieved by implementing SAs with higher MD. Although the upper cladding structure would help to reduce the scattering loss at the air-active layer interface, the fabrication of a surface planar WG would give a direct access to the active layer enabling the micro–structuring or direct functionalization.

5.1.2 5% Tm^{3+}:KYW surface planar waveguide laser

The active layer with a composition $KY_{0.61}Gd_{0.22}Lu_{0.12}Tm_{0.05}(WO_4)_2$ (i.e., 5%Tm^{3+}:KYW, η_q ~ 1.84) was grown by the LPE method. The layer was polished down to 18 µm thickness while the final WG length was 5 mm. No cladding layer was overgrown on the active layer resulting in a surface planar WG structure. In the CW operation, the maximum output power was achieved with T_{OC}= 30%, 154 mW at 1839.2 nm corresponding to η of 52.2% (*vs*. P_{abs}). The laser threshold was at P_{abs}= 104 mW. The propagation loss estimated by applying the Caird analysis amounted to 0.7±0.2 dB/cm. In the PQS operation mode (Fig.5.2 (a)) using a transmission type SWCNT SA (α_0'=2.6 %, I_{sat}= 7 MW/cm^2 and α_s'= 0.54 %, Fig.5.2 (b)), the laser generated a maximum average output power of 45.6 mW at 1835.4 nm with η = 22.5% (for T_{OC} = 30%). The η_{conv} was 29%.

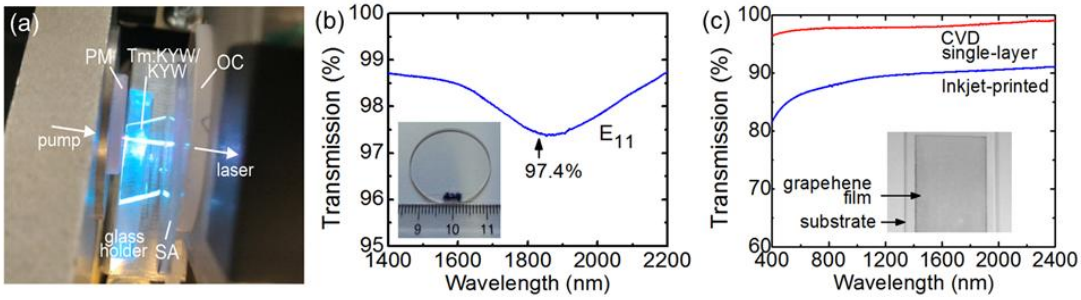

Figure 5.2. (a) Photograph of the blue upconversion luminescence from the PQS 5%Tm^{3+}:KYW planar WG laser with SWCNT-SA. Initial small-signal transmission of the (b) SWCNT-SA and (c) inkjet-printed graphene-SA, Fresnel losses are subtracted. *Insets* – image of the SAs.

During the PQS operation, the τ_p decreased from 161 to 83 ns, the E_p increased from 7.6 to 32.8 nJ and the PRF increased almost linearly from 0.94 to 1.39 MHz with P_{abs} (for T_{OC} = 30%). The shortest pulse duration (71 ns) corresponded to T_{OC}= 9% due to the higher intracavity peak intensity at the SA (~1.5 MW/cm^2). However, T_{OC} = 30% provided the highest E_p and, thus, the maximum P_{peak} reaching 395 mW, see *Paper II* for further details. The intensity fluctuation was < 20% and it was mostly attributed to the heating of the SA by the non-absorbed pump power.

For this WG, an inkjet printed graphene SA (α_0'=9.5 %, I_{sat}= 170 MW/cm^2 and α_s'= 6.5 %, Fig.5.2 (c)) was also tested using the optimum OC with T_{OC} = 30%. The maximum average output power was 26. 7 mW at 1834.2 nm with η = 11.3 %. The reduced output power and slope efficiency, as compared to those achieved with the SWCNTs SA (for the same T_{OC} = 30%), are partly attributed to the higher non-saturable loss present in the inkjet printed graphene SA. This is indeed supported by the slightly shorter PQS emission wavelength observed here, which in the quasi-3-level laser system indicates an extra cavity loss (cf. chapter 2). The best pulse characteristics were 98 ns / 21 nJ with a PRF of 1.27 MHz (intensity fluctuations < 25 %). The maximum peak power thus reached 214 mW, (See *paper III* for further details).

The improved slope efficiency (η > 50 %) achieved from the 5% Tm^{3+}:KYW planar WG laser, motivated a further optimization of the Tm^{3+}doping level in order to take advantage of the efficient CR process. This is especially favoured in such KREW laser media, as the high doping levels are not significantly affected by the fluorescence quenching due to the large interatomic distances (cf. chapter 2). In the case of a channel WG, as described in chapter 2, the high mode overlap between the pump and laser beams further increases the slope efficiency.

5.1.3 Diamond saw diced 10% Tm^{3+}:KYW channel waveguide laser

The LPE grown active layer with a composition of $KY_{0.61}Gd_{0.22}Lu_{0.07}Tm_{0.10}(WO_4)_2$ (i.e., 10% Tm^{3+}) had a thickness of 15.3 μm and the WG propagation length l was 3.5 mm. The surface channel WG was fabricated using a diamond dicing saw. The width of the channel (ridge) was 60.9±0.5 μm. The CW laser operation has been achieved with various OCs and also without any OC (relying on the Fresnel reflection, T_{OC} = 89%). In the latter case, a maximum output power of 262 mW at 1833 nm with a record slope efficiency η of 82.6% (*vs.* P_{abs}) was achieved, Fig.5.3(a).

The high η is due to the efficient CR among the Tm^{3+} ions, as expected for such high doping level (10 at.%) leading to a pump quantum efficiency η_q >1.96. Moreover, the high mode overlap efficiency (η_m~ 100%) and the large T_{OC} (leading to η_{out} ~ 92 ± 2%) resulted in a slope efficiency that is closer to the theoretical limit (cf. equation 2.25). The laser threshold was at P_{abs}= 214 mW. For smaller T_{OC}, η gradually decreased. The WG propagation loss was calculated (from the Caird plot) as δ =1.1±0.5 dB/cm. This value is slightly higher than the one for 5%Tm^{3+}:KYW planar WG. It is mostly assigned to the roughness of the WG side walls induced by the dicing.

A Photograph of the channel WG under lasing condition, with its bluish upconversion luminescence, is shown in Fig.5.3(b). The laser operated in multimode regime with the highest output power being from TE_{10} mode (see Fig. 6(a) of *Paper IV)*. From the numerical simulations, single transversal mode laser operation is expected with smaller channel width (i.e., 15 – 28 μm). Such single mode WG is favorable for implementing evanescent field interaction based PQS waveguide laser that can be extended towards an active biosensing platform.

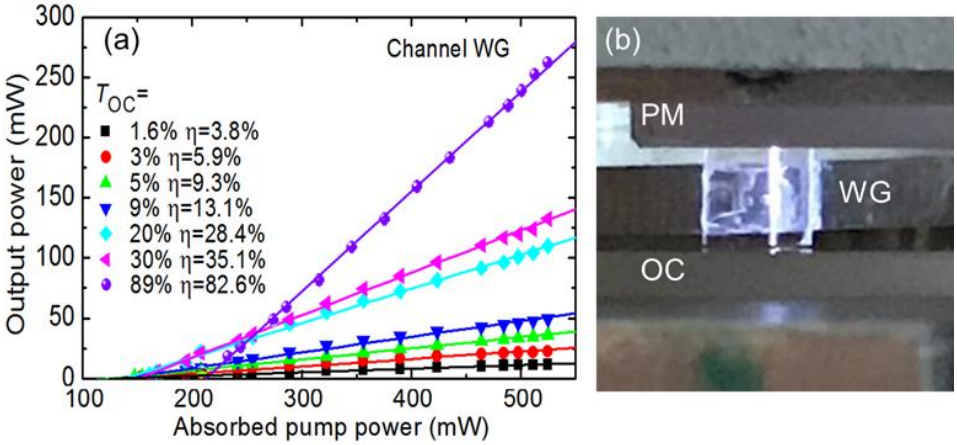

Figure 5.3. Diced 10%Tm^{3+}:KYW channel WG: (a) input-output dependences of the laser for various T_{OC}. η - slope efficiency; (b) photograph of the WG under lasing condition.

5.2 Fs-laser-written Tm^{3+} waveguide lasers

5.2.1 Buried waveguide lasers

The depressed-index buried WGs were fabricated in a bulk 3%Tm^{3+}:KLuW crystal. The length of this sample was l ~ 3mm. Two types of cladding structures were studied: those with a circular cladding having core diameters of 30 μm (W1), 40 μm (W2) and 50 μm (W3) or with a hexagonal optical-lattice-like cladding with a core diameter of 30 μm (W4).

The CW laser characteristics of the WGs were compared using a moderate transmission OC with T_{OC}= 9%. The best performance was observed from W2, with an output power of 46 mW at 1912 nm with η=15.2 % (*vs.* P_{abs}). The laser threshold was at P_{abs}= 21 mW, confirming the favourability of the channel WG for a lower laser threshold operation. For the other WGs, the output powers were slightly inferior, see *Paper V* for more details. Those results represented the first fs-DLW WG lasers in Tm^{3+} doped double tungstate crystal.

The PQS operation regime was realized using W2 and a transmission type SWCNTs SA (α_0'=2.6 %, I_{sat}= 7 MW/cm^2 and α_s'= 0.55 %). Two OCs having T_{OC} = 9% and 5% were tested. For T_{OC} = 9%, the laser generated a maximum average output power of 10.3 mW at ~1841 nm corresponding to η = 3.8%. The η_{conv} was 22%. The τ_p shortened from 98 to 50 ns and E_p increased from 2.7 to 7.0 nJ. The PRF increased almost linearly from 1.0 to 1.48 MHz, Fig. 5.4 (a, b). The maximum P_{peak} reached 141 mW.

The pulse duration (τ_p= 42 ns) achieved with T_{OC}= 5% is the record among all the PQS Tm^{3+} WG lasers reported to date using a "fast" SA (cf. table 5.1). The short τ_p is due to the use of a compact WG design (total cavity length: 4 mm) leading to a short T_R, a high intracavity intensity (due to the small T_{OC} and WG core size), and a high MD SA. It should be noted that the large gain cross-sections of Tm^{3+} in KLuW (cf. chapter 2) allowed for such a compact device. The intensity instability in the pulse train was < 20% and the pulse-to-pulse timing jitter was < 15 %, attributed to the heating of SA by the residual pump.

For this WG (W2), the laser performance with high transmission OCs (T_{OC}= 20% and 30%) was also studied. The maximum output power reached 247 mW at 1849.6 nm corresponding to a η of 48.7% *vs*. P_{abs} (for 30% OC). The optical-to-optical efficiency η_{opt} was 38.4% (see Fig.5 of *Paper VI*). The spectral shift (from ~1.91 µm for T_{OC}= 9% to ~1.85 µm for T_{OC}= 30%) was in agreement with the gain spectrum of Tm^{3+} in KLuW for light polarization E || N_m, (cf. Fig.2.8). The WG propagation loss was estimated using the Caird analysis as ~1.0±0.3 dB/cm.

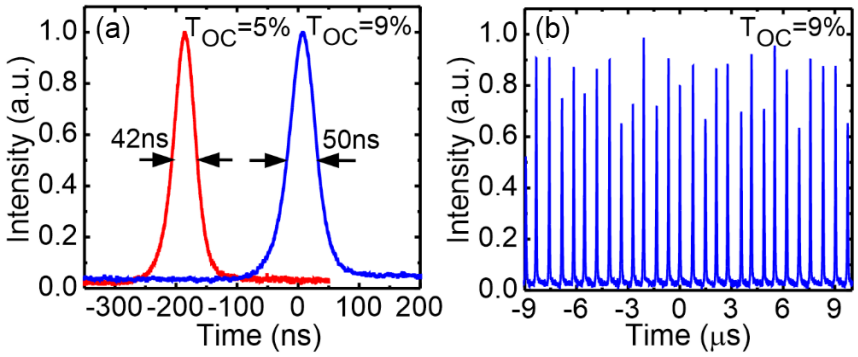

Figure 5.4. SWCNTs SA PQS fs-DLW 3%Tm^{3+}:KLuW WG laser: (a) oscilloscope traces of the shortest pulses; (b) the corresponding pulse train for T_{OC} = 9%, P_{abs} = 0.33 W.

A comparison between the performances of the two SAs (i.e. graphene and MoS_2), in the same laser cavity, was performed using W2 and the high T_{OC} . The detailed characteristics of the graphene (α_0'=5.7 %, I_{sat}= 0.6 MW/cm^2 and α_s'= 0.24 %) and MoS_2 (α_0'=4.5 %, I_{sat} ~ 0.5 MW/cm^2 and α_s'= 0.33 %) SAs were described in *Paper VI*. With T_{OC}= 30%, the laser generated 24.9 mW at 1844.8 nm with η = 9.3% (for graphene SA) and 22.1 mW at a shorter wavelength of 1843.4 nm with slightly lower η of 8.5% (for MoS_2 SA). The $\eta_{conv}$was 16.6% and 14.7% for graphene and MoS_2 SAs, respectively. For graphene SA, the best pulse characteristics were 88 ns / 18.0 nJ at a PRF of 1.39 MHz while for MoS_2 SA, it was 73 ns / 14.0 nJ at a slightly higher PRF of 1.58 MHz (see Fig.7 of *Paper VI*). These results were in agreement with the numerical modeling performed. The use of T_{OC}= 20% resulted in a shorter pulse duration for both graphene (72 ns) and MoS_2 (66 ns), due to the higher intracavity intensity on the SAs I_{in} reaching ~ 0.27 MW/cm^2. The *Q*-switching intensity instabilities were below 20%. The slightly shorter pulses with MoS_2 SA are explained by the larger fractional saturable loss (α_s'/α_o'= 0.074) as compared to the graphene SA (α_s'/α_o' = 0.042).

To summarise, the results discussed up to this point represent a notable improvement in the performance of the PQS Tm^{3+} WG lasers (cf. table 5.1). In particular, the relatively high average output power and slope efficiency while maintaining the sub-100 ns pulse duration. However, the pulse-to-pulse intensity instability arising mainly from the heating of the SA by the non-absorbed pump power was noted to be high (< 20 – 25%). This was mostly due to the direct nature of the interaction between the pump beam and the SA placed inside the laser cavity. Nevertheless, additional instabilities might also arise due to the temporal fluctuation of the pump source. The

conversion efficiency of the PQS WG lasers with respect to the CW operation was also limited, η_{conv}~15 – 45 %. One of the main reasons for this was the increased intracavity loss from the SA introduced into the laser cavity. The SA intrinsically possesses a non-saturable loss that might increase when being heated by the residual pump. The cavity misalignment would also increase the loss, affecting the achieved efficiency. Therefore, a PQS operation based on an indirect interaction between the SA (deposited onto the WG surfaces) and the propagating laser mode is expected to significantly improve those results.

5.2.2 Evanescent field -based passively *Q*-switched surface waveguide lasers

The depressed-index surface channel WGs were fabricated in a bulk 3%Tm^{3+}:KLuW crystal. The length of the sample l was 3.4 mm. Two WGs with core diameters of 50 and 60 µm were fabricated at the surface. Before the deposition of the SA (i.e., the thin PMMA film containing the randomly oriented SWCNTs), the CW performance of the WGs were studied. The 60 µm WG exhibited the best laser performance. For the optimum T_{OC} = 30%, the maximum CW output power was 171.1 mW at 1847.4 nm with η of 37.8 % (*vs.* P_{abs}). The laser threshold was at P_{abs} = 52 mW. The laser emitted at ~1.94 µm for small $T_{OC} \leq$ 5% and at ~1.85 µm for higher output coupling. The propagation losses estimated from the Caird analysis were δ = 0.7±0.3 dB/cm (for 60 µm WG) and δ = 0.9±0.3 dB/cm (for 50 µm WG). These losses were slightly lower as compared to the buried channel WGs described in the previous section. The laser mode was confined by the half-ring-shaped cladding from below and the air-crystal interface from above, resulting in a slightly asymmetric laser mode profile. This was in agreement with the numerically simulated mode profile (see *Paper VIII* for details).

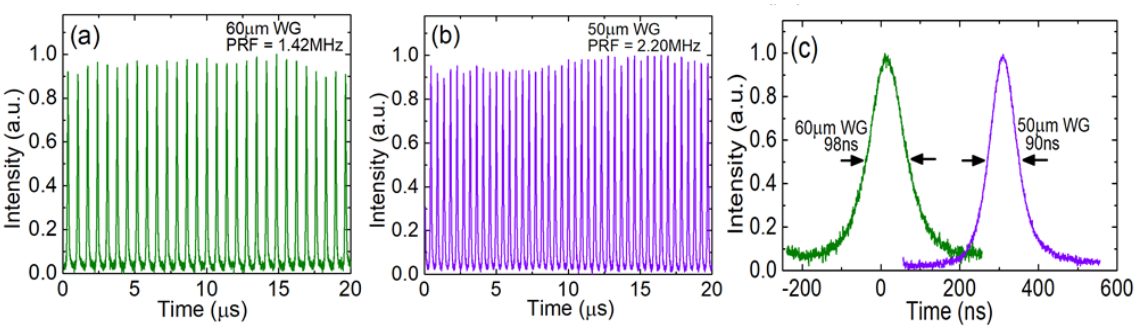

Figure 5.5. (a) Oscilloscope traces of (a,b) the pulse trains and (c) the corresponding single *Q*-switched pulses for the fs-DLW 3%Tm^{3+}:KLuW surface channel WG lasers PQS by evanescent-field interaction with SWCNTs SA. WG lasers with (a,c) 60 µm and (b,c) 50 µm cladding, T_{OC} = 30%, P_{abs}= 0.5 W.

The PQS operation was achieved based on the indirect interaction between the evanescent part of the laser mode and the surface deposited SWCNTs SA (α_0'=2.5 %, I_{sat}= 7 MW/cm^2 and α_s'= 0.52 %). No special cavity alignment was needed to observe the *Q*-switching. The 60 µm WG laser provided the best output performance. For T_{OC} = 30%, it generated a maximum average output power of 150 mW at 1846.8 nm with η = 34.6%, see Fig.12 (a, b) of *Paper VIII*. The η_{conv} was as high as 87.6%. Note that, the small blue-shift of the emission wavelength with respect to the CW laser and the high η_{conv} indicate the very low insertion loss for the SWCNTs SA. With the increase of P_{abs}, the τ_p shortened from 237 to 98 ns, the E_p increased from 24 to 105.6 nJ and the PRF increased from 0.86 to 1.42 MHz. The maximum P_{peak} reached 1.07 W. For the 50 µm WG laser, the best pulse characteristics were 52.2 nJ / 90 ns at a PRF of 2.20 MHz. The oscilloscope traces of the shortest single *Q*-switched pulses and the corresponding pulse trains are shown in Fig. 5.5(a – c). The intensity instability was <15% and the pulse-to-pulse timing jitter was <10% (for both WGs).

This work represents the first Tm^{3+} WG laser PQS by an evanescent field interaction with a surface deposited SA. The highest average output power (150 mW) and slope efficiency (34.6%) were achieved, as compared to the PQS results reported in the literature using a "fast" SA (cf. table 5.1). The use of a surface deposited SA has minimized the insertion loss, as indicated by the high η_{conv} (87.6%). The intensity instability in the pulse trains (<15%) has also improved, as compared to the results achieved with the transmission-type SAs. However, a shorter pulse (42 ns) was obtained from the buried channel WG with a transmission-type SWCNTs SA, as

described in section 5.2. Nevertheless, a shorter pulse from the PQS surface WG laser could be achieved by implementing a film containing a higher concentration of SWCNTs, thus increasing the MD of the deposited SA.

The results presented in this section were motivating for further extending (exploring) the work into a future active bio- and environmental sensing platform. One such possibility could be implementing the well-known Mach-Zehnder interferometer (MZI) based WG laser, incorporating an evanescent-field based sensing window on one of its arms. The responsive nature of the WG lasers towards an induced cavity loss in combination with a surface functionalization may lead to a sensitive and selective platform. The crucial building block in such MZI structure is the beam splitting and re-combining Y- branch. Such structure could also be used as an optical power distribution device, in a photonic integrated circuit. In this thesis work, such Y-branch structures were fabricated and tested.

5.2.3 Y-branch splitter based surface waveguide lasers

The 3%Tm^{3+}:KLuW sample with the depressed-index Y-branch surface WGs had a length l = 7.5 mm (along the N_g-axis).The cladding structures of the WGs had a rectangular cross-sections. Three Y-branch structures, all with the same depth (70 µm) and having different input/output width sizes were tested, Y1 (120 µm/60 + 60 µm with the output arms separation Δd_x=150 µm), Y2 (108 µm/54 + 54 µm, Δd_x=50 µm) and Y3 (180 µm/90 + 90 µm, Δd_x=100 µm). Additionally, a straight WG (S1) with 60×70 μm^2 cladding size was also fabricated, for comparison with the performance of the Y-branch WGs.

The CW operation of the Y-branch WGs was studied using various T_{OC}. The best performance corresponded to Y1 using the highest T_{OC} = 50% . The laser generated 0.46 W at 1841-1848 nm with a slope efficiency η of 40.6% (vs. P_{abs}). The laser threshold was at P_{abs} = 0.28 W and the η_{opt} was 31.5% (vs. P_{inc}). The laser output was linearly polarized and spatially multimode (TE_{12}/TE_{22}) with a power splitting ratio between the arms as 52.1/47.9%. The detailed mode analyses are given in *Paper IX*. By shifting the coupling position of the pump beam, the splitting ratio could be tuned and the laser could operate predominantly along one of its arm. For the straight WG S1, the output power reached 0.59 W at 1840–1855 nm with the maximum η = 44.2% and the lowest threshold of P_{abs}= 0.19 W as well as the highest η_{opt} of 37.2% (as compared to Y-branch WGs), Fig.5.6 (a, b).

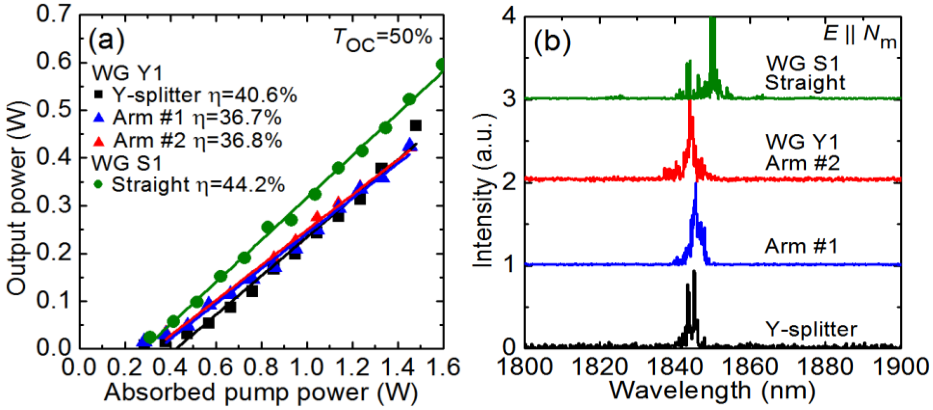

Figure 5.6. Fs-DLW 3%Tm^{3+}:KLuW Y-branch and straight WGs (Y1 and S1): (a) input-output dependences and (b) typical laser emission spectra measured at maximum P_{abs}, η – slope efficiency.

The result represents the first active Y-branch WGs fabricated in an anisotropic (low-symmetry, monoclinic) crystal by fs-DLW. It is promising for the fabrication of a more advanced structure such as the MZI for the envisioned application as an active optical sensor.

5.2.4 Power-scaling and in-band pumping of buried waveguide laser

In most of the results discussed in the previous sections, due to the limitation of the pump power, the achieved output powers were also limited. So, assessing the power scalability of the fs-DLW WGs towards a watt-level output would be interesting. Regarding PQS operation, all the implemented SAs were operating in the “fast” SA

regime, where the saturation happens due to the instantaneous intracavity intensity. The implementation of a "Slow" SA (saturated by the intracavity energy fluence) would lead to shorter pulses with high pulse energy. Furthermore, as one of the limitations of the achieved maximum η was the quantum defect (despite the efficient CR process available in Tm^{3+} ions), the implementation of a resonant (in-band) pumping scheme would lead to a higher η as well as a lower thermal load. Experiments aimed in addressing the aforementioned improvements were performed during my research visit to the CIMAP laboratory, at the University of Caen Basse-Normandie, France.

The depressed-index buried channel WG with a 40 μm core diameter in a 3%Tm^{3+}:KLuW crystal was implemented for the experiments. The length of the sample was l ~ 3mm. In the CW operation, the maximum output power reached 1.07 W at ~1.84 μm with η of 69.5% (*vs.* P_{abs}), for T_{OC}=50%. The laser threshold was at P_{abs} = 0.15 W and the η_{opt} = 38.2% (vs. P_{inc}). The Caird analysis was applied to determine the WG loss as δ = 1.3 ± 0.2 dB/cm. The laser operation without any OC (relying on the Fresnel reflection, T_{OC}=89%) generated an output power of 0.13 W at 1.83 μm with an increased laser threshold of P_{abs}= 0.34 W and a lower η=17.5% (see *Paper X* for details). With a special "band-pass" OC coated to support laser oscillation above 2 μm, a maximum output power of 0.35 W at 2004.6 nm with η=35% was achieved. Such long emission wavelength, from a Tm^{3+} laser, indicates a phonon-assisted electron transitions leading to the so-called "Vibronic" lasing regime.

For the PQS operation, the SA (polycrystalline Cr^{2+}:ZnS or Cr^{2+}:ZnSe) was inserted into the cavity, Fig.5.7(a). For T_{OC} = 50% with the Cr^{2+}:ZnSe SA exhibiting the lowest insertion loss (T_0 = 91%), the laser generated a maximum average output power of 0.43 W at 1.84 μm with a η = 48.9%, Fig.5.7(b) .The laser threshold was at P_{abs}= 0.27 W and the η_{conv} was 57.9%. The best pulse characteristics were 8.2 ns / 7 μJ at a PRF of 61.1 kHz. The P_{peak} was as high as 0.85 kW (see *Paper X* for details). For the Cr^{2+}:ZnS SA with the highest optical density (T_0 = 64.3%), the peak power reached 2.7 kW.

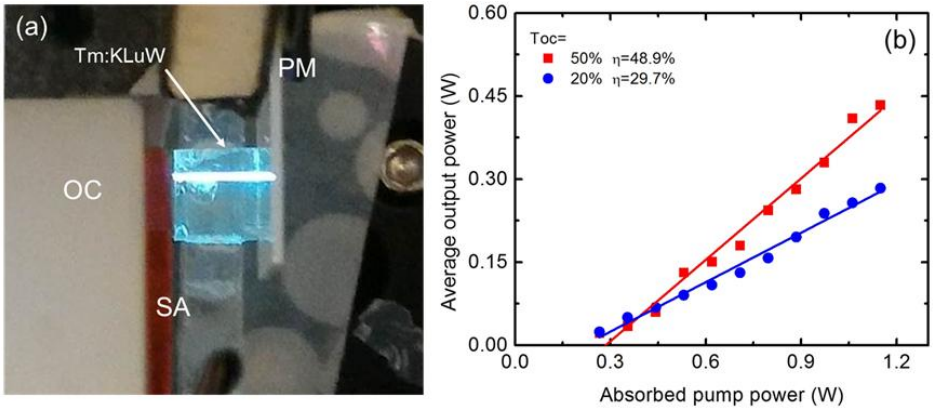

Figure 5.7. Fs-DLW 3%Tm^{3+}:KLuW WG laser PQS by Cr^{2+}:ZnSe SA (a) photograph showing the blue upconversion luminescence from the Tm^{3+} ions; (b) input-output dependences for T_{oc}=50% and 20%, η – slope efficiency.

Under in-band pumping at 1.68 μm, the maximum output power was 1.37 W at 1919.0 nm with η of 85.7% (*vs.* P_{abs}), for T_{OC} = 20%. The laser threshold was as low as P_{abs}=17 mW. The high stocks efficiency (η_{st}= 0.88), for such in-band pumping, resulted in a superior slope efficiency (η = 85.7%) as compared to the conventional 802 nm pumping. The lower laser threshold and the longer emission wavelength indicate a reduced intracavity loss, affirming the lower quantum defect in such pumping scheme (see *Paper X* for details).

Hence, the power scalability of the fs-DLW Tm^{3+} WG laser in KREW crystal has been demonstrated (cf. Table.5.2). Further power scaling towards a multi-watt output power seems feasible. Nevertheless, all the results discussed so far were based on the Tm^{3+} doped WG lasers typically operating slightly below 2 μm. Extending those works to cover other important spectral regions was also addressed in this thesis work. In this regard, fs-DLW Er^{3+}(~ 1.5 μm) and Ho^{3+} (~ 2.1 μm) doped WG lasers were fabricated and studied.

Table 5.1. Output characteristics of PQS Tm^{3+} waveguide lasers reported in the literature

Gain material	Geometry / fabrication*	SA	P_{out}, mW	η, %	$\Delta\tau$, ns	E_{out}, nJ	PRF, kHz	P_{peak}, mW	Ref.
Tm:ZBLAN	channel / fs	graphene	6	~5	2760	240	25	87	[158]
Tm:ZBLAN	channel / fs	Bi_2Te_3	16.3	1.3	1400	370	44.1	264	[116]
Tm:YAG	channel / fs	graphene	6.5	~2	<500	9.5	684	~20	[159]
Tm:KYW	planar / LPE	Cr^{2+}:ZnS	1.2	~3	1200	120	10	100	[74]
Tm:KYW	planar / LPE	graphene	6.5	9	195	5.8	1130	30	Paper I
Tm:KYW	planar / LPE	SWCNTs	45.6	22.5	83	33	1390	395	Paper II
Tm:KYW	planar / LPE	graphene Inkjet	26.7	11.3	98	21	1270	214	Paper III
Tm:KLuW	channel / fs	SWCNTs	10.3	3.8	50	7	1480	141	Paper V
Tm:KLuW	channel / fs	SWCNTs Evanec.	150	34.6	98	105.6	1420	1070	Paper VIII
Tm:KLuW	channel / fs	garphene	24.9	9.3	88	18	1390	210	Paper VI
Tm:KLuW	channel / fs	MoS_2	22.1	8.5	73	18	1580	190	Paper VI
Tm:KLuW	channel / fs	Cr^{2+}:ZnSe	430	48.9	8.2	7000	61.6	8.5 x10^5	Paper X
Tm:KLuW	channel / fs	Cr^{2+}:ZnS	55.4	-	2.6	6900	8	2.7 x10^6	Paper X

*fs – femtosecond direct laser writing; LPE – liquid phase epitaxy growth. Evanec. – evanescent filed interaction based saturable absorber. Inkjet – inkjet printed graphene saturable absorber.

Table 5.2. CW laser performance of fs-Laser-Written Tm^{3+} waveguides in the literature.

Material	Form	Pump	λ_p, nm	P_{th}, mW	P_{out}, mW	λ_L, nm	η, %	Ref.
Tm:ZBLAN	glass	diode	791	265	60	~1900	54^{Abs}	[160]
Tm:ZBLAN	glass	Ti:Sa	790	12	205	1890	67^{Abs}	[161]
Tm:GPNG	glass	Ti:Sa	791	80	32	1930	6^{Inc}	[162]
Tm:YAG	ceramics	Ti:Sa	800	312	93.2	1985	27^{Inc}	[163]
Tm:Lu_2O_3	ceramics	Ti:Sa	796	50	81	1942	7^{Inc}	[157]
Tm:YAG^t	crystal	Ti:Sa	-	100	48	1985	12^{Inc}	[164]
Tm:KLuW	crystal	EFL	1680	~17	**1370**	1919	**85.7^{Abs}**	*Paper X*
Tm:KLuW	crystal	Ti:Sa	802	150	**1070**	1850	**69.5^{Abs}**	*Paper X*

η – slope efficiency (superscript: η is calculated vs. the incident (*Inc*) or absorbed (*Abs*) pump power). EFL – erbium fiber laser.

5.3 Fs-laser-written Er^{3+} waveguide laser

A 60 μm core diameter depressed-index buried channel WG fabricated in a 1%Er^{3+}:KLuW crystal was studied. For this sample, the crystal growth is reported in [55] and detailed characterization of the fs-DLW WG is described in *Paper XI.* The sample had a length l of 3 mm. A fiber coupled InGaAs laser diode was used as a pump source. Its unpolarized emission at 981 nm was stabilized by a volume Bragg grating (emission bandwidth: 0.7 nm).

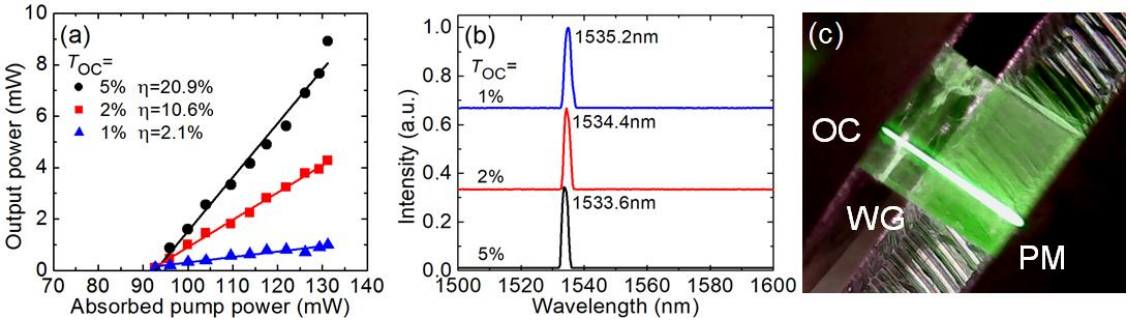

Figure 5.8. Diode-pumped fs-DLW 1%Er^{3+}:KLuW WG laser: (a) input-output dependences, η – slope efficiency; (b) typical laser emission spectra measured at P_{abs}= 116 mW; (c) photograph of the green upconversion luminescence from the Er^{3+}ions.

In the CW operation, the maximum output power corresponded to T_{OC} = 5%, namely 8.9 mW at 1533.6 nm with a slope efficiency η of 20.9% (vs. P_{abs}), see Fig.5.8(a, b). The laser threshold was at P_{abs} = 93 mW. For smaller output coupling, the laser output deteriorated: η = 10.6% and 2.1% for T_{OC} = 2% and 1%, respectively. The laser output was linearly polarized, E || N_m. It was naturally selected by the anisotropy of the gain.

The laser wavelength experienced a slight blue-shift with increasing T_{OC} from 1535.2 to 1533.6 nm in agreement with the quasi-3-level nature of Er^{3+} based lasers, Fig.5.8(b). According to the gain spectra of Er^{3+} in KLuW for light polarization E || N_m (cf. Fig.2.11), the local peak at ~1535 nm dominates for very high $\beta > 0.50$ (i.e. for strongly bleached WG). The photograph of the WG (under lasing conditions) showing a green upconversion luminescence is given in Fig.5.8 (c). This result represents the first ~1.5 μm fs-DLW Er^{3+} crystalline WG laser, as well as the first Er^{3+}-doped double tungstate WG laser (cf. Table 5.3), details are discussed in *Paper XI*. It is possible to improve the laser performance by optimizing the Er^{3+} doping concentration and the output coupling. Passive *Q*-switching of the Er^{3+} WG laser by implementing novel nanostructured saturable absorbers will further improve the result.

Table 5.3. CW laser performance of fs-Laser-Written Er^{3+} waveguides in the literature.

Material	Form	Pump	λ_p, nm	P_{th}, mW	P_{out}, mW	λ_L, nm	η, %	Ref.
Er, Yb:phosphate	glass	diode	976 & 980	142	80	1535	21.5^{inc}	[165]
Er, Yb:phosphate	glass	diode	975	330	1.7	1533	2^{inc}	[166]
Er, Yb:oxyfluoride-silicate	glass	diode	980&1480	350	0.03	1536	0.01^{inc}	[167]
Er, Yb:La-phosphate	glass	diode	976	350	5	1535	$\sim 2^{inc}$	[168]
Er, Yb:La-phosphate	glass	diode	976	21.6	112	1535	38.3^{abs}	[169]
Er:$LiLuF_4$	crystal	diode	974	1150	10	553	3^{inc}	[45]
Er:KLuW	crystal	diode	981	**93**	**8.9**	**1534**	$\mathbf{20.9}^{abs}$	*Paper XI*

η – slope efficiency (superscript: η is calculated vs. the incident (*Inc*) or absorbed (*Abs*) pump power).

5.4 Fs-laser-written Ho^{3+} and (Ho^{3+},Tm^{3+}) waveguide lasers

The laser performance of a depressed-index buried channel waveguide with a 60 μm diameter circular cladding inscribed in a 5%Ho^{3+}:$KGd(WO_4)_2$ was studied. The length of the sample was l = 5.5 mm. For T_{OC} = 30%, the laser generated a maximum output power of 212 mW with η of 67.2% (vs. P_{abs}). The laser threshold was at P_{abs} = 180 mW and the $\eta_{opt}$was 12.1%. The laser emitted at ~2055 nm for T_{OC} ≥ 3% and at ~2070 nm for lower transmission OCs. This spectral behaviour is in agreement with the gain spectra (cf. Fig.2.13). The propagation loss of the WG was estimated using the Caird analysis as δ = 0.94±0.2 dB/cm. The laser mode profile was spatially multimode, see Fig.7 of *Paper XII*. The first fs-DLW holmium WG laser based on an anisotropic (low-symmetry) crystalline material was demonstrated with this work (cf. Table 5.4).

An alternative scheme for exciting the Ho^{3+} ions is through Tm^{3+} ions, by taking advantage of the ET process in the co-doped materials. Such (Ho^{3+}, Tm^{3+}) co-doped WG laser was fabricated and characterized. A 50 μm core diameter depressed-index surface channel WG was fabricated in a 0.5% Ho^{3+} 5%Tm^{3+}: KLuW crystal. The length of the sample was l= 3 mm. The pumping scheme (at 1.68 μm) was in a quasi-CW mode. The input-output dependence of the laser is shown in Fig.5.9(a). For most of the studied OCs, a co-lasing from both Ho^{3+} and Tm^{3+} ions were observed. The maximum output power for the dominant Ho^{3+} emission was 147 mW at 2058.6 nm with a slope efficiency of η=14.5% (vs. P_{abs}), for T_{OC}= 3%. The laser threshold was at P_{abs}=157 mW.

For smaller transmission OCs (T_{OC} < 7%), the laser emission was dominantly from Ho^{3+} (~ 2.060 μm) while for intermediate OCs (T_{OC}= 7% and 9%), the ~1.95 μm emission from Tm^{3+} became stronger. For a high transmission T_{OC}= 20%, the laser emission was solely from the Tm^{3+} ions with a slightly shorter wavelength (~1.93 μm), Fig.5.9(b). Such spectral behaviour is related to the inversion level in the cavity. The finite efficiency of the

ET process also limits the Ho^{3+} lasing performance, as some of the pump energy is kept in the excited Tm^{3+} ions. Consequently, for high inversion levels (high T_{OC}), a significant amount of the Tm^{3+} ions are in the excited states and reach the lasing threshold first as compared to the Ho^{3+} ions.

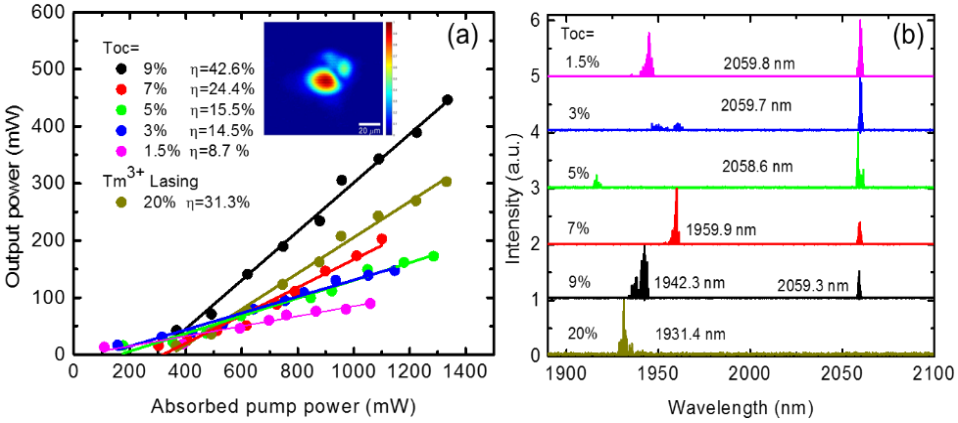

Figure 5.9. In-band pumped fs-DLW 0.5%Ho^{3+} 5%Tm^{3+}:KLuW WG laser:(a) input-output dependence, η – slope efficiency; (b) typical laser emission spectra measured at P_{abs}=0.7 W. (*unpublished work*)

The emission spectra of this laser (for T_{OC} = 3%) were monitored at different absorbed pump powers, Fig.5.10 (a). As P_{abs} increased (i.e. more Tm^{3+} ions get excited - β increases), more peaks start to appear near 1.94 μm where Tm^{3+} ions are known to emit. This observation was in agreement with Fig.5.9 (b). A photograph showing the green upconversion luminescence from the Ho^{3+} ions ($^5S_2 + {}^5F_4 \rightarrow {}^5I_8$ transitions) is given in Fig.5.10 (b). The measured far-field mode profile of the laser beam was spatially multimode, Fig.5.9 (a) *inset*. This work represents the first fs-DLW (Ho^{3+},Tm^{3+}) co-doped WG laser in crystalline material (cf. Tabel.5.4).

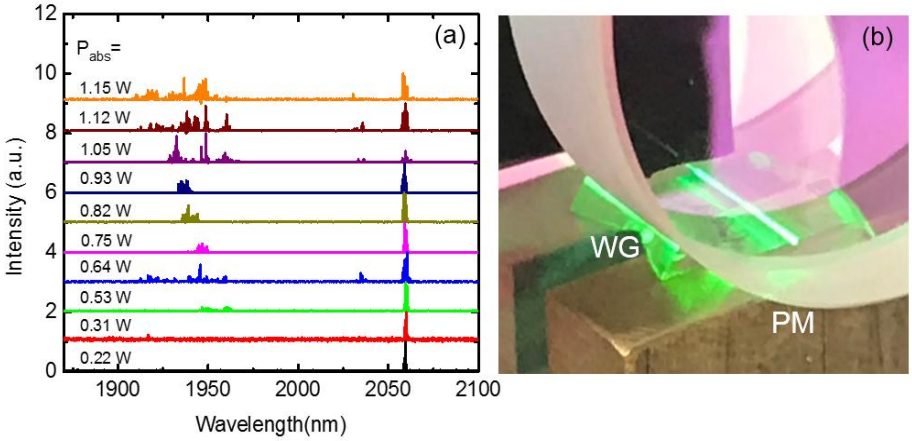

Figure 5.10. In-band pumped fs-DLW 0.5%Ho^{3+} 5%Tm^{3+}:KLuW WG laser:(a) emission spectra vs. absorbed pump power (P_{abs}), for T_{OC} = 3%; (b) photograph of the green upconversion luminescence from the Ho^{3+} ions. (unpublished work)

For the Ho^{3+} -doped WG laser, further power scaling to multi-watt output is possible by applying powerful pump sources (e.g., Tm^{3+} fiber lasers) and optimizing the Ho^{3+} doping concentration. The reduction of the WG diameter (below 30 μm) will provide single-transverse-mode operation. This will help to realize mode-locked WG laser capable of generating picosecond pulses with multi-GHz repetition frequency. Further optimization of the co-doping ratios would improve the results from the (Ho^{3+}, Tm^{3+}) co-doped WG laser.

Table 5.4. CW laser performance of fs-Laser-Written Ho^{3+} and (Ho^{3+},Tm^{3+}) waveguides in the literature.

Material	Form	Pump	λ_p, nm	P_{th}, mW	P_{out}, mW	λ_L, nm	η, %	Ref.
Ho:YAG	crystal	TFL	1908	3200	**1880**	2090	29^{Inc}	[170]
Ho,Yb:YAG	crystal	TFL	1908	~1800	330	2090	9^{Inc}	[170]
Ho:ZBLAN	glass	TFL	1945	104	1090	2070	50.9^{Inc}	[171]
Ho:ZBLAN	glass	diode	1150	28	26	2900	19.5^{Abs}	[172]
Ho:KGdW	crystal	TL	1960	180	212	2055	**67.2^{Abs}**	*Paper XII*
Ho,Tm:ZBLAN	glass	TiSa	790	**20**	76	2052	20^{Abs}	[98]
Ho,Tm:KLuW $^{q\text{-}CW}$	crystal	EFL	1680	157	**147**	2058	14.5^{Abs}	**

η – slope efficiency (superscript: η is calculated vs. the incident (*Inc*) or absorbed (*Abs*) pump power). EFL – erbium fiber laser. TFL – thulium fiber laser.TL – thulium laser. **Unpublished work.

Chapter 6 Conclusions and future work

6.1 Conclusions

This thesis work has dealt with the fabrication and the characterization of compact and efficient WG lasers operating in the CW and PQS operation regimes around 2 μm spectral range. To achieve this, thulium (Tm^{3+}), erbium (Er^{3+}), or holmium (Ho^{3+}) doped monoclinic double tungstate crystalline materials were employed. Those gain media were chosen due to their ability to generate polarized laser emission and their high gain cross-sections which make them suitable for achieving compact devices. The combination of TSSG, LPE, diamond saw dicing, and fs-DLW methods were employed for fabricating and structuring of the WGs. Furthermore, different characterization techniques (i.e., confocal microscopy, μ-Raman, and μ-luminescence mapping) were performed to assess the induced modifications and the preserved crystallinity of the fs-DLW WGs. In the PQS operation regime, the suitability of different SAs such as graphene (CVD and inkjet printed), SWCNTs, MoS_2, Cr^{2+}:ZnS and Cr^{2+}:ZnSe, were tested.

The first ~2 μm double tungstate WG laser passively *Q*-switched by a graphene SA was demonstrated. The laser was based on an epitaxially grown buried planar waveguide in a 3%Tm^{3+}- doped $KY_{0.58}Gd_{0.22}Lu_{0.17}(WO_4)_2$ crystal. Pulses with 5.8 nJ / 195 ns were achieved at 1831.8 nm with a PRF of 1.13 MHz.

The SWCNTs SA was shown to be very suitable for the passive *Q*-switching of ~2 μm WG lasers, as demonstrated with a 5%Tm^{3+}: $KY_{0.61}Gd_{0.22}Lu_{0.12}(WO_4)_2$ surface planar WG. The laser delivered sub-100 ns pulses (~71-83 ns) with > 1 MHz repetition rates. The maximum average output power was 46 mW, the slope efficiency 22.5% and the *Q*-switching conversion efficiency was 29%. Further shortening of the laser pulses down to few tens of nanoseconds is expected with a channel WG geometry. Passive *Q*-switching with an inkjet-printed graphene SA generated 98 ns/21 nJ pulses at 1834 nm with MHz repetition rate. Such printing technique is suited for the direct deposition of different nanostructured SAs onto the surface of the WGs.

The successful fabrication of an active (Tm^{3+}- doped) surface channel WG by combining the LPE and the diamond saw dicing methods was demonstrated in a monoclinic crystal. The highly-doped (10% Tm^{3+}) channel WG laser provided a moderate propagation loss of 1.1 ± 0.5 dB/cm and output power of 262 mW with a record slope efficiency of 82.6% due to the efficient Tm^{3+}-Tm^{3+} CR.

Fs-laser-written WG lasers in Tm^{3+} - doped double tungstate crystals were demonstrated for the first time. The passive *Q*-switching of a depressed-index buried cladding WG in a 3%Tm^{3+}:$KLu(WO_4)_2$ crystal using a transmission-type novel nanostructured saturable absorbers (graphene, SWCNTs, and MoS_2) exhibited promising performance. Pulse widths as short as 42 ns (SWCNTs) and 18 nJ pulse energy with ~1.4 MHz repetition frequency (graphene) were achieved. The pulse-to-pulse intensity instability was below 25% while the PQS conversion efficiency was ~ 22 %.

The first Tm^{3+} - doped WG laser PQS by an evanescent field interaction with a surface-deposited SA was presented. A half-ring shaped surface channel WG was fabricated in a 3%Tm^{3+}:$KLu(WO_4)_2$ crystal. A PMMA film containing a randomly oriented SWCNTs served as the SA. This configuration enabled relatively high pulse energy (105.6 nJ at 1846.8 nm), a high laser slope efficiency (34.6%), a high *Q*-switching conversion efficiency (approaching 90%) and a low pulse-to-pulse intensity instability (<15%). The WG laser operated in the MHz repetition range.

Fs-laser-written Tm^{3+} - doped channel WG laser delivered a watt-level output power (in CW regime) and a few-ns/μJ level pulse (in PQS regime) at ~2 μm. It was demonstrated based on a monoclinic 3%Tm^{3+}:$KLu(WO_4)_2$ sample and a Cr^{2+}:ZnS SA. The result represents the highest output power (1.07 W) and slope efficiency (69.5%), as well as the shortest PQS pulse (2.6 ns) from any fs-laser-written Tm^{3+} WG laser. Furthermore, the first in-band pumping (at ~1.68 μm) of the Tm^{3+} WG laser resulted in even higher output power (1.37 W) at ~1.9 μm with a record slope efficiency of 85.7%.

The first active Y-splitter fabricated in an anisotropic (low-symmetry, monoclinic) crystal by fs-laser-writing was studied. The laser generated a total output power of 0.46 W at ~1.84 μm with a slope efficiency of 40.6%. The power splitting ratio was almost 50/50%. The laser output was spatially multimode.

Based on a 1%Er^{3+}- doped $KLu(WO_4)_2$ sample, the first crystalline erbium WG laser was demonstrated. The laser generated 8.9 mW at 1533.6 nm (a wavelength corresponding to the telecom C-band) with a slope efficiency of 20.9 %.

The in-band pumping of the first fs-laser-written holmium WG laser based on a 5%Ho^{3+}:$KGd(WO_4)_2$ crystal generated a 212 mW at 2055 nm with a record slope efficiency of 67.2%. A promising result was also achieved from a (Ho^{3+},Tm^{3+}) co-doped fs-laser-written WG in a 0.5%Ho^{3+} 5%Tm^{3+}:$KLu(WO_4)_2$ crystal. For most of the studied output OCs, a co-lasing from both Ho^{3+} and Tm^{3+} ions were observed. The maximum output power for the dominant Ho^{3+} emission was 147 mW at 2058.6 nm with a slope efficiency of 14.5%. Further optimization of the co-doping ratios would improve the result towards an efficient laser emission at ~ 2.1μm.

6.2 Future work

6.2.1 Active waveguide sensor

The results achieved in this thesis work are encouraging for future research towards developing a compact device. One such possibility is to extend the work regarding the evanescent field interaction based PQS waveguide laser towards a sensing platform. For this, WG operating in a single transverse mode regime is preferred as it will give better control over the penetration depth and intensity of the evanescent field. The much-needed specificity in a sensing application can be accomplished through the functionalization of the deposited SA using a specific "bioreceptor". The direct coating of the cavity mirrors onto the WG facets and implementing a fiber-coupled system will increase the robustness of such a device. A microfluidic channel could be incorporated onto the surface of the functionalized WG for delivering the target molecules. During the PQS operation regime, a small intracavity loss would dramatically change the laser/pulse characteristics. Hence, the information gathered by monitoring the lasing characteristics (i.e., average output power, laser emission wavelength, and other pulse characteristics) may be analysed and correlated with the nature of the target molecules being sensed. The combination of WG lasing and surface functionalization may lead towards a sensitive and selective biosensor.

6.2.2 Mode-locking of waveguide laser

In addition to the power scaling of the Ho^{3+} WG lasers, the realization of Ho^{3+} based high repetition rate oscillators would be interesting for many applications. In such mode-locked (ML) operation regime, a single transverse mode WG is desirable in order to avoid intermodal dispersions that will affect the stability of the pulses. An optimized coupling and a minimum propagation loss are also desirable. However, the most crucial factor for efficient mode-locking of a WG laser is the controlling/compensation of the dispersion in the cavity. An interferometric dispersion control (based on the small air-gap available between the end-facet and the SA/OC) or implementation of a dispersive mirror would result in a compact ML WG laser capable of generating picosecond pulses with a multi-GHz repetition frequency.

6.2.3 Waveguide based pre-amplifier

The effective seed energy from the broadband supercontinuum (SC) sources that are implemented in Ho^{3+}:YLF based regenerative amplifier systems (operating ~ 2 μm) are usually low, in the pJ range. Therefore, a pre-amplification of the broadband SC spectrum around 2 μm is necessary to achieve a higher (nJ) seed energy level that is needed to prevent the instability arising during the amplification [173, 174]. Such pre-amplification could be implemented using a low-loss single transverse mode fs-laser-written Ho^{3+}:$KGd(WO_4)_2$ WG which has a high optical gain around ~ 2 μm (as noted from the CW lasing result).

References

1. T. H. Maiman, "Stimulated Optical Radiation in Ruby," Nature 187, 493-494 (1960).
2. K. Kincade, A. Nogee, G. Overton, D. Belforte, and C. Holton, "Annual Laser Market Review & Forecast: Lasers enabling lasers" (Laser Focus World, 2018), retrieved https://www.laserfocusworld.com/articles/print/volume-54/issue-01/features/annual-laser-market-review-forecast-lasers-enabling-lasers.html.
3. C.-H. Li, A. J. Benedick, P. Fendel, A. G. Glenday, F. X. Kärtner, D. F. Phillips, D. Sasselov, A. Szentgyorgyi, and R. L. Walsworth, "A laser frequency comb that enables radial velocity measurements with a precision of 1 cm s^{-1}," Nature 452, 610 (2008).
4. A. Giakoumaki, K. Melessanaki, and D. Anglos, "Laser-induced breakdown spectroscopy (LIBS) in archaeological science-applications and prospects," Analytical and bioanalytical chemistry 387, 749-760 (2007).
5. H. Kaushal and G. Kaddoum, "Applications of Lasers for Tactical Military Operations," IEEE Access 5, 20736-20753 (2017).
6. Q. Peng, A. Juzeniene, J. Chen, L. O. Svaasand, T. Warloe, K.-E. Giercksky, and J. Moan, "Lasers in medicine," Rep. Prog. Phys. 71, 056701 (2008).
7. U. N. Singh, B. M. Walsh, J. Yu, M. Petros, M. J. Kavaya, T. F. Refaat, and N. P. Barnes, "Twenty years of Tm:Ho:YLF and LuLiF laser development for global wind and carbon dioxide active remote sensing," Opt. Mater. Express 5, 827 (2015).
8. U. N. Singh, T. F. Refaat, J. Yu, M. Petros, and R. G. Remus, "Airborne active remote sensor for atmospheric carbon dioxide," SPIE Newsroom (2015).
9. E. Illy, H. Karlsson, and G. Elgcrona, "Important performance parameters when considering lasers for holographic applications," Proceedings of the 11th International Symposium on Display Holography-ISDH, 237-240 (2018).
10. A. H. Zewail, "Femtochemistry: Atomic-Scale Dynamics of the Chemical Bond," J. Phys. Chem. A 104, 5660-5694 (2000).
11. J. Dutta Majumdar and I. Manna, "Laser material processing," Int. Mater. Rev. 56, 341-388 (2013).
12. U. Umapathi, H.-T. Chen, S. Mueller, L. Wall, A. Seufert, and P. Baudisch, "LaserStacker," Proceedings of the 28th Annual ACM Symposium on User Interface Software & Technology, 575-582 (2015).
13. C. Vannahme, S. Klinkhammer, U. Lemmer, and T. Mappes, "Plastic lab-on-a-chip for fluorescence excitation with integrated organic semiconductor lasers," Opt. Express 19, 8179-8186 (2011).
14. H.-G. Rhee, "Lithography " in *Direct Laser Lithography and Its Applications*, M. Wang, ed. (IntechOpen, 2010), pp. 656 - 672.
15. G. J. Spühler, P. S. Golding, L. Krainer, I. J. Kilburn, P. A. Crosby, M. Brownell, K. J. Weingarten, R. Paschotta, M. Haiml, R. Grange, and U. Keller, "Multi-wavelength source with 25 GHz channel spacing tunable over C-band," Electron. Lett. 39, 778 (2003).
16. A. Javan, W. R. Bennett, and D. R. Herriott, "Population Inversion and Continuous Optical Maser Oscillation in a Gas Discharge Containing a He-Ne Mixture," Phys. Rev. Lett. 6, 106-110 (1961).
17. F. J. McClung and R. W. Hellwarth, "Giant Optical Pulsations from Ruby," J. Appl. Phys. 33, 828-829 (1962).
18. C. T. A. Brown, M. A. Cataluna, A. A. Lagatsky, E. U. Rafailov, M. B. Agate, C. G. Leburn, and W. Sibbett, "Compact laser-diode-based femtosecond sources," New J. Phys. 6, 175-175 (2004).
19. U. Keller, "Recent developments in compact ultrafast lasers," Nature 424, 831 (2003).

20. E. Cadiou, J.-B. Dherbecourt, G. Gorju, J.-M. Melkonian, A. Godard, J. Pelon, and M. Raybaut, "Atmospheric CO_2 measurements with a 2-µm DIAL instrument," EPJ Web of Conferences 176, 05045 (2018).
21. K. Scholle, S. Lamrini, P. Koopmann, and P. Fuhrberg, "2 µm Laser Sources and Their Possible Applications," in *Frontiers in Guided Wave Optics and Optoelectronics*, B. Pal, ed. (IntechOpen, 2010), pp. 471-500.
22. J. Geng and S. Jiang, "Fiber Lasers: The 2 µm Market Heats Up," Opt. Photon. News 25, 34-41 (2014).
23. E. Snitzer, "Optical Maser Action of Nd^{+3} in a Barium Crown Glass," Phys. Rev. Lett. 7, 444-446 (1961).
24. C. Grivas, "Optically pumped planar waveguide lasers, Part I: Fundamentals and fabrication techniques," Prog. Quant. Electron. 35, 159-239 (2011).
25. V. A. Orlovich, M. Pollnau, V. Panchenko, and I. A. Scherbakov, "Dielectric waveguide lasers," Exp. Mech. 6731, 67310Y (2007).
26. Y. J. Yuechen Jia and F. C. Feng Chen, "Compact solid-state waveguide lasers operating in the pulsed regime: a review [Invited]," Chin. Opt. Lett. 17, 012302 (2019).
27. C. Grivas, "Optically pumped planar waveguide lasers: Part II: Gain media, laser systems, and applications," Prog. Quant. Electron. 45-46, 3-160 (2016).
28. B. Saleh and M. Teich, *Fundamentals of Photonics, 3rd Edition* (Wiley, 2019).
29. C. R. Doerr and H. Kogelnik, "Dielectric Waveguide Theory," J. Light. Technol. 26, 1176-1187 (2008).
30. R. G. Hunsperger, *Integrated Optics, Theory and Technology* (Springer Verlag, 1982).
31. R. R. A. Syms and J. R. Cozens, *Optical guided waves and devices* (McGraw-Hill, 1992).
32. A. W. Snyder and J. D. Love, "Goos-Hänchen shift," Appl. Opt. 15, 236-238 (1976).
33. D. L. Lee, *Electromagnetic principles of integrated optics* (Wiley, New York, 1986).
34. H. Kogelnik, *Theory of Dielectric Waveguides. In: Integrated Optics.*, Topics in Applied Physics (Springer, 1975).
35. M. Eichhorn, "Quasi-three-level solid-state lasers in the near and mid infrared based on trivalent rare earth ions," Appl. Phys. B 93, 269-316 (2008).
36. X. Mateos, V. Petrov, M. Aguiló, R. M. Solé, J. Gavalda, J. Massons, F. Díaz, and U. Griebner, "Continuous-wave laser oscillation of Yb^{3+} in monoclinic $KLu(WO_4)_2$," IEEE J. Quantum Electron. 40, 1056-1059 (2004).
37. M. C. Pujol, R. Solé, J. Massons, J. Gavaldà, X. Solans, C. Zaldo, F. Díaz, and M. Aguiló, "Structural study of monoclinic $KGd(WO_4)_2$ and effects of lanthanide substitution," J. Appl.Cryst. 34, 1-6 (2001).
38. M. C. Pujol, A. Aznar, X. Mateos, X. Solans, J. Massons, S. Suriñach, F. Díaz, and M. Aguiló, "Structural redetermination, thermal expansion and refractive indices of $KLu(WO_4)_2$," J. Appl.Cryst. 39, 230-236 (2006).
39. X. Mateos, R. Solé, J. Gavaldà, M. Aguiló, J. Massons, and F. Díaz, "Crystal growth, optical and spectroscopic characterisation of monoclinic $KY(WO_4)_2$ co-doped with Er^{3+} and Yb^{3+}," Opt. Mat. 28, 423-431 (2006).
40. M. C. Pujol, M. Rico, C. Zaldo, R. Solé, V. Nikolov, X. Solans, M. Aguiló, and F. Díaz, "Crystalline structure and optical spectroscopy of Er^{3+}-doped $KGd(WO_4)_2$ single crystals," Appl. Phys. B 68, 187-197 (2014).
41. L. Chaoyang, B. Yong, Y. Feng, W. Zhichao, X. Yiting, W. Yuanbin, G. Hongwei, P. Qinjun, C. Dafu, and X. Zuyan, "106.5 W high beam quality diode-side-pumped Nd:YAG laser at 1123 nm," Opt. Express 18, 7923-7928 (2010).
42. X. Mateos, P. Loiko, J. M. Serres, K. Yumashev, U. Griebner, V. Petrov, M. Aguiló, and F. Díaz, "Efficient micro-lasers based on highly-doped monoclinic double tungstates," IEEE J. Quantum Electron. 53, 1-10 (2017).

43. K. van Dalfsen, S. Aravazhi, C. Grivas, S. M. García-Blanco, and M. Pollnau, "Thulium channel waveguide laser with 1.6 W of output power and ~80% slope efficiency," Opt. Lett. 39, 4380-4383 (2014).
44. Ò. Silvestre, J. Grau, M. C. Pujol, J. Massons, M. Aguiló, F. Díaz, M. T. Borowiec, A. Szewczyk, M. U. Gutowska, M. Massot, A. Salazar, and V. Petrov, "Thermal properties of monoclinic $KLu(WO_4)_2$ as a promising solid state laser host," Opt. Express 16, 5022-5034 (2008).
45. S. Chénais, F. Druon, S. Forget, F. Balembois, and P. Georges, "On thermal effects in solid-state lasers: The case of ytterbium-doped materials," Prog. Quant. Electron. 30, 89-153 (2006).
46. S. D. Jackson and T. A. King, "Theoretical Modeling of Tm-Doped Silica Fiber Lasers," J. Lightwave Technol. 17, 948 (1999).
47. X. Mateos, V. Petrov, J. Liu, M. C. Pujol, U. Griebner, M. Aguiló, F. Díaz, M. Galan, and G. Viera, "Efficient 2-µm Continuous-Wave Laser Oscillation of Tm^{3+}:$KLu(WO_4)_2$," IEEE J. Quantum Electron. 42, 1008-1015 (2006).
48. O. Silvestre, M. Pujol, M. Rico, F. Güell, M. Aguiló, and F. Díaz, "Thulium doped monoclinic $KLu(WO_4)_2$ single crystals: Growth and spectroscopy," Appl. Phys. B-Lasers Opt. 87, 707-716 (2007).
49. O. Silvestre, M. C. Pujol, R. Solé, W. Bolaños, J. J. Carvajal, J. Massons, M. Aguiló, and F. Diaz, "Ln^{3+}:$KLu(WO_4)_2$/$KLu(WO_4)_2$ epitaxial layers: Crystal growth and physical characterisation," Mater. Sci. Eng. B 146, 59-65 (2008).
50. V. Petrov, M. Cinta Pujol, X. Mateos, Ò. Silvestre, S. Rivier, M. Aguiló, R. M. Solé, J. Liu, U. Griebner, and F. Díaz, "Growth and properties of $KLu(WO_4)_2$, and novel ytterbium and thulium lasers based on this monoclinic crystalline host," Laser Photonics Rev. 1, 179-212 (2007).
51. A. S. Yasukevich, V. G. Shcherbitsky, V. E. Kisel, A. V. Mandrik, and N. V. Kuleshov, "Modified reciprocity method in laser crystals spectroscopy," Advanced Solid-State Photonics 2004, WB8 (2004).
52. S. Bjurshagen, P. Brynolfsson, V. Pasiskevicius, I. Parreu, M. C. Pujol, A. Pena, M. Aguilo, and F. Diaz, "Crystal growth, spectroscopic characterization, and eye-safe laser operation of erbium- and ytterbium-codoped $KLu(WO_4)_2$," Appl. Opt. 47, 656-665 (2008).
53. G. Karlsson, F. Laurell, J. Tellefsen, B. Denker, B. Galagan, V. Osiko, and S. Sverchkov, "Development and characterization of Yb-Er laser glass for high average power laser diode pumping," Appl. Phys. B 75, 41-46 (2014).
54. J. W. Kim, D. Y. Shen, J. K. Sahu, and W. A. Clarkson, "High-power in-band pumped Er:YAG laser at 1617 nm," Opt. Express 16, 5807 (2008).
55. J. M. Serres, P. Loiko, V. Jambunathan, X. Mateos, V. Vitkin, A. Lucianetti, T. Mocek, M. Aguiló, F. Díaz, U. Griebner, and V. Petrov, "Efficient diode-pumped Er:$KLu(WO_4)_2$ laser at ~ 1.6 µm," Opt. Lett. 43, 218-221 (2018).
56. V. Jambunathan, A. Schmidt, X. Mateos, M. C. Pujol, U. Griebner, V. Petrov, C. Zaldo, M. Aguiló, and F. Díaz, "Crystal growth, optical spectroscopy, and continuous-wave laser operation of co-doped (Ho,Tm):$KLu(WO_4)_2$ monoclinic crystals," J. Opt. Soc. Am. B 31, 1415-1421 (2014).
57. P. Loiko, J. M. Serres, X. Mateos, K. Yumashev, N. Kuleshov, V. Petrov, U. Griebner, M. Aguiló, and F. Díaz, "Microchip laser operation of Tm,Ho:KLu(WO(4))(2) crystal," Opt. Express 22, 27976-27984 (2014).
58. P. Loiko, J. M. Serres, X. Mateos, K. Yumashev, N. Kuleshov, V. Petrov, U. Griebner, M. Aguiló, and F. Díaz, "In-band-pumped Ho:$KLu(WO_4)_2$ microchip laser with 84% slope efficiency," Opt. Lett. 40, 344-347 (2015).
59. K. Scholle and P. Fuhrberg, "In-band pumping of high-power Ho:YAG lasers by laser diodes at 1.9 µm," Conference on Quantum Electronics and Laser Science, CLEO 2008, 1-2 (2008).

60. K. Mizutani, S. Ishii, M. Aoki, H. Iwai, R. Otsuka, H. Fukuoka, T. Isikawa, and A. Sato, "2 mum Doppler wind lidar with a Tm:fiber-laser-pumped Ho:YLF laser," Opt. Lett. 43, 202-205 (2018).
61. V. Jambunathan, X. Mateos, M. C. Pujol, J. J. Carvajal, F. Díaz, M. Aguiló, U. Griebner, and V. Petrov, "Continuous-wave laser generation at ~2.1 μm in Ho:KRE(WO_4)$_2$ (RE = Y, Gd, Lu) crystals: a comparative study," Opt. Express 19, 25279-25289 (2011).
62. H. Lin, F. Tang, W. Chen, W. Guo, Q. Huang, N. Wang, L. Guan, Y. Cao, and G. Zhang, "Diode-pumped tape casting planar waveguide YAG/Nd:YAG/YAG ceramic laser," Opt. Express 23, 8104-8112 (2015).
63. B. Yao, X. Li, T. Dai, Z. Cui, S. Bai, H. Yang, J. Li, Y. Ju, L. Ge, Y. Wang, and Y. Pan, "Diode-pumped tape casting planar waveguide YAG/Tm:YAG/YAG ceramic laser at 2013.76 nm," Opt. Lett. 41, 254-256 (2016).
64. I. J. Thomson, F. J. F. Monjardin, H. J. Baker, and D. R. Hall, "Efficient Operation of a 400 W Diode Side-Pumped Yb:YAG Planar Waveguide Laser," IEEE J. Quantum Electron. 47, 1336-1345 (2011).
65. J. I. Mackenzie, S. C. Mitchell, R. J. Beach, H. E. Meissner, and D. P. Shepherd, "15 W diode-side-pumped Tm:YAG waveguide laser at 2 [micro sign]m," Electron. Lett. 37, 898 (2001).
66. J. Martínez de Mendívil, J. del Hoyo, J. Solís, and G. Lifante, "Ridge waveguide laser in Nd:$LiNbO_3$ by Zn-diffusion and femtosecond-laser structuring," Opt. Mat. 62, 353-356 (2016).
67. J.-Y. Chen, J.-Y. Lv, Z.-Y. Wang, S.-B. Lin, H.-T. Guo, and C.-X. Liu, "Near-infrared optical properties and thermal stability of proton-implanted Er^{3+}/Yb^{3+} co-doped silicate glass waveguides," Results Phys. 12, 357-360 (2019).
68. P. Loiko and M. Pollnau, "Stochastic Model of Energy-Transfer Processes Among Rare-Earth Ions. Example of Al_2O_3:Tm^{3+}," J. Phys. Chem. C 120, 26480-26489 (2016).
69. J. A. Grant-Jacob, S. J. Beecher, T. L. Parsonage, P. Hua, J. I. Mackenzie, D. P. Shepherd, and R. W. Eason, "An 11.5 W Yb:YAG planar waveguide laser fabricated via pulsed laser deposition," Opt. Mater. Express 6, 91-96 (2016).
70. P. A. Atanasov, R. I. Tomov, J. Perriére, R. W. Eason, N. Vainos, A. Klini, A. Zherikhin, and E. Millon, "Growth of Nd:potassium gadolinium tungstate thin-film waveguides by pulsed laser deposition," Appl. Phys. Lett. 76, 2490-2492 (2000).
71. D. Geskus, S. Aravazhi, C. Grivas, K. Wörhoff, and M. Pollnau, "Microstructured KY(WO_4)$_2$:Gd^{3+}, Lu^{3+}, Yb^{3+} channel waveguide laser," Opt. Express 18, 8853-8858 (2010).
72. Y. Lu, P. Dekker, and M. J. Dawes, "Liquid-Phase Epitaxial Growth and Characterization of Nd:$YAl_3(BO_3)_4$ Optical Waveguides," Cryst. 9(2019).
73. S. Kurilchik, O. Dernovich, K. Gorbachenya, V. Kisel, I. Kolesova, A. Kravtsov, S. Guretsky, and N. Kuleshov, "Growth, spectroscopy, and laser characterization of Er:$KGd_xYb_yY_{1-x-y}(WO_4)_2$ epitaxial layers," Opt. Lett. 42, 4565-4568 (2017).
74. W. Bolaños, J. J. Carvajal, X. Mateos, E. Cantelar, G. Lifante, U. Griebner, V. Petrov, V. L. Panyutin, G. S. Murugan, J. S. Wilkinson, M. Aguiló, and F. Díaz, "Continuous-wave and Q-switched Tm-doped KY(WO_4)$_2$ planar waveguide laser at 1.84 μm," Opt. Express 19, 1449-1454 (2011).
75. X. Mateos, P. Loiko, S. Lamrini, K. Scholle, P. Fuhrberg, S. Suomalainen, A. Härkönen, M. Guina, S. Vatnik, I. Vedin, M. Aguiló, F. Díaz, Y. Wang, U. Griebner, and V. Petrov, "Ho:KY(WO_4)$_2$ thin-disk laser passively Q-switched by a GaSb-based SESAM," Opt. Express 26, 9011-9016 (2018).
76. K. Kodate, Y. Komai, and K. Okamoto, "Compact Spectroscopic Sensor Using an Arrayed Waveguide Grating," IEEE/LEOS International Conference on Optical MEMS and Nanophotonics 2007, 159-160 (2007).
77. K. M. Davis, K. Miura, N. Sugimoto, and K. Hirao, "Writing waveguides in glass with a femtosecond laser," Opt. Lett. 21, 1729-1731 (1996).

78. F. Chen and J. R. V. Aldana, "Optical waveguides in crystalline dielectric materials produced by femtosecond-laser micromachining," Laser Photonics Rev. 8, 251-275 (2014).
79. R. Osellame, G. Cerullo, and R. Ramponi, *Femtosecond Laser Micromachining Photonic and Microfluidic Devices in Transparent Materials* (Springer, 2012).
80. A. Kaiser, B. Rethfeld, M. Vicanek, and G. Simon, "Microscopic processes in dielectrics under irradiation by subpicosecond laser pulses," Phys. Rev. B 61, 11437-11450 (2000).
81. D. Choudhury, J. R. Macdonald, and A. K. Kar, "Ultrafast laser inscription: perspectives on future integrated applications," Laser Photonics Rev. 8, 827-846 (2014).
82. A. Okhrimchuk, "Femtosecond fabrication of waveguides in ion-doped laser crystals," in *Coherence and Ultrashort Pulse Laser Emission*, F. J. Duarte, ed. (InTechOpen, 2010).
83. H.-D. Nguyen, A. Ródenas, J. R. Vázquez de Aldana, J. Martínez, F. Chen, M. Aguiló, M. C. Pujol, and F. Díaz, "Heuristic modelling of laser written mid-infrared $LiNbO_3$ stressed-cladding waveguides," Opt. Express 24, 7777-7791 (2016).
84. T. Sabapathy, A. Ayiriveetil, A. K. Kar, S. Asokan, and S. J. Beecher, "Direct ultrafast laser written C-band waveguide amplifier in Er-doped chalcogenide glass," Opt. Mater. Express 2, 1556-1561 (2012).
85. W. Yang, C. Corbari, P. G. Kazansky, K. Sakaguchi, and I. C. S. Carvalho, "Low loss photonic components in high index bismuth borate glass by femtosecond laser direct writing," Opt. Express 16, 16215-16226 (2008).
86. C. Miese, S. Gross, M. J. Withford, and A. Fuerbach, "Waveguide inscription in Bismuth Germanate crystals using high repetition rate femtosecond lasers pulses," Opt. Mater. Express 5, 323-329 (2015).
87. G. Douglass, F. Dreisow, S. Gross, and M. J. Withford, "Femtosecond laser written arrayed waveguide gratings with integrated photonic lanterns," Opt. Express 26, 1497-1505 (2018).
88. A. Rodenas and A. K. Kar, "High-contrast step-index waveguides in borate nonlinear laser crystals by 3D laser writing," Opt. Express 19, 17820-17833 (2011).
89. J. R. Macdonald, R. R. Thomson, S. J. Beecher, N. D. Psaila, H. T. Bookey, and A. K. Kar, "Ultrafast laser inscription of near-infrared waveguides in polycrystalline ZnSe," Opt. Lett. 35, 4036-4038 (2010).
90. C. N. Borca, V. Apostolopoulos, F. Gardillou, H. G. Limberger, M. Pollnau, and R. P. Salathé, "Buried channel waveguides in Yb-doped $KY(WO_4)_2$ crystals fabricated by femtosecond laser irradiation," Appl. Surf. Sci. 253, 8300-8303 (2007).
91. S. M. Eaton, C. A. Merchant, R. Iyer, A. J. Zilkie, A. S. Helmy, J. S. Aitchison, P. R. Herman, D. Kraemer, R. J. D. Miller, C. Hnatovsky, and R. S. Taylor, "Raman gain from waveguides inscribed in $KGd(WO_4)_2$ by high repetition rate femtosecond laser," Appl. Phys. Lett. 92, 081105 (2008).
92. A. Ródenas, G. A. Torchia, G. Lifante, E. Cantelar, J. Lamela, F. Jaque, L. Roso, and D. Jaque, "Refractive index change mechanisms in femtosecond laser written ceramic Nd:YAG waveguides: micro-spectroscopy experiments and beam propagation calculations," Appl. Phys. B 95, 85-96 (2009).
93. G. Salamu, F. Jipa, M. Zamfirescu, and N. Pavel, "Laser emission from diode-pumped Nd:YAG ceramic waveguide lasers realized by direct femtosecond-laser writing technique," Opt. Express 22, 5177-5182 (2014).
94. H. Liu, Y. Jia, F. Chen, and J. R. Vázquez de Aldana, "Continuous wave laser operation in Nd:GGG depressed tubular cladding waveguides produced by inscription of femtosecond laser pulses," Opt. Mater. Express 3, 278 (2013).
95. Y. Jia, J. R. Vázquez de Aldana, and F. Chen, "Efficient waveguide lasers in femtosecond laser inscribed double-cladding waveguides of Yb:YAG ceramics," Opt. Mater. Express 3, 645 (2013).

96. F. Moglia, S. Müller, F. Reichert, P. W. Metz, T. Calmano, C. Kränkel, E. Heumann, and G. Huber, "Efficient upconversion-pumped continuous wave Er^{3+}:$LiLuF_4$ lasers," Opt. Mat. 42, 167-173 (2015).
97. H. Liu, S. Luo, B. Xu, H. Xu, Z. Cai, M. Hong, and P. Wu, "Femtosecond-laser micromachined Pr:YLF depressed cladding waveguide: Raman, fluorescence, and laser performance," Opt. Mater. Express 7, 3990-3997 (2017).
98. D. G. Lancaster, S. Gross, H. Ebendorff-Heidepriem, A. Fuerbach, M. J. Withford, and T. M. Monro, "2.1 μm waveguide laser fabricated by femtosecond laser direct-writing in Ho^{3+}, Tm^{3+}:ZBLAN glass," Opt. Lett. 37, 996-998 (2012).
99. N. Pavel, G. Salamu, F. Jipa, and M. Zamfirescu, "Diode-laser pumping into the emitting level for efficient lasing of depressed cladding waveguides realized in Nd:YVO4 by the direct femtosecond-laser writing technique," Opt. Express 22, 23057-23065 (2014).
100. F. Tso and R. Byer, "Modeling and CW operation of a quasi-three-level 946 nm Nd: YAG laser," IEEE J. Quantum Electron. 23, 605-612 (1987).
101. A. Choudhary, "Ultrafast waveguide lasers," Doctoral thesis (University of Southampton Southampton 2014).
102. F. Cornacchia, A. Toncelli, and M. Tonelli, "2-μm lasers with fluoride crystals: Research and development," Prog. Quant. Electron. 33, 61-109 (2009).
103. P. Koopmann, R. Peters, K. Petermann, and G. Huber, "Crystal growth, spectroscopy, and highly efficient laser operation of thulium-doped Lu_2O_3 around 2 μm," Appl. Phys. B 102, 19-24 (2011).
104. P. Loiko, P. Koopmann, X. Mateos, J. M. Serres, V. Jambunathan, A. Lucianetti, T. Mocek, M. Aguiló, F. Díaz, U. Griebner, V. Petrov, and C. Kränkel, "Highly Efficient, Compact Tm^{3+}:RE_2O_3 (RE = Y, Lu, Sc) Sesquioxide Lasers Based on Thermal Guiding," IEEE J. Sel. Top. Quantum Electron. 24, 1-13 (2018).
105. Z. Xiang, D. Wang, S. Pan, Y. Dong, Z. Zhao, T. Li, J. Ge, C. Liu, and J. Chen, "Beam quality improvement by gain guiding effect in end-pumped Nd:YVO_4 laser amplifiers," Opt. Express 19, 21060-21073 (2011).
106. J. M. Serres, X. Mateos, P. Loiko, K. Yumashev, N. Kuleshov, V. Petrov, U. Griebner, M. Aguiló, and F. Díaz, "Diode-pumped microchip Tm:$KLu(WO_4)_2$ laser with more than 3W of output power," Opt. Lett. 39, 4247-4250 (2014).
107. M. Delgado-Pinar, D. Zalvidea, A. Díez, P. Pérez-Millán, and M. V. Andrés, "Q-switching of an all-fiber laser by acousto-optic modulation of a fiber Bragg grating," Opt. Express 14, 1106-1112 (2006).
108. S. Ma, D. Lu, H. Yu, H. Zhang, X. Han, Q. Lu, C. Ma, and J. Wang, "High repetition rates optically active langasite electro-optically Q-switched laser at 1.34 μm," Opt. Express 25, 24007-24014 (2017).
109. G. J. Spühler, R. Paschotta, R. Fluck, B. Braun, M. Moser, G. Zhang, E. Gini, and U. Keller, "Experimentally confirmed design guidelines for passively Q-switched microchip lasers using semiconductor saturable absorbers," J. Opt. Soc. Am. B 16, 376-388 (1999).
110. J. M. Serres, P. Loiko, X. Mateos, H. Yu, H. Zhang, Y. Chen, V. Petrov, U. Griebner, K. Yumashev, M. Aguiló, and F. Díaz, "MoS_2 saturable absorber for passive Q-switching of Yb and Tm microchip lasers," Opt. Mater. Express 6, 3262 (2016).
111. P. Loiko, X. Mateos, S. Y. Choi, F. Rotermund, J. M. Serres, M. Aguiló, F. Díaz, K. Yumashev, U. Griebner, and V. Petrov, "Vibronic thulium laser at 2131 nm Q-switched by single-walled carbon nanotubes," J. Opt. Soc. Am. B 33, D19-D27 (2016).
112. A. S. Yasukevich, P. Loiko, N. V. Gusakova, J. M. Serres, X. Mateos, K. V. Yumashev, N. V. Kuleshov, V. Petrov, U. Griebner, M. Aguiló, and F. Díaz, "Modelling of graphene Q-switched Tm lasers," Opt. Commun. 389, 15-22 (2017).

113. M. S. Gaponenko, V. E. Kisel, N. V. Kuleshov, A. M. Malyarevich, K. V. Yumashev, and A. A. Onushchenko, "Passive mode locking of diode-pumped Tm:KYW laser with PbS quantum-dot-doped glass," Laser Phys. Lett. 7, 286-289 (2010).
114. M. Gaponenko, N. Kuleshov, and T. Südmeyer, "Microchip Tm:KYW Laser with 2.5 W of Output Power," CLEO: Science and Innovations, CLEO-SI 2015, SF1F.6 (2015).
115. H. Yu, V. Petrov, U. Griebner, D. Parisi, S. Veronesi, and M. Tonelli, "Compact passively Q-switched diode-pumped Tm:$LiLuF_4$ laser with 1.26 mJ output energy," Opt. Lett. 37, 2544-2546 (2012).
116. X. Jiang, S. Gross, H. Zhang, Z. Guo, M. J. Withford, and A. Fuerbach, "Bismuth telluride topological insulator nanosheet saturable absorbers for q-switched mode-locked Tm:ZBLAN waveguide lasers," Ann. Phys. 528, 543-550 (2016).
117. Y. Wang, G. Huang, H. Mu, S. Lin, J. Chen, S. Xiao, Q. Bao, and J. He, "Ultrafast recovery time and broadband saturable absorption properties of black phosphorus suspension," Appl. Phys. Lett. 107, 091905 (2015).
118. Y. G. Wang, H. R. Chen, X. M. Wen, W. F. Hsieh, and J. Tang, "A highly efficient graphene oxide absorber for Q-switched Nd:$GdVO_4$ lasers," Nanotechnology 22, 455203 (2011).
119. J. H. Yim, W. B. Cho, S. Lee, Y. H. Ahn, K. Kim, H. Lim, G. Steinmeyer, V. Petrov, U. Griebner, and F. Rotermund, "Fabrication and characterization of ultrafast carbon nanotube saturable absorbers for solid-state laser mode locking near 1μm," Appl. Phys. Lett. 93, 161106 (2008).
120. X. Mateos, P. Loiko, S. Y. Choi, F. Rotermund, M. Aguiló, F. Díaz, U. Griebner, and V. Petrov, "Single-walled carbon nanotubes oust graphene and semiconductor saturable absorbers in Q-switched solid-state lasers at 2 μm," Laser Phys. Lett. 14, 095801 (2017).
121. F. Rotermund, W. B. Cho, S. Y. Choi, I. H. Baek, J. H. Yim, S. Lee, A. Schmidt, G. Steinmeyer, U. Griebner, D. I. Yeom, K. Kim, and V. Petrov, "Mode-locking of solid-state lasers by single-walled carbon-nanotube based saturable absorbers," Quantum Electron. 42, 663-670 (2012).
122. S. M Bachilo, M. S Strano, C. Kittrell, R. Hauge, R. E Smalley, and R. Weisman, "Structure-Assigned Optical Spectra of Single-Walled Carbon Nanotubes," Science 298, 2361-2366 (2003).
123. Q. Bao, H. Zhang, Y. Wang, Z. Ni, Y. Yan, Z. X. Shen, K. P. Loh, and D. Y. Tang, "Atomic-Layer Graphene as a Saturable Absorber for Ultrafast Pulsed Lasers," Adv. Funct. Mater. 19, 3077-3083 (2009).
124. G. Xing, H. Guo, X. Zhang, T. C. Sum, and C. H. Huan, "The Physics of ultrafast saturable absorption in graphene," Opt. Express 18, 4564-4573 (2010).
125. F. Zhang, S. Han, Y. Liu, Z. Wang, and X. Xu, "Dependence of the saturable absorption of graphene upon excitation photon energy," Appl. Phys. Lett. 106, 091102 (2015).
126. J. Ma, G. Xie, P. Lv, W. Gao, P. Yuan, L. Qian, U. Griebner, V. Petrov, H. Yu, H. Zhang, and J. Wang, "Wavelength-versatile graphene-gold film saturable absorber mirror for ultra-broadband mode-locking of bulk lasers," Sci. Rep. 4, 5016 (2014).
127. J. Carvajal, M. Pujol, and F. Díaz, "High-Temperature Solution Growth: Application to Laser and Nonlinear Optical Crystals," in *Springer Handbook of Crystal Growth*, Dhanaraj G., Byrappa K., Prasad V., and D. M., eds. (Springer, 2010).
128. X. M. Ferré, "Crystal growth, optical characterization and laser operation of Yb^{3+} in monoclinic double tungstates," Doctoral Thesis (Universitat Rovira i Virgili, Tarragona, 2004).
129. W. B. Rodríguez, "Development and characterization of waveguide lasers on monoclinic potassium double tungstates," Doctoral Thesis (Universitat Rovira i Virgili, Tarragona, 2011).
130. R. Solé, V. Nikolov, X. Ruiz, J. Gavaldà, X. Solans, M. Aguiló, and F. Díaz, "Growth of β-$KGd_{1-x}Nd_x(WO_4)_2$ single crystals in $K_2W_2O_7$ solvents," J. Cryst. Growth 169, 600-603 (1996).
131. Y. Romanyuk, "liquid-phase epitaxy of doped $KY(WO_4)_2$ layers for waveguide lasers," Doctoral Thesis (Ecole polytechnique fédérale de lausanne, Lausanne, 2006).

132. A. Aznar, O. Silvestre, M. C. Pujol, R. Solé, M. Aguiló, and F. Díaz, "Liquid-Phase Epitaxy Crystal Growth of Monoclinic $KLu_{1-x}Yb_x(WO_4)_2/KLu(WO_4)_2$ Layers," Cryst. Growth Des 6, 1781-1787 (2006).
133. W. Bolaños, J. J. Carvajal, X. Mateos, G. S. Murugan, A. Z. Subramanian, J. S. Wilkinson, E. Cantelar, D. Jaque, G. Lifante, M. Aguiló, and F. Díaz, "Mirrorless buried waveguide laser in monoclinic double tungstates fabricated by a novel combination of ion milling and liquid phase epitaxy," Opt. Express 18, 26937-26945 (2010).
134. M. Pollnau, Y. Romanyuk, F. Gardillou, C. Borca, U. Griebner, S. Rivier, and V. Petrov, "Double Tungstate Lasers: From Bulk Toward On-Chip Integrated Waveguide Devices," IEEE J. Sel. Top. Quantum Electron. 13, 661-671 (2007).
135. D. Geskus, S. Aravazhi, K. Wörhoff, and M. Pollnau, "High-power, broadly tunable, and low-quantum-defect $KGd_{1-x}Lu_x(WO_4)_2:Yb^{3+}$ channel waveguide lasers," Opt. Express 18, 26107-26112 (2010).
136. W. Bolaños, J. J. Carvajal, M. Cinta Pujol, X. Mateos, G. Lifante, M. Aguiló, and F. Díaz, "Epitaxial Growth of Lattice Matched $KY_{1-x-y}Gd_xLu_y(WO_4)_2$ Thin Films on $KY(WO_4)_2$ Substrates for Waveguiding Applications," Cryst. Growth Des. 9, 3525-3531 (2009).
137. "Hardness of Materials" (Ted pella inc.), retrieved https://www.tedpella.com/company_html/hardness.htm.
138. K. van Dalfsen, S. Aravazhi, D. Geskus, K. Wörhoff, and M. Pollnau, "Efficient $KY_{1-x-y}Gd_xLu_y(WO_4)_2:Tm^{3+}$ channel waveguide lasers," Opt. Express 19, 5277-5282 (2011).
139. C. N. Borca, Y. E. Romanyuk, F. Gardillou, M. Pollnau, M. P. Bernal, and P. Moretti, "Optical channel waveguides in $KY(WO_4)_2:Yb^{3+}$," Lasers and Electro-Optics, CLEO 1-2 (2006).
140. A. Hooper, J. Ehorn, M. Brand, and C. Bassett, "Review of wafer dicing techniques for via-middle process 3DI/TSV ultrathin silicon device wafers," Proceedings - Electronic Components and Technology Conference 2015, 1436-1446 (2015).
141. L. G. Carpenter, "Precision dicing and micromilling of silica for photonics," Doctoral thesis (University of Southampton, , Southampton, 2013).
142. "Dicing blade operation recommendations" (UKAM Industrial Superhard Tools Division of LEL Diamond Tools International Inc.), retrieved https://www.ukam.com/dicingblade_operation_recommendations.htm.
143. F. M. Bain, A. A. Lagatsky, R. R. Thomson, N. D. Psaila, N. V. Kuleshov, A. K. Kar, W. Sibbett, and C. T. A. Brown, "Ultrafast laser inscribed $Yb:KGd(WO_4)_2$ and $Yb:KY(WO_4)_2$ channel waveguide lasers," Opt. Express 17, 22417-22422 (2009).
144. H. Karakuzu, M. Dubov, and S. Boscolo, "Control of the properties of micro-structured waveguides in lithium niobate crystal," Opt. Express 21, 17122-17130 (2013).
145. W. B. Cho, J. H. Yim, S. Y. Choi, S. Lee, A. Schmidt, G. Steinmeyer, U. Griebner, V. Petrov, D.-I. Yeom, K. Kim, and F. Rotermund, "Boosting the Non Linear Optical Response of Carbon Nanotube Saturable Absorbers for Broadband Mode-Locking of Bulk Lasers," Adv. Funct. Mat. 20, 1937-1943 (2010).
146. J. Li, F. Ye, S. Vaziri, M. Muhammed, M. C. Lemme, and M. Östling, "Efficient Inkjet Printing of Graphene," Adv. Mat. 25, 3985-3992 (2013).
147. S. W. Paddock, "Principles and practices of laser scanning confocal microscopy," Mol. biotechnol. 16, 127-149 (2000).
148. G. D. Danilatos, "Environmental scanning electron microscopy and microanalysis," Microchim. Acta 114, 143-155 (1994).
149. H. Liu, Q. An, F. Chen, J. R. Vázquez de Aldana, and B. del Rosal Rabes, "Continuous-wave lasing at 1.06µm in femtosecond laser written Nd:KGW waveguides," Opt. Mat. 37, 93-96 (2014).
150. S. Aravazhi, D. Geskus, K. van Dalfsen, S. A. Vázquez-Córdova, C. Grivas, U. Griebner, S. M. García-Blanco, and M. Pollnau, "Engineering lattice matching, doping level, and optical

properties of $KY(WO_4)_2$:Gd, Lu, Yb layers for a cladding-side-pumped channel waveguide laser," Appl. Phys. B 111, 433-446 (2013).

151. P. Loiko, P. Segonds, P. L. Inácio, A. Peña, J. Debray, D. Rytz, V. Filippov, K. Yumashev, M. C. Pujol, X. Mateos, M. Aguiló, F. Díaz, M. Eichhorn, and B. Boulanger, "Refined orientation of the optical axes as a function of wavelength in three monoclinic double tungstate crystals KRE(WO_4)_2 (RE = Gd, Y or Lu)," Opt. Mater. Express 6, 2984 (2016).
152. Tong and X. Colin, "Characterization Methodologies of Optical Waveguides. In: Advanced Materials for Integrated Optical Waveguides. ," in *Springer Series in Advanced Microelectronics*, Springer, ed. (Springer 2014).
153. R. Regener and W. Sohler, "Loss in low-finesse Ti:$LiNbO_3$ optical waveguide resonators," Appl. Phys. B: Lasers Opt. 36, 143-147 (1985).
154. D. Findlay and R. A. Clay, "The measurement of internal losses in 4-level lasers," Phys. Lett. 20, 277-278 (1966).
155. J. A. Caird, S. A. Payne, P. R. Staber, A. J. Ramponi, L. L. Chase, and W. F. Krupke, "Quantum electronic properties of the $Na_3Ga_2Li_3F$ 12:Cr^{3+} laser," IEEE J. Quantum Elect. 24, 1077-1099 (1988).
156. S. A. Payne, L. L. Chase, H. W. Newkirk, L. K. Smith, and W. F. Krupke, "$LiCaAlF_6$:Cr^{3+}: a promising new solid-state laser material," IEEE J. Quantum Elect. 24, 2243-2252 (1988).
157. J. Morris, N. K. Stevenson, H. T. Bookey, A. K. Kar, C. T. A. Brown, J. M. Hopkins, M. D. Dawson, and A. A. Lagatsky, "1.9 µm waveguide laser fabricated by ultrafast laser inscription in Tm:Lu_2O_3 ceramic," Opt. Express 25, 14910-14917 (2017).
158. J. H. Lee, S. Gross, B. V. Cunning, C. L. Brown, D. Kielpinski, T. M. Monro, and D. G. Lancaster, "Graphene-based passive Q-switching of a Tm^{3+}:ZBLAN short-infrared waveguide laser," Conference on Lasers and Electro-Optics (CLEO) - Laser Science to Photonic Applications, San Jose, CA, 1-2 (2014).
159. Y. Ren, G. Brown, R. Mary, G. Demetriou, D. Popa, F. Torrisi, A. C. Ferrari, F. Chen, and A. K. Kar, "7.8-GHz Graphene-Based 2-µm Monolithic Waveguide Laser," IEEE J. Sel. Top. Quantum Electron. 21, 395-400 (2015).
160. D. G. Lancaster, S. Gross, H. Ebendorff-Heidepriem, K. Kuan, T. M. Monro, M. Ams, A. Fuerbach, and M. J. Withford, "Fifty percent internal slope efficiency femtosecond direct-written Tm^{3+}:ZBLAN waveguide laser," Opt. Lett. 36, 1587-1589 (2011).
161. D. G. Lancaster, S. Gross, A. Fuerbach, H. E. Heidepriem, T. M. Monro, and M. J. Withford, "Versatile large-mode-area femtosecond laser-written Tm:ZBLAN glass chip lasers," Opt. Express 20, 27503-27509 (2012).
162. F. Fusari, R. R. Thomson, G. Jose, F. M. Bain, A. A. Lagatsky, N. D. Psaila, A. K. Kar, A. Jha, W. Sibbett, and C. T. A. Brown, "Lasing action at around 1.9 µm from an ultrafast laser inscribed Tm-doped glass waveguide," Opt. Lett. 36, 1566-1568 (2011).
163. Y. Ren, G. Brown, A. Ródenas, S. Beecher, F. Chen, and A. K. Kar, "Mid-infrared waveguide lasers in rare-earth-doped YAG," Opt. Lett. 37, 3339-3341 (2012).
164. Y. Y. Ren, S. J. Beecher, G. Brown, A. Rodenas, A. Lancaster, F. Chen, and A. K. Kar, "Q-switched mode-locking of a mid-infrared Tm:YAG waveguide laser with graphene film," Pacific Rim Conference on Lasers and Electro-Optics, CLEO - Technical Digest, 1-2 (2013).
165. G. Della Valle, S. Taccheo, R. Osellame, A. Festa, G. Cerullo, and P. Laporta, "1.5 µm single longitudinal mode waveguide laser fabricated by femtosecond laser writing," Opt. Express 15, 3190 (2007).
166. S. Taccheo, G. Della Valle, R. Osellame, G. Cerullo, N. Chiodo, P. Laporta, O. Svelto, A. Killi, U. Morgner, M. Lederer, and D. Kopf, "Er:Yb-doped waveguide laser fabricated by femtosecond laser pulses," Opt. Lett. 29, 2626-2628 (2004).
167. N. D. Psaila, R. R. Thomson, H. Bookey, N. Chiodo, S. Shen, R. Osellame, G. Cerullo, A. Jha, and A. Kar, "Er : Yb-Doped Oxyfluoride Silicate Glass Waveguide Laser Fabricated Using Ultrafast Laser Inscription," IEEE Photonic Tech. L. 20, 126-128 (2008).

168. J. Hoyo, V. Berdejo, T. Teddy Fernandez, A. Ferrer, A. Ruiz de la Cruz, J. A. Vallés, M. Rebolledo, I. Ortega-Feliu, and J. Solis, "Femtosecond laser written 16.5 mm long glass-waveguide amplifier and laser with 5.2 dB cm^{-1} internal gain at 1534 nm," Laser Phys. Lett. 10, 105802 (105807pp) (2013).
169. J. del Hoyo, P. Moreno-Zárate, G. Escalante, J. A. Vallés, P. Fernández, and J. Solís, "High-Efficiency Waveguide Optical Amplifiers and Lasers via FS-Laser Induced Local Modification of the Glass Composition," J. Lightwave Technol. 35, 2955-2959 (2017).
170. S. McDaniel, F. Thorburn, A. Lancaster, R. Stites, G. Cook, and A. Kar, "Operation of Ho:YAG ultrafast laser inscribed waveguide lasers," Appl. Opt. 56, 3251-3256 (2017).
171. D. G. Lancaster, V. J. Stevens, V. Michaud-Belleau, S. Gross, A. Fuerbach, and T. M. Monro, "Holmium-doped 2.1 µm waveguide chip laser with an output power >1 W," Opt. Express 23, 32664-32670 (2015).
172. D. Lancaster, S. Gross, H. Ebendorff-Heidepriem, M. Withford, T. Monro, and S. Jackson, "Efficient 2.9 µm fluorozirconate glass waveguide chip laser," Opt. Lett. 38, 2588-2591 (2013).
173. W. A. Clarkson, A. Dergachev, and R. Shori, "High-energy, kHz-rate, picosecond, 2-µm laser pump source for mid-IR nonlinear optical devices," Proceedings of SPIE - The International Society for Optical Engineering 8599, 85990B (2013).
174. M. Hemmer, D. Sanchez, M. Jelinek, V. Smirnov, H. Jelinkova, V. Kubecek, and J. Biegert, "2-µm wavelength, high-energy Ho:YLF chirped-pulse amplifier for mid-infrared OPCPA," Opt. Lett. 40, 451-454 (2015).

List of publications

The results discussed in this thesis are based on the following published or submitted peer-reviewed journal articles. Because of editorial policies on copyright, the publications can be downloaded from the webpage of each journal.

Paper I: **E. Kifle,** X. Mateos, P. Loiko, K. Yumashev, A. Yasukevich, V. Petrov, U. Griebner, M. Aguiló, and F. Díaz, "Graphene Q-switched Tm:KY(WO_4)$_2$ waveguide laser," Laser Physics 27, 045801 (2017).
https://doi.org/10.1088/1555-6611/aa5c15

Paper II: **E. Kifle,** X. Mateos, P. Loiko, S. Y. Choi, J. E. Bae, F. Rotermund, M. Aguiló, F. Díaz, U. Griebner, and V. Petrov, "Tm:$KY_{1-x-y}Gd_xLu_y(WO_4)_2$ planar waveguide laser passively Q-switched by single-walled carbon nanotubes," Opt. Express 26, 4961-4966 (2018).
https://doi.org/10.1364/OE.26.004961

Paper III: P. Loiko, J. M. Serres, S. S. Delekta, **E. Kifle**, J. Bogusławski, M. Kowalczyk, J. Sotor, M. Aguiló, F. Díaz, U. Griebner, V. Petrov, S. Popov, J. Li, X. Mateos, and M. Östling, "Inkjet-printing of graphene saturable absorbers for ~2 μm bulk and waveguide lasers," Opt. Mater. Express 8, 2803-2814 (2018).
https://doi.org/10.1364/OME.8.002803

Paper IV: **E. Kifle**, P. Loiko, U. Griebner, V. Petrov, P. Camy, A. Braud, M. Aguiló, F. Díaz, and X. Mateos, "Diamond saw dicing of thulium channel waveguide lasers in monoclinic crystalline films," Opt. Lett. 44, 1596-1599 (2019).
https://doi.org/10.1364/OL.44.001596

Paper V: **E. Kifle**, X. Mateos, J. R. V. de Aldana, A. Ródenas, P. Loiko, S. Y. Choi, F. Rotermund, U. Griebner, V. Petrov, M. Aguiló, and F. Díaz, "Femtosecond-laser-written Tm:$KLu(WO_4)_2$ waveguide lasers," Opt. Lett. 42, 1169-1172 (2017).
https://doi.org/10.1364/OL.42.001169

Paper VI: **E. Kifle**, P. Loiko, J. R. Vázquez de Aldana, C. Romero, A. Ródenas, V. Zakharov, A. Veniaminov, H. Yu, H. Zhang, Y. Chen, M. Aguiló, F. Díaz, U. Griebner, V. Petrov, and X. Mateos, "Fs-laser-written thulium waveguide lasers *Q*-switched by graphene and MoS_2," Opt. Express 27, 8745-8755 (2019).
https://doi.org/10.1364/OE.27.008745

Paper VII: **E. Kifle**, P. Loiko, X. Mateos, J. R. Vázquez de Aldana, A. Ródenas, U. Griebner, V. Petrov, M. Aguiló, and F. Díaz, "Femtosecond-laser-written hexagonal cladding waveguide in Tm:$KLu(WO_4)_2$: μ-Raman study and laser operation," Opt. Mater. Express 7, 4258-4268 (2017).
https://doi.org/10.1364/OME.7.004258

Paper VIII: **E. Kifle,** P. Loiko, J. R. Vázquez de Aldana, C. Romero, A. Ródenas, S. Y. Choi, J. E. Bae, F. Rotermund, V. Zakharov, A. Veniaminov, M. Aguiló, F. Díaz, U. Griebner, V. Petrov, and X. Mateos, "Passively *Q*-switched femtosecond-laser-written thulium waveguide laser based on evanescent field interaction with carbon nanotubes," Photon. Res. 6, 971-980 (2018).
https://doi.org/10.1364/PRJ.6.000971

Paper IX: **Esrom Kifle**, Pavel Loiko, Carolina Romero, Javier Rodríguez Vázquez de Aldana, Viktor Zakharov, Andrey Veniaminov, Uwe Griebner, Valentin Petrov, Patrice Camy, Alain Braud, Magdalena Aguiló, Francesc Díaz, and Xavier Mateos, " Ultrafast laser inscription and laser operation of surface Y-branch splitters in monoclinic thulium-doped crystals,". (to be submitted to ACS Photonics).

Paper X: **E. Kifle,** Pavel Loiko, Carolina Romero, Javier Rodríguez Vázquez de Aldana, Viktor Zakharov, Andrey Veniaminov, Uwe Griebner, Valentin Petrov, Patrice Camy, Alain Braud, Magdalena Aguiló, Francesc Díaz, and Xavier Mateos, " Power-scaling and in-band pumping of a fs-laser-written thulium waveguide laser with watt-level output power,". (to be submitted to Optics Express).

Paper XI: **E. Kifle**, P. Loiko, C. Romero, J. R. Vázquez de Aldana, A. Ródenas, V. Jambunathan, V. Zakharov, A. Veniaminov, A. Lucianetti, T. Mocek, M. Aguiló, F. Díaz, U. Griebner, V. Petrov, and X. Mateos, "Fs-laser-written erbium-doped double tungstate waveguide laser," Opt. Express 26, 30826-30836 (2018).
https://doi.org/10.1364/OE.26.030826

Paper XII: **E. Kifle**, P. Loiko, C. Romero, J. Rodríguez Vázquez de Aldana, A. Ródenas, V. Zakharov, A. Veniaminov, M. Aguiló, F. Díaz, U. Griebner, V. Petrov, and X. Mateos, "Femtosecond-laser-written Ho:$KGd(WO_4)_2$ waveguide laser at 2.1 μm," Opt. Lett. 44, 1738-1741 (2019).
https://doi.org/10.1364/OL.44.001738

The following articles are results published during the Ph.D. work of the candidate but are not directly related to this thesis work.

Paper XIII: W. Jing, P. Loiko, J. M. Serres, Y. Wang, **E. Kifle**, E. Vilejshikova, M. Aguiló, F. Díaz, U. Griebner, H. Huang, V. Petrov, and X. Mateos, "Synthesis, spectroscopic characterization and laser operation of Ho^{3+} in “mixed” $(Lu,Sc)_2O_3$ ceramics," Journal of Luminescence 203, 145-151 (2018).
https://doi.org/10.1016/j.jlumin.2018.06.043

Paper XIV: P. Loiko, **E. Kifle**, J. M. Serres, X. Mateos, M. Aguiló, F. Díaz, E. Vilejshikova, N. Kuleshov, and A. Pavlyuk, "Efficient continuous-wave in-band pumped Nd:$KY(MoO_4)_2$ laser," Laser Physics Letters 15, 065002 (2018).
https://doi.org/10.1088/1612-202X/aab82f

Paper XV: P. Loiko, J. Bogusławski, J. M. Serres, **E. Kifle**, M. Kowalczyk, X. Mateos, J. Sotor, R. Zybała, K. Mars, A. Mikuła, K. Kaszyca, M. Aguiló, F. Díaz, U. Griebner, and V. Petrov, "Sb_2Te_3 thin film for the passive Q-switching of a Tm:$GdVO_4$ laser," Opt. Mater. Express 8, 1723-1732 (2018).
https://doi.org/10.1364/OME.8.001723

Paper XVI: Z. Pan, J. M. Serres, **E. Kifle**, P. Loiko, H. Yuan, X. Dai, H. Cai, M. Aguiló, F. Díaz, Y. Wang, Y. Zhao, U. Griebner, V. Petrov, and X. Mateos, "Comparative study of the spectroscopic and laser properties of Tm^{3+}, $Na^+(Li^+)$-codoped $Ca_3Nb_{1.5}Ga_{3.5}O_{12}$-type disordered garnet crystals for mode-locked lasers," Opt. Mater. Express 8, 2287-2299 (2018).
https://doi.org/10.1364/OME.8.002287

Paper XVII: J. W. Kim, S. Y. Choi, J. E. Bae, M. H. Kim, Y. U. Jeong, **E. Kifle**, X. Mateos, M. Aguiló, F. Díaz, U. Griebner, V. Petrov, G.-H. Kim, and F. Rotermund, "Comparative study of Yb:KYW planar waveguide lasers Q-switched by direct- and evanescent-field interaction with carbon nanotubes," Opt. Express 27, 1488-1496 (2019).
https://doi.org/10.1364/OE.27.001488

Paper XVIII: Z. Pan, P. Loiko, J. M. Serres, **E. Kifle**, H. Yuan, X. Dai, H. Cai, Y. Wang, Y. Zhao, M. Aguiló, F. Díaz, U. Griebner, V. Petrov, and X. Mateos, " "Mixed" Tm:$Ca(Gd,Lu)AlO_4$ - a novel crystal for tunable and mode-locked 2 μm lasers," Opt. Express 27, 9987-9995 (2019).
https://doi.org/10.1364/OE.27.009987

Paper XIX: P. Loiko, R. Soulard, **E. Kifle**, L. Guillemot, G. Brasse, A. Benayad, J.-L. Doualan, A. Braud, M. Aguiló, F. Díaz, X. Mateos, and P. Camy, "Ytterbium calcium fluoride waveguide laser," Opt. Express 27, 12647-12658 (2019).
https://doi.org/10.1364/OE.27.012647

Paper XX: L. Zhang, P. Loiko, J. M. Serres, **E. Kifle**, H. Lin, G. Zhang, E. Vilejshikova, E. Dunina, A. Kornienko, L. Fomicheva, U. Griebner, V. Petrov, Z. Lin, W. Chen, K. Subbotin, M. Aguiló, F. Díaz, and X. Mateos, "Growth, spectroscopy and first laser operation of monoclinic Ho^{3+}:$MgWO_4$ crystal," Journal of Luminescence 213, 316-325 (2019).
https://doi.org/10.1016/j.jlumin.2019.04.035

The results discussed in this thesis are also based on the following conference publications:

C-paper I: P. Loiko, J. M. Serres, S. S. Delekta, **E. Kifle**, X. Mateos, A. Baranov, M. Aguiló, F. Díaz, U. Griebner, V. Petrov, S. Popov, J. Li, and M. Östling, "Inkjet-Printing of Graphene Saturable Absorbers for ~2 μm Bulk and Waveguide Lasers," in Conference on Lasers and Electro-Optics, OSA Technical Digest (online) (Optical Society of America, 2017), STh1I.4.

C-paper II: **E. Kifle**, X. Mateos, J. R. Vázquez de Aldana, A. Ródenas, P. Loiko, S. Y. Choi, F. Rotermund, U. Griebner, V. Petrov, M. Aguiló, and F. Díaz, "Femtosecond Laser-Written Tm:$KLu(WO_4)_2$ Waveguide Lasers," in 2017 European Conference on Lasers and Electro-Optics and European Quantum Electronics Conference, (Optical Society of America, 2017), CJ_P_31.

C-paper III: **E. Kifle**, X. Mateos, P. Loiko, S. Y. Choi, F. Rotermund, M. Aguiló, F. Díaz, V. Petrov, and U. Griebner, "Tm:$KY(WO_4)_2$ Planar Waveguide Laser Q-switched by Single-Walled Carbon Nanotubes," in Laser Congress 2017 (ASSL, LAC), OSA Technical Digest (online) (Optical Society of America, 2017), JTh2A.28.

C-paper IV: Z. Pan, J. M. Serres, **E. Kifle**, P. Loiko, H. Yuan, X. Dai, H. Cai, Y. Wang, Y. Zhao, M. Aguiló, F. Díaz, X. Mateos, U. Griebner, and V. Petrov, "Growth, spectroscopy and laser operation of "mixed" Tm:$Ca(Gd,Lu)AlO_4$ – A novel crystal for mode-locked lasers," in Laser Congress 2018 (ASSL), OSA Technical Digest (Optical Society of America, 2018), ATu2A.21.

C-paper V: P. Loiko, J. Bogusławski, J. M. Serres, **E. Kifle**, M. Kowalczyk, X. Mateos, J. Sotor, R. Zybała, K. Mars, A. Mikuła, M. Aguiló, F. Díaz, U. Griebner, and V. Petrov, "Tm:$GdVO_4$ microchip laser Q-switched by a Sb_2Te_3 topological insulator," SPIE LASE (SPIE, 2018), Vol. 10511.

C-paper VI: **E. Kifle**, X. Mateos, J. R. V. d. Aldana, A. Ródenas, P. Loiko, V. Zakharov, A. Veniaminov, H. Yu, H. Zhang, Y. Chen, M. Aguiló, F. Díaz, U. Griebner, and V. Petrov, "Passive Q-switching of femtosecond-laser-written Tm:$KLu(WO_4)_2$ waveguide lasers by graphene and MoS_2 saturable absorbers, SPIE LASE (SPIE, 2018), Vol. 10511.

C-paper VII: **E. Kifle**, P. Loiko, J. R. V. de Aldana, A. Ródenas, L. Zhang, Z. Lin, H. Lin, G. Zhang, V. Petrov, U. Griebner, M. Aguiló, F. Díaz, X. Mateos, and W. Chen, "Highly-Efficient Femtosecond-Laser-Written Waveguide Lasers at ~2 μm in Monoclinic Tm:$MgWO_4$," in Conference on Lasers and Electro-Optics, OSA Technical Digest (online) (Optical Society of America, 2018), SM2N.6.

C-paper VIII: **E. Kifle,** P. Loiko, C. Romero, J. R. V. de Aldana, M. Aguiló, F. Díaz, A. Braud, P. Camy, U. Griebner, V. Petrov, and X. Mateos, "Watt-Level fs-Laser-Written Thulium Waveguide Lasers," in Conference on Lasers and Electro-Optics, OSA Technical Digest (Optical Society of America, 2019), STh1E.5.

UNIVERSITAT
ROVIRA i VIRGILI